



Algorithm Theoretical Basis Document
for the
Cross Track Infrared Sounder
(CrIS)
Environmental Data Records
(EDR)

Version 1.2.3 – March 2001

With contributions from:

Jean-Luc Moncet, Xu Liu, Hélène Rieu-Isaacs, Ned Snell, Scott Zaccheo, Richard Lynch, Janusz Eluszkiewicz, Yuguang He, Gennadi Uymin, Chris Lietzke, Jennifer Hegarty, Sid Boukabara, Alan Lipton, John Pickle

AER, Inc. Document Number P882-TR-E-1.2.3-ATBD-03-01
ITT A/CD Document 818004

HISTORY OF REVISIONS

Version 1.0: Delivered at PDR - May 1999.

Version 1.1: Delivered at SSSR - March 2000.

- Addition of AER, Inc. document numbering on front page.
- Addition of bookmarks and thumbnails in pdf version.
- Modification of Equation (11) for transmittance equation in section 5.5.
- Correction of nominal accuracy for OSS selection in paragraph 5.3.
- Correction of Equation (51) for transformed retrieval equation in paragraph 6.3.

Version 1.2: Delivered in October 2000.

- Section 9.6 on the surface pressure determination has been revised.
- Changes were made in Section 6.1.2. They include new information about point selections, validation and methods used (Monte Carlo vs sequential search method). Figures which illustrate selection of OSS points and a validation procedure have been added.
- Section 0 has been expanded to discuss approaches to the computation of the Planck function and to include a subsection on trace gas variability.

Version 1.2.2: Delivered in December 2000.

- The main body of the document has been rearranged to follow the structural design of the algorithm.
- Some appendices that are not referenced in the text have been removed.

Version 1.2.3: Delivered in March 2001.

- Post-DDR version (updated figures).

TABLE OF CONTENTS

HISTORY OF REVISIONS.....	2
TABLE OF CONTENTS.....	3
LIST OF TABLES	7
LIST OF FIGURES	8
1 INTRODUCTION.....	12
2 EDR REQUIREMENTS	13
2.1 Definitions and Requirements.....	13
2.2 Atmospheric Moisture Profile.....	14
2.3 Atmospheric Vertical Temperature Profile.....	15
2.4 Pressure (Surface/Vertical Profile).....	17
2.5 Timing.....	18
3 CrIMSS INSTRUMENTS OVERVIEW	19
3.1 Infrared Instrument: CrIS.....	19
3.2 Microwave Instruments: AMSU and MHS.....	23
3.2.1 AMSU	23
3.2.2 MHS	23
4 CrIMSS ALGORITHM OVERVIEW.....	26
5 FORWARD MODEL	28
5.1 RT Equation in the Microwave.....	28
5.2 RT Equation in the Infrared	29
5.3 Overview of the OSS Method.....	30
5.4 Implementation of the OSS Method.....	33
5.4.1 Infrared	33
5.4.2 Microwave.....	42
5.5 Radiance Calculations in the OSS forward model.....	43
5.5.1 Optical Depth Tables.....	43
5.5.2 Radiance and derivative calculation.....	45
5.6 Practical Implementation.....	49
5.7 Treatment of Clouds.....	51
5.7.1 Microwave.....	51

TABLE OF CONTENTS

5.7.2	Infrared	52
6	INVERSE MODEL.....	53
6.1	Linearization Noise	54
6.2	Non-Linear Physical Inversion Method for CrIMSS	55
6.3	Eigenvector Transformation of Retrieved Parameters	56
7	RETRIEVAL STRATEGIES UNDER CLOUDY CONDITIONS.....	59
7.1	Cloud Clearing (CC)	59
7.2	Simultaneous Cloud Parameter Retrieval (SCPR).....	59
7.3	Hole Hunting (HH).....	60
8	INITIALIZATION.....	61
9	INPUT AND PRE-PROCESSING	62
9.1	Microwave SDR.....	62
9.2	Infrared SDR	62
9.3	External Data Inputs.....	62
9.3.1	Required Data in Case of Failure of the Microwave Instruments	63
9.3.2	Optional Data for Performance Enhancement.....	63
9.4	Precipitation Check	63
9.5	Surface Type Determination	64
9.6	Surface Pressure Computation	65
9.6.1	Hydrostatic Equation.....	66
9.6.2	Possible Improvement	68
9.6.3	Example.....	69
9.6.4	Alternative Method.....	70
9.7	NWP Initial Guess Profiles	71
10	MICROWAVE-ONLY RETRIEVAL	72
10.1	Description of the Algorithm	72
10.2	Retrieved Parameters.....	73
11	SCENE CLASSIFICATION.....	76
12	JOINT MICROWAVE AND INFRARED RETRIEVAL	82
12.1	General Description of the Algorithm.....	82
12.2	Channel Selection and Apodization	84
12.3	Impact of Trace Gas Variability.....	85

TABLE OF CONTENTS

12.3.1	Ozone	85
12.3.2	N ₂ O.....	86
12.4	Possible Strategy for IR Cloud Parameter Retrieval	89
12.5	Retrieved Parameters.....	90
13	QUALITY CONTROL.....	92
13.1	Normalized χ^2 Test.....	92
13.2	Deviation Between MW-Only and Joint MW+IR Retrievals	92
13.3	MW Quality Control Test	93
13.4	Quality Control Procedure Flow Diagram	93
13.5	Application of QC to Scanline Retrievals	94
13.6	Estimating Accuracy of Cloud-Cleared Radiances.....	98
14	OUTPUT AND POST-PROCESSING.....	99
14.1	Required Outputs.....	99
14.2	Optional Outputs	99
14.3	Post-processing.....	100
14.3.1	Pressure Profile Computation	100
14.3.2	Temperature and Water Vapor Profile Interpolation	101
14.3.3	Slant-to-Vertical Conversion	102
14.3.4	Lower and Upper Air Temperature Profiling	102
15	TIMING.....	103
APPENDIX 1: SUPPLEMENTARY INFORMATION ABOUT THE OSS METHOD....		104
1	Monte Carlo Approach to the OSS Model.....	104
1.1	Introduction	104
1.2	Determinant Control.....	106
1.3	Statistical Control.....	107
2	Validation of the OSS Model.....	108
3	Transformation Between Apodized and Unapodized Spectra.....	113
APPENDIX 2: CHANNEL SELECTION		114
1	Introduction.....	114
2	Description of the Method.....	114
3	Implementation and Retrieval Results.....	116
APPENDIX 3: EMPIRICAL ORTHOGONAL FUNCTIONS		121

TABLE OF CONTENTS

1	Introduction.....	121
2	Principal Component Analysis of the NOAA-88 profiles.....	121
3	Transformation of Retrieval Variables.....	122
	APPENDIX 4: SIGNAL APODIZATION.....	128
1	Introduction.....	128
2	Unapodized Channel Response Function	128
3	Hamming's Filter Function	131
	APPENDIX 5: INVERSION METHODS.....	134
1	Introduction.....	134
2	Retrieval Methods.....	134
3	Simulation Results.....	135
4	Summary.....	137
	APPENDIX 6: THE CLOUD CLEARING (CC) METHOD.....	142
1	Treatment of Radiances in Cloudy Atmospheres	142
2	Single Cloud Formation with 2 FOVs.....	144
3	Channel Selection for Cloud Filtering	146
4	Determination of η for a Single Cloud Formation.....	147
5	Multiple Cloud Formations with Multiple FOVs.....	150
	REFERENCES.....	152
	LIST OF ACRONYMS.....	156

LIST OF TABLES

Table 1: Atmospheric Vertical Moisture Profile EDR Requirements.....	14
Table 2: ITT Guaranteed Performance – Moisture Uncertainty (RMS,%).	15
Table 3: Atmospheric Vertical Temperature Profile EDR Requirements.....	15
Table 4: ITT Guaranteed Performance – Temperature Uncertainty (RMS, K).	16
Table 5: Pressure (Surface/Profile) EDR Requirements.	17
Table 6: ITT Guaranteed Performance--Pressure Accuracy and Precision.	17
Table 7: Spectral Band Characteristics as Defined by the CrIS SDR.....	19
Table 8: AMSU (1 to 15) and MHS (16 to 20) Channel Set.....	24
Table 9: Number of OSS points in LWIR.....	37
Table 10: Number of OSS points in MWIR.....	37
Table 11: Number of OSS points in SWIR.	37
Table 12: Number of Spectral Points Selected in the MW.	42
Table 13: List of Parameters Retrieved in the Microwave.....	74
Table 14: Parameters Retrieved in the Joint MW+IR Retrieval.	90
Table 15: Timing (in seconds) for the RT Model and the Joint MW+IR Retrieval.....	103
Table 16: Selected Channels for CrIS.....	117

LIST OF FIGURES

Figure 1: An example of simulated clear sky brightness temperatures.....	20
Figure 2: Temperature weighting function (in arbitrary units)	21
Figure 3: Temperature weighting function (in arbitrary units)	21
Figure 4: Temperature weighting function (in arbitrary units)	22
Figure 5: AMSU/MHS FOV Configuration.	24
Figure 6: Channels Position for AMSU (1 to 15) and MHS (16 to 20).	25
Figure 7: CrIMSS EDR Algorithm Flow Diagram.	26
Figure 8: Number of spectral points per channel selected for <i>Sinc</i> ILS:.....	35
Figure 9: Number of spectral points selected in SWIR with variable surface emissivity for (a) <i>Blackman</i> ILS, (b) <i>Hamming</i> ILS, (c) <i>Sinc</i> ILS.	36
Figure 10: RMS differences between OSS-generated and true radiances for <i>Sinc</i> ILS....	38
Figure 11: RMS differences between OSS-generated and true radiances in SWIR with .	39
Figure 12: LWIR, <i>Hamming</i> - 40π ILS, variable emissivity.	40
Figure 13: LWIR, variable emissivity. Transformation between <i>Sinc</i> with unlimited number of side-lobes and (a) <i>Blackman</i> - 3π , (b) <i>Hamming</i> - 40π	41
Figure 14: Comparison OSS/Central Frequency (Maximum Differences).....	43
Figure 15: Numbering convention for the atmospheric layers used by OSS.	46
Figure 16: Inversion flowchart.	58
Figure 17: Surface Type Identification.	65
Figure 18: Flowchart for surface pressure calculation. Temperature and water vapor profiles are also available on output.	68
Figure 19: Illustration of configuration. Input from NWP: surface pressure, surface elevation, and temperature and water vapor profiles.	69
Figure 20: Surface pressure for the Tibetan Plateau/India region at 0.1° resolution (a) Calculated using the method described in this section (b) Obtained from a direct interpolation of NWP data.	70
Figure 21: Functional Flow Diagram for MW Retrieval.	73
Figure 22: Flow Diagram of the Scene Classification Module.	76
Figure 23: The first 6 EOFs resulting from PCA.	78

LIST OF FIGURES

Figure 24: The Magnitudes of Singular Values (equal to the square root of eigenvalues λ).	79
Figure 25: Clustering Pattern for 1 cloud formation.	79
Figure 26: Application of PCA to estimate the number of cloud formations. (a) Number of estimated cloud formations. (b) Cloud top pressure of the clouds. (c) Cloud fraction of cloud 1 (d) Cloud fraction of cloud 2.	81
Figure 27: Flow Chart for the Joint Microwave and Infrared Retrieval.	83
Figure 28: Impact of O ₃ variability on temperature and moisture retrievals. Green lines: baseline algorithm (no O ₃ variability), red lines: retrieval performed on simulated radiances including ozone profiles from the NOAA-88 database. In the retrieval, an O ₃ column factor has been retrieved.	86
Figure 29: Simulated N ₂ O profiles from the SKYHI model (red lines). The black line represents the standard N ₂ O profile.	87
Figure 30: Radiative effect of variable N ₂ O. The red lines show the differences in brightness temperatures between radiances simulated using SKYHI N ₂ O profiles and the standard profile. Black lines represent instrument noise. Only results for the MWIR and SWIR bands are shown, as the impact of variable N ₂ O is minimal in LWIR.	87
Figure 31: Impact of variable N ₂ O on the CrIS retrieval RMS error. Red: baseline algorithm (no N ₂ O variability), green: variable N ₂ O affecting radiances, ignored in the retrieval, blue: N ₂ O affecting radiances, retrieved as a column scaling factor, black: similar to blue, but N ₂ O enhanced by 50% between 1000 and 900 mbar.	88
Figure 32: Similar to Figure 31, but for CrIS bias error.	88
Figure 33: Quality Control Flow Diagram.	93
Figure 34: Location of scanlines.	94
Figure 35: (a) Average cloud top pressure, (b) average cloud fraction, and (c) maximum cloud contrast for each FOR. The bars in (b) divide the 16 scanlines.	95
Figure 36: a) The absolute value of the difference in the average lower tropospheric temperature for each FOR. b) Same as (a) but with the rejection criterion applied.	96
Figure 37: (a) Error in the lower tropospheric temperature for each FOR (sequenced from small to large), (b) χ^2 plotted in the same sequence as (a). (c) χ^2_{MW} plotted in the same sequence as (a), (d) σ plotted in the same sequence as (a).	97

LIST OF FIGURES

Figure 38: RMS error for temperature and moisture. Results with and without QC are presented. With QC implemented, 129 profiles out of 480 were rejected (27%).	97
Figure 39: Pressure Profile Uncertainty.	101
Figure 40: Flow diagram for the MC approach to the OSS model.	105
Figure 41: Number of spectral points selected for <i>Blackman</i> ILS with 3 side lobes. (a) LWIR,	109
Figure 42: Similar to Figure 41, but for <i>Hamming</i> ILS with 40 side lobes.	110
Figure 43: RMS differences between OSS-generated & true radiances for <i>Blackman</i> ILS with 3 side lobes. (a) LWIR, (b) MWIR, (c) SWIR.	111
Figure 44: Similar to Figure 43, but for <i>Hamming</i> ILS with 40 side lobes.	112
Figure 45: Water vapor derivatives and selection thresholds. Channels for which the absolute values of water vapor derivatives exceed the threshold are excluded from the entropy-based channel selection for temperature	118
Figure 46: Trace gas derivatives and selection thresholds for the CrIS Bands 1-3. Channels for which the absolute values of trace gas derivatives exceed the threshold are excluded from the entropy-based channel selection for temperature, water vapor, and surface parameters.	118
Figure 47: Typical Temperature Entropy (δS) per Channel.	119
Figure 48: Selected channels for temperature T (with and without band 2), water vapor, and the surface parameters as a function of the total number of channels. The temperature channels selected in Band 2 are based on information in all three bands (non-weighted S_e).	119
Figure 49: RMS errors for temperature and water vapor for 200 clear-sky ocean scenes. Results from second stage retrievals performed using all IR channels and subsets of 150, 300, and 400 channels are shown.	120
Figure 50: First 6 EOFs as a result of a PCA of NOAA-88 temperature profiles.	123
Figure 51: BIAS and RMS representation errors of NOAA-88 temperature profiles using 20 EOFs.	124
Figure 52: Layer-mean representation errors of NOAA-88 temperature profiles.	124
Figure 53: The original NOAA-88 temperature profile (solid line) and the profile reconstructed using 20 EOFs (stars). The plot on the right is the difference.	125
Figure 54: First 6 EOFs as a result of applying PCA to NOAA-88 moisture profiles. SV stands for the square root of eigenvalues.	125

LIST OF FIGURES

Figure 55: BIAS and RMS errors of the reconstructed NOAA-88 moisture profiles using 15 eigenvectors.....	126
Figure 56: BIAS and RMS errors of the reconstructed NOAA-88 moisture profiles using 10 eigenvectors.....	126
Figure 57: Example of the original and reconstructed moisture profiles and its difference.	127
Figure 58: BIAS and RMS error when applying the eigenvectors obtained from the analysis of the NOAA-88 moisture profiles to reconstruct the TIGR moisture profiles.....	127
Figure 59: Boxcar Apodization Function and its Sinc Fourier Transform.	129
Figure 60: Hamming Apodization Function and its Fourier Transform.	132
Figure 61: Algorithm retrieval rates and χ^2 values versus iteration number for clear-sky land and ocean cases (microwave first guess). Results obtained using the DRAD, Levenberg-Marquardt, and Maximum Likelihood methods are shown. The upper plots describe the number of retrievals that meet the radiance convergence criterion ($\chi^2 < 2$). The lower plots show average χ^2 values for profiles that converged in 8 iterations.....	137
Figure 62: Percent retrieved and normalized χ^2 for cloudy cases corresponding to Figure 61.	138
Figure 63: Temperature and water vapor RMS errors for 200 clear-sky land profiles retrieved using the DRAD algorithm.	138
Figure 64: Similar to Figure 63, but for the Levenberg-Marquardt algorithm.....	139
Figure 65: Similar to Figure 63, but for the Maximum Likelihood algorithm.....	139
Figure 66: Similar to Figure 61, but for climatology first guess.....	140
Figure 67: Temperature and water vapor RMS errors for 200 clear-sky land profiles retrieved using the DRAD algorithm and a climatology first guess.	140
Figure 68: Similar to Figure 67, but for the Levenberg-Marquardt algorithm.	141
Figure 69: Similar to Figure 67, but for the Maximum Likelihood algorithm.....	141

1 INTRODUCTION

This algorithm theoretical basis document (ATBD) describes the theoretical background and functional implementation of the environmental data record (EDR) retrieval algorithm for the Cross Track Infrared and Microwave Sounder Suite (CrIMSS). The algorithm has been developed by Atmospheric and Environmental Research, Inc. (AER) in support of the National Polar-orbiting Operational Environmental Satellite System (NPOESS). The mission of the CrIMSS payload is to produce both Sensor Data Record (SDR) and EDR in support of the NPOESS mission requirements. The SDR processing is described in the companion SDR ATBD (Lachance *et al.* 1999). The EDR allocated to CrIMSS include vertical moisture profile, vertical temperature profile, and surface/pressure profile. The CrIMSS payload consists of infrared and microwave components. The infrared component is the Cross Track Infrared Sounder (CrIS) to be procured by NPOESS with nominal characteristics defined by ITT CrIS system specification. The microwave components are assumed to include the Advanced Microwave Sounding Unit (AMSU) and the Microwave Humidity Sounder (MHS) supplied by NASA. Differing in their sensitivity to clouds, the microwave components provide data in situations of full overcast as well as first guess information for the infrared component. In partly cloudy and clear situations, the infrared component provides the highest quality EDR.

The organization of this document is as follows. The EDR thresholds and objectives allocated to CrIMSS are presented in Section 2, followed by an overview of the sensor suite in Section 3. A top level flow diagram for the CrIMSS algorithm is presented in Section 4. Sections 5 and 6 describe our general approach to the forward and inverse problems, respectively, with Section 7 providing an overview of retrieval strategies under cloudy conditions. The initialization of the retrieval process is described in Section 8, followed by a description of input and pre-processing in Section 9. Section 10 describes the microwave-only retrieval, followed by a description of the scene classification in Section 11 and of the joint microwave and infrared retrieval in Section 12. Quality control and post-processing are discussed in Sections 13 and 14, respectively. The timing results for the current version of the algorithm are presented in Section 15. This document also contains a set of supporting appendices providing detailed information about various components of the algorithm and describing results from trade studies.

2 EDR REQUIREMENTS

2.1 Definitions and Requirements

EDR requirements are divided into two categories: primary and secondary. Primary EDRs are those EDR attributes for which the CrIMSS contractor has been assigned primary algorithm development responsibility. The algorithm may or may not require the use of additional data from other than the primary sensor. Secondary EDRs are those attributes for which the sensor may provide data as a secondary input to an EDR algorithm assigned as a primary EDR to another NPOESS sensor contractor.

Unless otherwise specified, attribute values are to be interpreted as upper bounds anywhere in the area where measurements are obtained, including the edge of the measuring sensor field of regard. Unless otherwise specified, a percentage appearing as a value for an attribute is to be interpreted as the percentage of the true value of the attribute. For any attribute where a percentage and a numerical value are specified, the greater of the two is the requirement.

Specification of horizontal cell size or horizontal spatial resolution at nadir does not imply that data must be acquired from a cross-track scanning sensor. The data may be acquired from a conical scanning sensor or any other sensor as long as the horizontal cell size or resolution along the satellite ground track does not exceed the nadir upper bound. For an EDR for which horizontal cell size is specified only at nadir, cell size is allowed to grow away from nadir as a normal function of the looking angle.

“Clear” refers to cases in which the average fractional cloudiness in the array of CrIS spots falling within a 48 km square “AMSU like” footprint is up to 50%. The instrument shall be capable of meeting “clear” sounding requirements in situations where none of the individual spots are totally cloud-free. “Cloudy” refers to cases in which the average fractional cloudiness is in the range from 50% to 100% (e.g., totally overcast). The “average fractional cloudiness” is determined from the sensor’s view angle, not from a local vertical. “Cloud-Free” represents conditions in which no clouds are present.

The following tables present the EDR requirements and ITT's guaranteed performances for the primary EDR (atmospheric vertical moisture profile, atmospheric vertical temperature profile, vertical pressure profile and timing).

2.2 Atmospheric Moisture Profile

An atmospheric vertical moisture profile is a set of estimates of average mixing ratio in three-dimensional cells centered on specified points along a local vertical. For this EDR, horizontal cell size is specified at nadir only. The mixing ratio of a sample of air is the ratio of the mass of water vapor in the sample to the mass of dry air in the sample. Units for mixing ratio are gram per kilogram (g/kg).

Table 1: Atmospheric Vertical Moisture Profile EDR Requirements.

Parameter	Guaranteed Performance
a. Horizontal Cell Size	12.4 km @ nadir
b. Horizontal Reporting Interval	1 to 9 per FOR
c. Vertical Cell Size	2 km
d. Vertical Reporting Interval	
1. surface to 850 mb	20 mb
2. 850 mb to 100 mb	50 mb
e. Horizontal Coverage (Global)	N/A*
f. Vertical Coverage	Surface to 100 mb
g. Measurement Range	0 - 30 gm/km
h. Measurement Uncertainty (expressed as a percent of average mixing ratio in 2 km layers)	See Table 2
i. Mapping Uncertainty	1.45 km
j. Minimum Ground Swath-width (833 km, circular, polar-orbit altitude)	2200 km See *

*Horizontal Coverage is a system level specification determined by the number of satellites, orbitology, and sensor swath width. Thus, only "Minimum Ground Swath-width" is specified at the sensor level.

Table 2: ITT Guaranteed Performance – Moisture Uncertainty (RMS,%).

Altitude (mb)	Guaranteed Performance - Clear	Guaranteed Performance - Cloudy
Surface-600	14.1	15.8
600-300	13.8	17.1
300-100	11.7	16.4

2.3 Atmospheric Vertical Temperature Profile

An atmospheric temperature profile is a set of estimates of the average atmospheric temperature in three-dimensional cells centered on specified points along a local vertical. Units for temperature are Kelvins (K).

Table 3: Atmospheric Vertical Temperature Profile EDR Requirements.

Parameter	Guaranteed Performance
a. Horizontal Cell Size	
1. Clear, nadir	12.4 km to 0.1 mb 40 km above 0.1 mb
2. Clear, worst case	44 km
3. Cloudy, nadir	43 km
4. Cloudy, worst case	151 km
b. Horizontal Reporting Interval	One to nine per FOR
c. Vertical Cell Size	
Clear (< 50% cloudy)	
1. surface to 300 mb	1 km
2. 300 mb to 30 mb	3 km
3. 30 mb to 1 mb	5 km
4. 1 mb to 0.01 mb	5 km
Cloudy	
5. surface to 700 mb	1 km
6. 700 mb to 300mb	1 km

SECTION 2: EDR REQUIREMENTS

7. 300 mb to 30 mb	3 km
8. 30 mb to 1 mb	5 km
9. 1 mb to 0.01 mb	5 km
d. Vertical Reporting Interval	
1. surface to 850 mb	20 mb
2. 850 mb to 300 mb	50 mb
3. 300 mb to 100 mb	25 mb
4. 100 mb to 10 mb	20 mb
5. 10 mb to 1 mb	2 mb
6. 1 mb to 0.1 mb	0.2 mb
7. 0.1 mb to 0.01 mb	0.02 mb
e. Horizontal Coverage (global)	N/A*
f. Vertical Coverage	Surface to 0.01 mb
g. Measurement Range	
1. Earth Scene	180 - 335K
2. Black Body	180 - 310K
h. Measurement Uncertainty**	See Table 4
i. Mapping Uncertainty	1.45 km
j. Minimum Ground Swath-width (833 km, circular, polar-orbit altitude)	2200 km See *

* See footnote to Table 1.

** Measurement Uncertainty for all altitudes of 1.0 to 0.01 mbar shall be referenced to the Cloudy Horizontal Cell Size thresholds and objectives as listed under a3 and a4.

Table 4: ITT Guaranteed Performance – Temperature Uncertainty (RMS, K).

Altitude (mb)	Clear	Cloudy
Surface-700	0.9	2.27
700-300	0.9	1.24
300-30	0.98	1.27
30-1	1.45	1.45
1-0.5	3.5	3.5

2.4 Pressure (Surface/Vertical Profile)

A pressure profile is a set of estimates of atmospheric pressure at specified altitudes above the Earth's surface. Pressure is a derived quantity. Its profile is derived from the retrieved temperature and moisture profiles and an external estimate of pressure at some level in the atmosphere. Units for pressure are millibars (mb).

Table 5: Pressure (Surface/Profile) EDR Requirements.

Parameter	Guaranteed Performance
a. Horizontal Cell Size, nadir	43 km
b. Horizontal Reporting Interval	One to nine per FOR
c. Vertical Cell Size	1 km
d. Vertical Reporting Interval	
1. 0 - 2 km	1 km
2. 2 - 5 km	1 km
3. > 5 km	1 km
e. Horizontal Coverage (global)	N/A
f. Vertical Coverage	0 - 30 km
g. Measurement Range	10 - 1050 mb
h. Measurement Accuracy	See Table 6
i. Measurement Precision	4 mb
j. Mapping Uncertainty	1.45 km
m. Minimum Ground Swath-width(833 km, circular, polar-orbit altitude)*	2200 km

* See footnote to Table 1.

Table 6: ITT Guaranteed Performance--Pressure Accuracy and Precision.

Altitude (km)	Accuracy (%)	Precision (mb)
0-2	0.51	3.13
2-10	0.74	2.45
10-30	0.87	0.91

2.5 Timing

Any initialization of operational EDR algorithms which is unique to specific satellite, sensor data or orbital conditions shall take no more than 1 minute following receipt of the first segments of CrIS SDRs. The SDRs transmitted to EDR algorithms shall be broken into segments and processed in blocks. Processing of one SDR data block in operational algorithms into an EDR data block shall be completed and handed off as a user output prior to processing of the next data block. Processing time associated with each data block shall be 1 minute or less. SDR data resulting from 1.25 orbits of data collection shall be fully processed into EDRs in under 18 minutes when scientific code is converted to operational code running on forecast 2007 desktop computers.

3 CrIMSS INSTRUMENTS OVERVIEW

3.1 Infrared Instrument: CrIS

The CrIS (Cross Track Infrared Sounder) instrument is a Michelson interferometer infrared sounder covering the spectral range of approximately 3.9 to 15.4 microns. CrIS provides cross-track measurements of scene radiances to permit the calculation of vertical distribution of temperature and moisture in the Earth's atmosphere. The nominal spectral resolution is defined as $1/2L$, where L is the maximum optical path difference of the interferometer. A critical consideration in the design of an interferometer is the choice of apodization function. Some information on this subject is provided in Appendix 4.

The frequency range adopted in the current design of the CrIS instrument is listed in Table 7. There are three bands in the CrIS spectral range, denoted as LWIR, MWIR, and SWIR. Figure 1 shows an example of simulated clear sky radiances in the spectral range covering the three CrIS bands. The radiances are expressed in brightness temperature units. The emission in the spectral region from 635 to about 800 cm^{-1} is mainly from atmospheric CO_2 and is used for atmospheric temperature sounding. The atmospheric window region in LWIR extends from 800 to about 950 cm^{-1} and provides sounding channels for the surface properties and the lower troposphere temperatures. The main emission band of O_3 is centered around 1050 cm^{-1} . The main emission in MWIR is due to atmospheric moisture, although there are some contributions from methane and nitrous oxide near 1250 cm^{-1} . MWIR contains most of CrIS atmospheric moisture sounding channels. The main feature in SWIR is the emission from the $4.18\text{-}\mu\text{m}$ CO_2 band, which can also be used for atmospheric temperature sounding.

Table 7: Spectral Band Characteristics as Defined by the CrIS SDR.

Band	Frequency Range	Resolution ($1/2L$)	# Channels
LWIR	$650\text{-}1095\text{ cm}^{-1}$	0.625 cm^{-1}	713
MWIR	$1210\text{-}1750\text{ cm}^{-1}$	1.25 cm^{-1}	433
SWIR	$2155\text{-}2550\text{ cm}^{-1}$	2.5 cm^{-1}	153
Total			1305

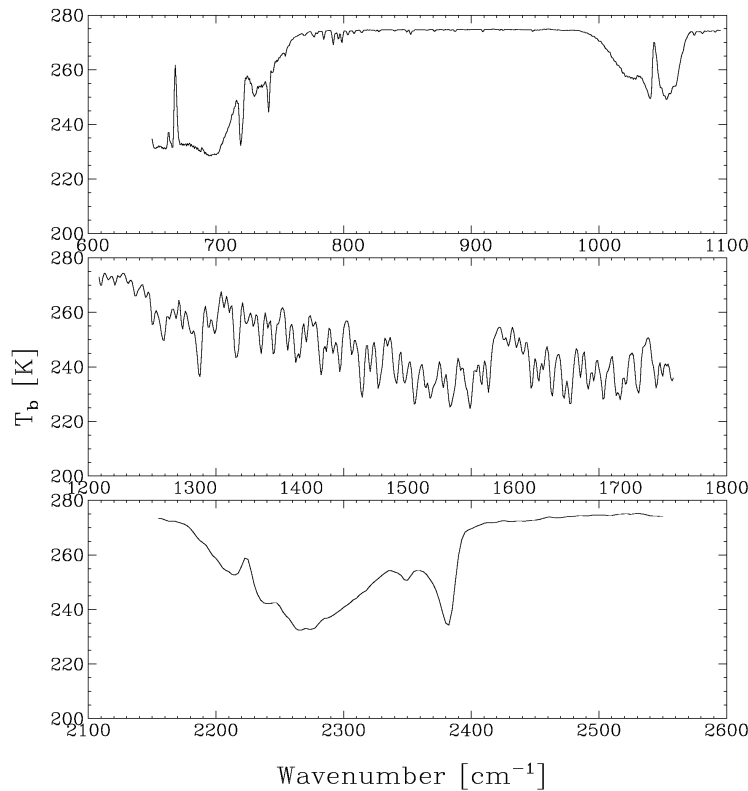


Figure 1: An example of simulated clear sky brightness temperatures in the three CrIS spectral bands.

Figures 2-4 show the temperature derivatives (weighting functions) normalized by the CrIS instrument noise in the 3 CrIS bands. It is clear that the centers of CO₂ bands are responsible for the sounding of upper atmospheric temperature. For channels away from the center of CO₂ band the peak of the weighting function shifts down in altitude, allowing for sounding of the atmosphere below 1 mb. The width of the weighting function is a good indicator of the vertical resolution of the sounding instrument. For the CrIS instrument there is better vertical resolution at the lower altitudes relative to that at higher altitudes. It should be mentioned that MWIR is very sensitive to lower atmospheric temperatures. However, channels in MWIR are also sensitive to atmospheric moisture and they should not be used as the primary temperature sounding channels if temperature and moisture are retrieved sequentially. In the current version of the code, all geophysical parameters are retrieved simultaneously and therefore MWIR also contributes to the lower atmospheric temperature retrievals.

SECTION 3: CrIMSS INSTRUMENTS OVERVIEW

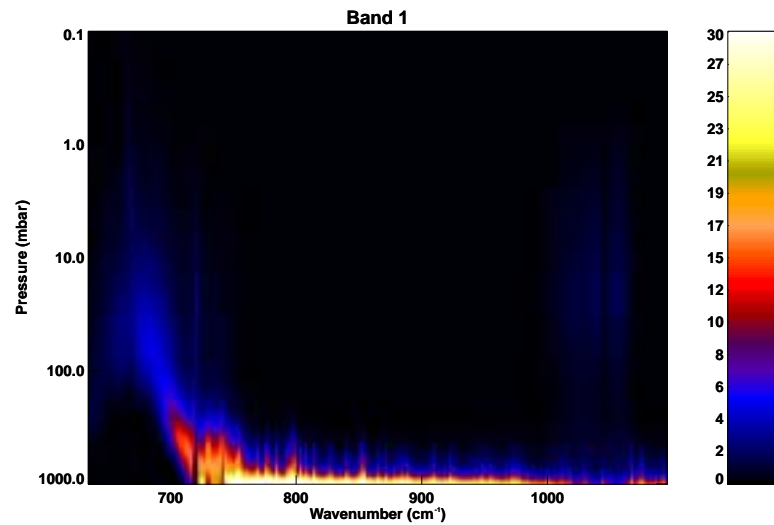


Figure 2: Temperature weighting function (in arbitrary units) in a spectral range that includes LWIR.

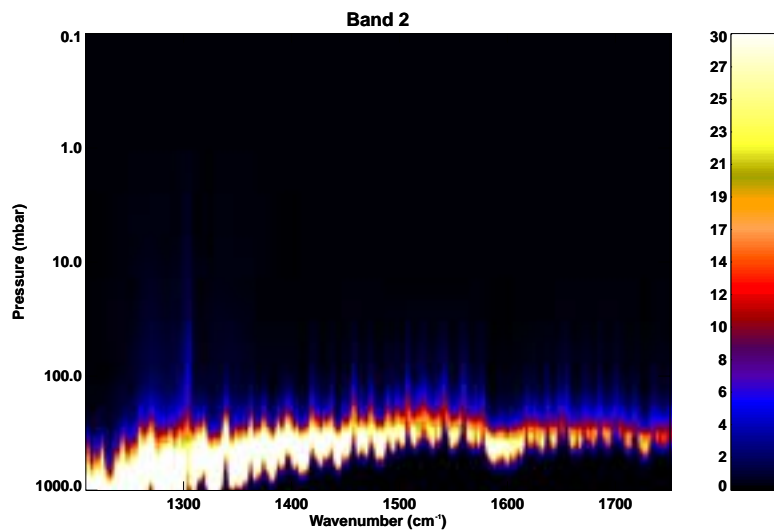


Figure 3: Temperature weighting function (in arbitrary units) in a spectral range that includes MWIR.

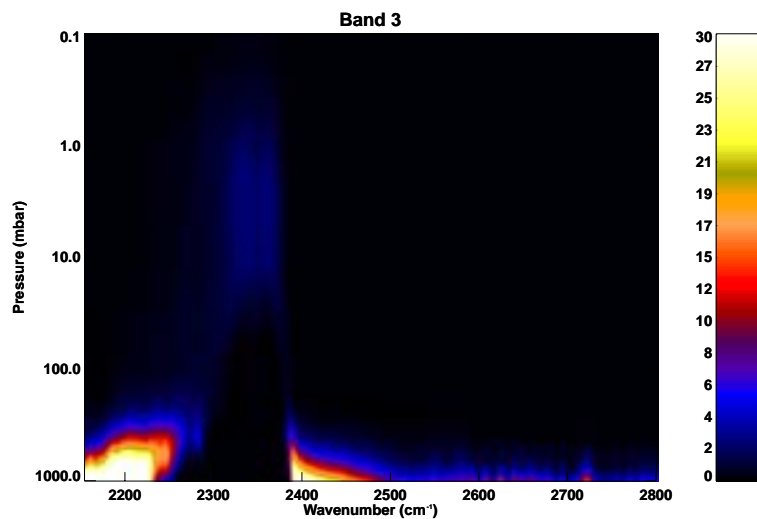


Figure 4: Temperature weighting function (in arbitrary units) in a spectral range that includes SWIR.

3.2 Microwave Instruments: AMSU and MHS

3.2.1 AMSU

AMSU is a cross-track scanning microwave radiometer with 15 spectral channels (23 GHz - 89 GHz). The AMSU channels and their specifications are given in Table 8 (channels 1 to 15). AMSU consists of 12 channels within the 50-60 GHz portion of the oxygen band to provide temperature and precipitation information. In addition, AMSU contains three window-channels at 24, 31, and 89 GHz to provide total precipitable water, cloud liquid water content, and precipitation measurements, respectively. These channels can be used to provide information on sea-ice concentration and snow cover. The 3-dB beam diameter of AMSU is 3.3°, corresponding to about 45 km at nadir. Each cross-track scan produces 32 sets of measurements (30 Earth looks, 1 dark space calibration, and 1 internal blackbody radiometric calibration). The scan repeats every 8 seconds.

3.2.2 MHS

MHS is a cross-track scanning microwave radiometer with 5 spectral channels (89 GHz - 183 GHz). The MHS channels and their specifications are also given in Table 8 (channels 16 to 20). Like AMSU, MHS contains a channel at 89 GHz to provide precipitation information (but at a higher spatial resolution). MHS has one window-channel at 150 GHz to obtain high-resolution measurements of precipitation, snow cover, and sea-ice. Three additional channels in the 183 GHz water vapor line are used to retrieve atmospheric humidity profiles. The 3-dB beam diameter of an MHS FOV is 1.1°, corresponding to about 15 km at nadir. Each cross-track scan produces 92 sets of measurements (90 Earth looks, 1 dark space calibration, and 1 blackbody calibration). The scan repeats every 8/3 seconds. One AMSU FOV contains 9 (3x3) MHS FOVS, as shown in Figure 5.

Figure 6 shows the position of the AMSU and MHS channels on the microwave water vapor and oxygen absorption spectrum.

SECTION 3: CrIMSS INSTRUMENTS OVERVIEW

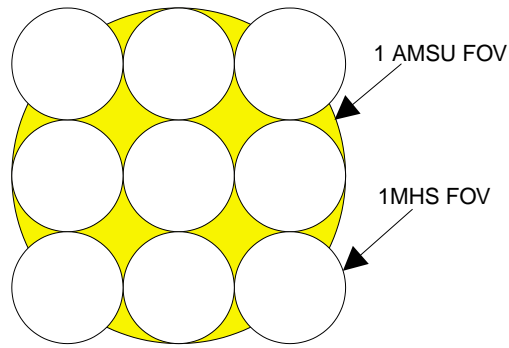


Figure 5: AMSU/MHS FOV Configuration.

Table 8: AMSU (1 to 15) and MHS (16 to 20) Channel Set.

Channel	Central Frequency	Side Band	Bandwidth	Primary Use
1	23.800	0.0	270	TPW
2	31.400	0.0	180	CLW
3	50.300	0.0	180	Temperature
4	52.800	0.0	400	Temperature
5	53.596	± 0.115	170	Temperature
6	54.400	0.0	400	Temperature
7	54.940	0.0	400	Temperature
8	55.500	0.0	330	Temperature
9	57.290	0.0	330	Temperature
10	57.290	0.217	78	Temperature
11	57.290	$\pm 0.322 \pm 0.048$	36	Temperature
12	57.290	$\pm 0.322 \pm 0.022$	16	Temperature
13	57.290	$\pm 0.322 \pm 0.010$	8	Temperature
14	57.290	$\pm 0.322 \pm 0.0045$	3	Temperature
15	89.000	0.0	6000	CLW
16	89.000	± 0.9	1000	CLW
17	150.000	± 0.9	1000	Water vapor
18	183.310	± 1.0	500	Water vapor
19	183.310	± 3.0	1000	Water vapor
20	183.310	± 7.0	2000	Water vapor

SECTION 3: CrIMSS INSTRUMENTS OVERVIEW

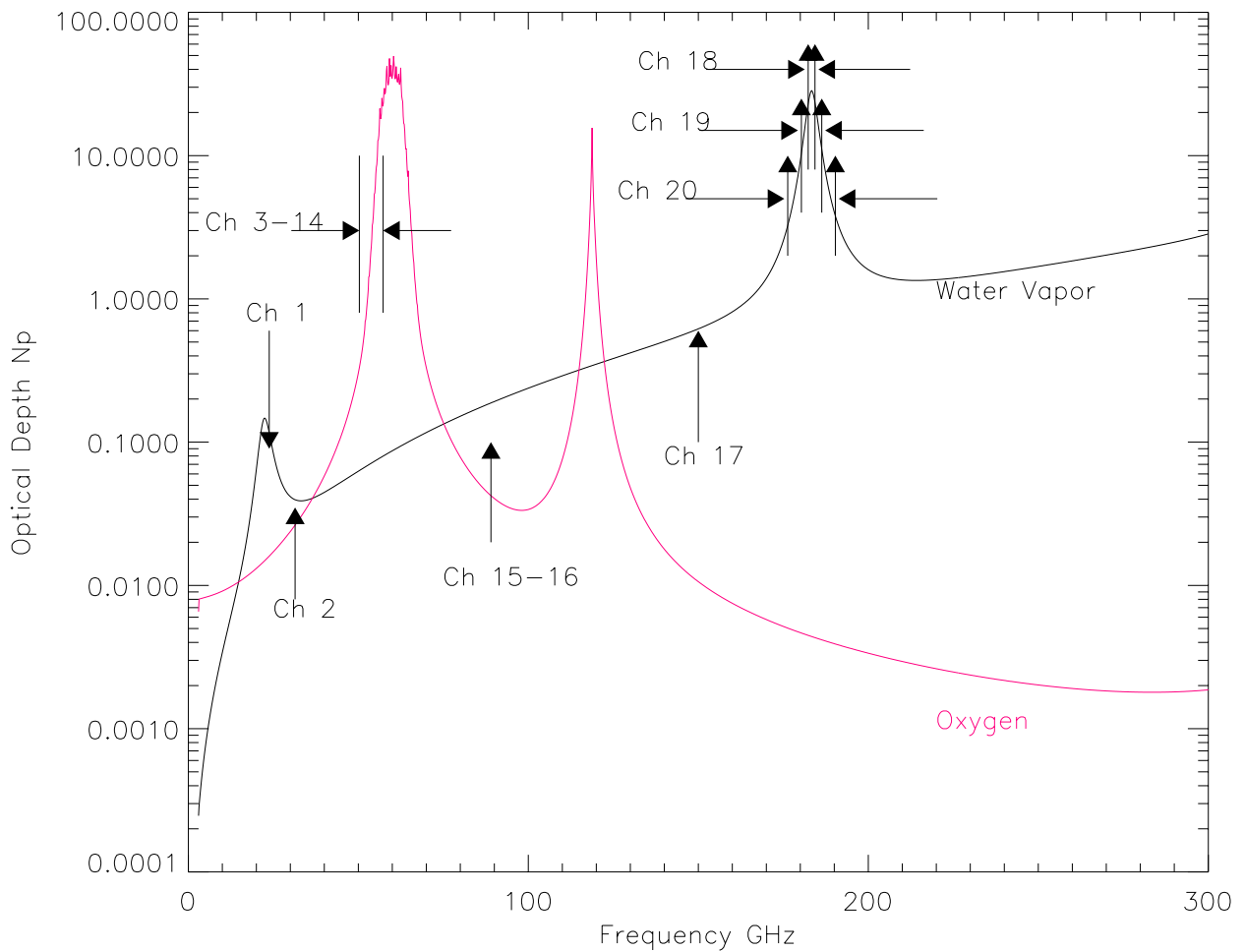


Figure 6: Channels Position for AMSU (1 to 15) and MHS (16 to 20).

4 CrIMSS ALGORITHM OVERVIEW

Figure 7 presents the top-level flow diagram for the CrIMSS retrieval algorithm. The algorithm consists of seven modules (shown enclosed in rectangular boxes in Figure 7):

1. Initialization
2. Input and pre-processing
3. Microwave-only retrieval
4. Scene classification
5. Joint microwave and infrared retrieval
6. Quality control
7. Output and post-processing

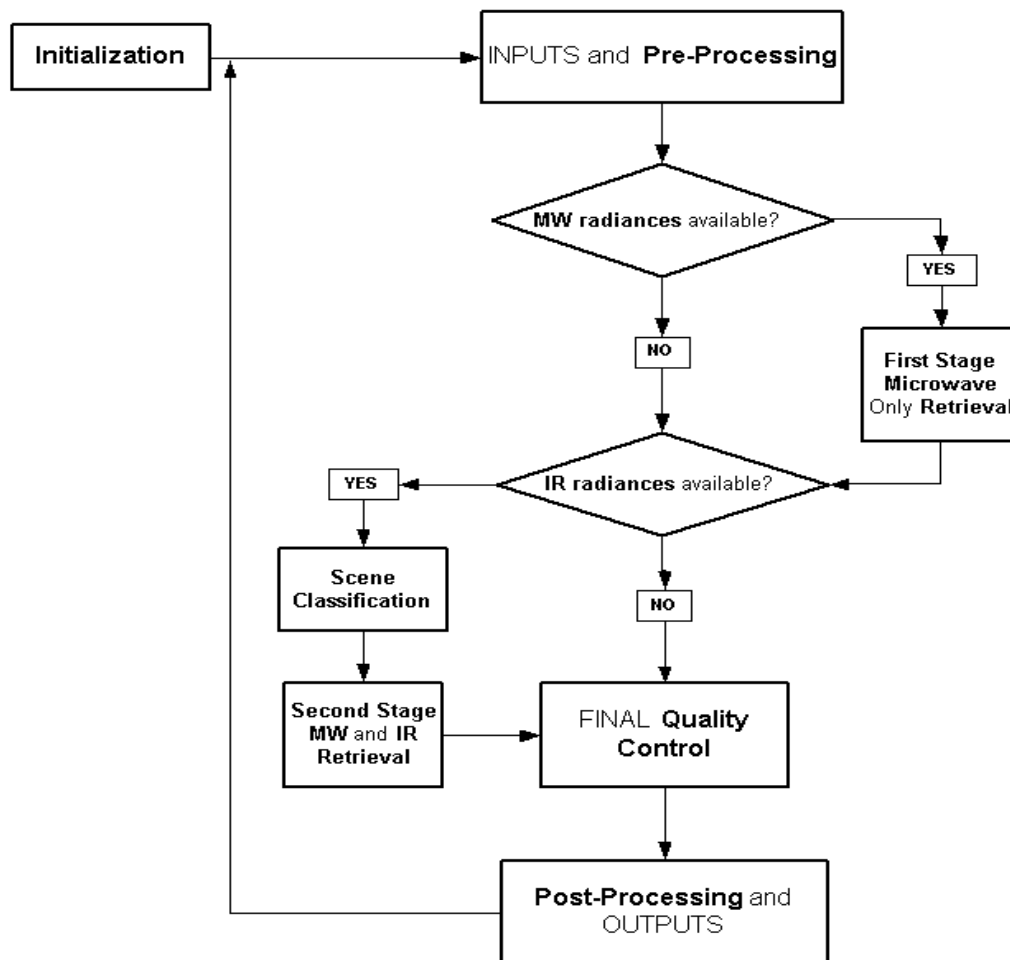


Figure 7: CrIMSS EDR Algorithm Flow Diagram.

SECTION 4: CrIMSS ALGORITHM OVERVIEW

The CrIMSS algorithm utilizes a fast radiative transfer (forward) model and an inversion algorithm, both of which share common features between the microwave and infrared parts of the retrieval. They are two key elements of the CrIMSS algorithm and their general description is presented in sections 5 and 6, respectively. Another critical consideration in the design of an infrared retrieval algorithm concerns the treatment of clouds and a brief overview of retrieval strategies under cloudy conditions is provided in Section 7. The remainder of this ATBD is devoted to the description of the individual modules of the CrIMSS algorithm.

5 FORWARD MODEL

One of the most critical components of a remote sensing retrieval algorithm is the radiative transfer model (also referred to as the forward model). The forward model is used to compute radiances corresponding to a given atmospheric and geophysical state (temperature, water vapor and ozone profiles, surface properties, cloud properties, etc.) and the derivatives (or Jacobian) of the radiances with respect to atmospheric and surface parameters for use by the inversion module. The forward model should also be able to accurately model the Instrument Line Shape (ILS) function or Spectral Response Function (SRF). In addition to being accurate, the forward model must meet stringent requirements on computational time. This section presents the Optimal Spectral Sampling (OSS) technique that has been developed at AER and applied to construct a highly accurate and computationally efficient forward model for the CrIMSS algorithm. Being a monochromatic method, the OSS technique has the advantage over other fast forward model parameterizations in providing the required derivatives analytically, with little extra computation time.

5.1 RT Equation in the Microwave

The radiative transfer equation (RTE) used in the microwave region treats the atmosphere as an inhomogeneous, plane-parallel, nonscattering medium. The brightness temperature R_ν at frequency ν is computed using the Rayleigh-Jeans approximation:

$$R_\nu \cong \varepsilon_\nu \Theta_s T_{s,\nu} + \int_{p_s}^0 \Theta(p) \frac{\partial T_\nu(p, \theta_u)}{\partial p} dp + (1 - \varepsilon_\nu) T_{s,\nu} \left[\int_0^{p_s} \Theta(p) \frac{\partial T_\nu^*(p, \theta_d)}{\partial p} dp + T_\nu^*(0, \theta_d) \Theta_c \right]$$

Equation 1

where $\Theta(p)$ is the atmospheric temperature at pressure p , $T_\nu(p, \theta_u)$ is the total transmittance due to molecular species and cloud liquid water from pressure p to space at the satellite viewing angle θ_u , $T_\nu^*(p, \theta_d)$ is the transmittance from surface to pressure p at computational angle θ_d , ε_ν is the surface emissivity, and Θ_c is the cosmic radiation term ($\Theta_c = 2.73$ K). In the microwave, over both land and ocean, the surface is treated as specularly reflective, i.e. $\theta_d = \theta_u$.

5.2 RT Equation in the Infrared

The general form of the RTE in the infrared for an inhomogeneous, plane-parallel, nonscattering medium can be written as:

$$\begin{aligned}
 R_v = & \varepsilon_v B_v(\Theta_s) T_{s,v} + \int_{p_s}^0 B_v(\Theta(p)) \frac{\partial T_v(p, \theta_u)}{\partial p} dp \\
 & + 2T_{s,v} \int_0^{\pi/2} \rho_v(\theta_d, \theta) \left[\int_0^{p_s} B_v(\Theta(p)) \frac{\partial T_v^*(p, \theta)}{\partial p} dp \right] \sin \theta \cos \theta d\theta \\
 & + \rho_v T_{s,v} T_v(p_s, \theta_{sun}) F_{0,v} \cos \theta_{sun}
 \end{aligned}$$

Equation 2

where $B_v(\Theta(p))$ is the Planck function emission, $F_{0,v}$ is the solar irradiance, θ_{sun} is the solar zenith angle, and ρ_v is the bi-directional surface reflectance. The third term in Equation 2 represents the contribution of the reflected downwelling thermal radiation to the observed radiance.

A proper treatment of the angular integral in Equation 2 would require information about the anisotropy in the downwelling radiances caused by the anisotropy in the reflective properties of the surface. In practice, because of the non-homogenous nature of the atmosphere and the fact that bi-directional reflectance distribution functions (BRDF) for natural land surfaces are poorly known, the usefulness of such a level of sophistication for a 1-D retrieval problem is uncertain. At the present stage of development of the CrIS EDR algorithm, the following form of RTE is used to address the case of specular and Lambertian surfaces:

$$\begin{aligned}
 R_v \cong & \varepsilon_v B_v(\Theta_s) T_{s,v} + \int_{p_s}^0 B_v(\Theta(p)) \frac{\partial T_v(p, \theta_u)}{\partial p} dp \\
 & + (1 - \varepsilon_v) T_{s,v} \int_0^{p_s} B_v(\Theta(p)) \frac{\partial T_v^*(p, \theta_d)}{\partial p} dp \\
 & + \rho_v T_{s,v} T_v(p_s, \theta_{sun}) F_{0,v} \cos \theta_{sun}
 \end{aligned}$$

Equation 3

where $\theta_d = \theta_u$ for specular surfaces and $\theta_d \approx 53^\circ$ for Lambertian surfaces. The treatment adopted in the Lambertian case corresponds to the use of a single “diffusivity” angle, which provides a good approximation to the explicit angular integral when the downwelling radiance field is isotropic.

The single-angle integration is valid over ocean, where the specular assumption is a reasonable approximation, and for densely vegetated land surfaces, for which the BRDFs are nearly isotropic. More complex land surface types need to be considered in future work. In particular, land surface types such as sand, snow, senescent vegetation, as well as inhomogeneous pixels (e.g. mixture of land and water bodies) often display highly non-Lambertian characteristics (Snyder et al. 1998). As a future enhancement to the current algorithm, a separate retrieval of thermal reflectivity over land and coastal regions is being considered. Appropriate constraints will be used to tie the spectral thermal reflectivity to the emissivity as a function of geographical location, season, and surface/vegetation type.

5.3 Overview of the OSS Method

Optimal Spectral Sampling (OSS) is a general approach to radiative transfer that is applicable from the microwave through the ultraviolet regions of the spectrum and that can be used with any ILS (or SRF). In this approach, the top-of-atmosphere (TOA) radiance for each instrument channel is represented as a linear combination of radiances computed at selected monochromatic locations within the domain spanned by the ILS

$$R_{\Delta\nu}(\nu) = \frac{\int_{\Delta\nu} \phi(\nu - \nu') R(\nu') d\nu'}{\int_{\Delta\nu} \phi(\nu - \nu') d\nu'} = \sum_i w_i R_{\nu_i} + err$$

Equation 4

where ν_i belongs to some selected interval $\Delta\nu$ around the “central” frequency ν and $\phi(\nu - \nu')$ is the instrument function (assumed to vanish when ν' is outside the interval $\Delta\nu$). The optimal selection of the frequencies ν_i and weights w_i is performed off-line by comparing radiances

derived from the OSS formulation with those obtained using a reference line-by-line (LBL) model. The optimization procedure minimizes RMS differences between the reference and approximate radiances for an ensemble of globally representative atmospheric profiles and the full range of satellite viewing angles. The error term on the right-hand side of Equation 4 expresses the degree of approximation in this scheme and determines the number of points used in Equation 4 for each channel. For the current CrIS forward model, this term was set to 0.05 K.

For a localized ILS or SRF, the following constraints are applied in order to ensure a physical solution

$$w_i > 0 \quad \text{and} \quad \sum_i w_i = 1$$

Equation 5

The positive coefficient constraint serves as a sign control that prevents the instability of the selection process. In their paper describing the Exponential Sum Fitting Transmittance (ESFT) approach, Wiscombe and Evans (1977) pointed out that the appearance of a negative coefficient indicates linear dependence of some selected points and can lead to ill-conditioning in the least-squares fitting process. However, for a non-localized ILS the sign control is not a good constraint, since negative coefficients are physically allowed for spectral regions in which the side-lobes of the non-localized ILS are negative. An alternative approach to avoiding ill-conditioning relies on controlling the value of the determinant of the inversion matrix in the least squares fitting process and is combined with a statistical Monte Carlo search (see Appendix 1). It is flexible and allows control of the determinant values and of statistically rejecting configurations of points characterized by small values of the determinant.

Two methods have been adopted for selecting the monochromatic spectral points and their associated weights. For a localized ILS (such as *Blackman* for CrIS) or SRF for AMSU/MHS, a sequential search, similar to that used by Wiscombe and Evans (1977) for ESFT, is implemented with constraints listed in Equation 5. However, this method is not practical for a non-localized ILS (such as *Hamming* or *Sinc*), since sign control needs to be replaced in this case by determinant control and this results in a significant increase in the numbers of points required to fit the “true” radiances. Because of this, for a non-localized ILS the sequential search has been

replaced by a more efficient Monte Carlo (MC) method described in Appendix 1. This method can be used for both localized and non-localized ILS.

Note that if the second constraint in Equation 5 is not explicitly enforced, it can still be approximately realized with a fairly high accuracy for a localized ILS. For example, when modeling apodized radiances without this constraint for *Blackman*, the sum rule is still valid with an accuracy of about 10^{-3} . However, the situation changes dramatically when the number of side lobes reaches a few tens. For the *Hamming* instrument function with 40 side lobes, the value of the sum ranges between 0.7 and 1.3 if the sum rule is not enforced explicitly. For the *Sinc* ILS, the sum can even turn negative values for some instrument channels. Consequently, we have chosen to work with the sum rule, as expressed in Equation 5, but without confining the coefficients to positive values. Instead, we used the determinant control (see Appendix 1).

Before making the final selection using appropriate CrIS ILS, several pre-selections may be done using a localized ILS. Sequential search is appropriate for pre-selecting OSS points from the initial monochromatic uniform grid by using a boxcar ILS. It is convenient to perform the pre-selection in a few steps, keeping the selection threshold at 0.025 K. In LWIR, for example, the initial monochromatic frequency spacing in the LBL calculations is $1.0 \times 10^{-4} \text{ cm}^{-1}$. The 1st pre-selection is done for a boxcar ILS with a Full Width at Half Maximum (FWHM) of $5 \times 10^{-3} \text{ cm}^{-1}$. Next, three hierarchical steps are used. In each step, five adjacent boxcars are joined together to form a boxcar for the next step. The combined points in the new boxcar will be further eliminated in the next OSS selection process. The fitted radiances of a new boxcar are defined as averages over predecessors. Completing the hierarchical steps, a set of spectral points and weights is selected to represent a boxcar ILS with FWHM equal to 0.625 cm^{-1} . It should be noted that in order to save computational time, the pre-selection is performed assuming a constant value of surface emissivity. A set of monochromatic transmittances at the selected monochromatic frequency points is saved and monochromatic radiances with variable surface emissivity values are calculated from these transmittances.

The final selection for each channel is both ILS- and emissivity-dependent and is performed within a spectral range that covers the entire ILS (e.g., for a *Sinc* ILS, all points in CrIS LWIR are used). The output from this process includes the selected frequencies, their weights, and the

corresponding monochromatic radiances. Optical depth tables of various atmospheric gases at different atmospheric temperatures and at the selected frequencies are then generated using a LBL model. Section 5.5 describes how the CrIMSS forward model calculates infrared and microwave radiances using information resulting from this procedure.

5.4 Implementation of the OSS Method

This section describes the application of the OSS method to the modeling of CrIMSS radiances. The number of points selected for each instrument channel will be discussed and results of validation studies for the OSS forward model will be presented. The issue of modeling non-localized ILS for CrIS will also be discussed. It should be noted that the RMS differences shown in this section do not include errors due to optical depth interpolation with respect to temperature. These errors can be made arbitrarily small by increasing the number of temperature entries in the optical depth look-up tables (see Section 5.5.1).

5.4.1 Infrared

In the infrared, the OSS method has been successfully applied to both apodized and unapodized radiances. The method takes advantage of the fact that the OSS selection depends mainly on the local features in the radiance spectrum and on the spectral resolution and the information about the shape of the ILS is carried mostly by the weights. In other words, for a given spectral resolution, the total number of points necessary to represent a given portion of the spectrum is approximately the same for a non-localized and a localized ILS. Hence, there is no or little increase in computational speed with unapodized ILS for the monochromatic transmittance calculations. However, for an unapodized ILS a potential increase in computational time can originate from two factors: 1. A larger number points out of the total set of selected points are needed to reconstruct a given channel and 2. The assumption that the Planck function is constant over the interval spanned by the ILS is no longer valid.

A training set of 32 atmospheric profiles from the TIGR database (Chedin et al. 1985) has been adopted to select OSS spectral locations and weights. The line-by-line radiative transfer model adopted as reference in the infrared is the LBLRTM model (Clough et al. 1992). LBLRTM is

originally based on FASCODE and has been extensively validated against atmospheric measurements (Snell et al 1995). Numerical simulations have been performed with a strongly localized ILS (*Blackman*), an “intermediate” ILS (*Hamming*), and a non-localized ILS (*Sinc*). Test studies have shown that the contributions of *Blackman* side lobes beyond the central peak are negligible, as are the contributions from *Hamming* side lobes beyond 40. On the other hand, the side lobes of *Sinc* only become negligible outside of the CrIS bands, with the result that near the band edges, the shape of a *Sinc* ILS is strongly asymmetric.

Figure 8 shows the number of monochromatic spectral points per channel needed to model a *Sinc* ILS in the three CrIS bands, with similar figures for *Blackman-3 π* and *Hamming-40 π* shown in Appendix 1. In the window spectral region, only a few points are required for any ILS. However, for a non-localized ILS more monochromatic spectral points are needed to model each CrIS channel. This is mitigated by the duplication of spectral points selected for different channels, with the result that the total number of independent spectral points needed to model a non-localized ILS is only slightly larger than for a localized ILS. The numbers of points selected in the three CrIS channels are summarized in Table 9 through Table 11.

A factor that has an impact on the OSS selection is the treatment of surface emissivity. The results described thus far pertain to the case of a flat emissivity of 1. To simulate variable emissivity, hinge points separated by 20 wavenumbers have been chosen within the CrIS spectral bands, the emissivities at the hinge points have been assigned random values between 0.85 and 0.98, and the emissivities at frequencies located between the hinge points have been obtained by linear interpolation. The number of points selected per channel is shown in Figure 9 for three apodization functions (although selection for variable emissivity was performed in all three bands, only results for SWIR are shown). As shown in Table 9, Table 10, and Table 11, the average number of OSS points selected in the case of variable emissivity is larger than for their flat counterparts.

A set of 50 atmospheric profiles, independent of those used in the OSS selection process, has been adopted to validate the CrIS OSS forward model. The validation involves a comparison between radiances generated using the OSS forward model for these profiles at randomly varying scan angles and radiances obtained by convolving the appropriate ILS with the

monochromatic radiances obtained using LBLRTM. Figure 10 shows the RMS differences between the two sets of radiances in the case of an unapodized ILS and for a flat emissivity (figures for *Blackman-3 π* and *Hamming-40 π* are shown in Appendix 1), while the validation results for variable emissivity in SWIR are shown in Figure 11. It should be noted that the results shown in Figure 11 were obtained assuming random emissivities for both the training and the independent profiles; the OSS training set based on the flat emissivity produces much larger RMS differences if variable emissivity is assumed for the independent profiles.

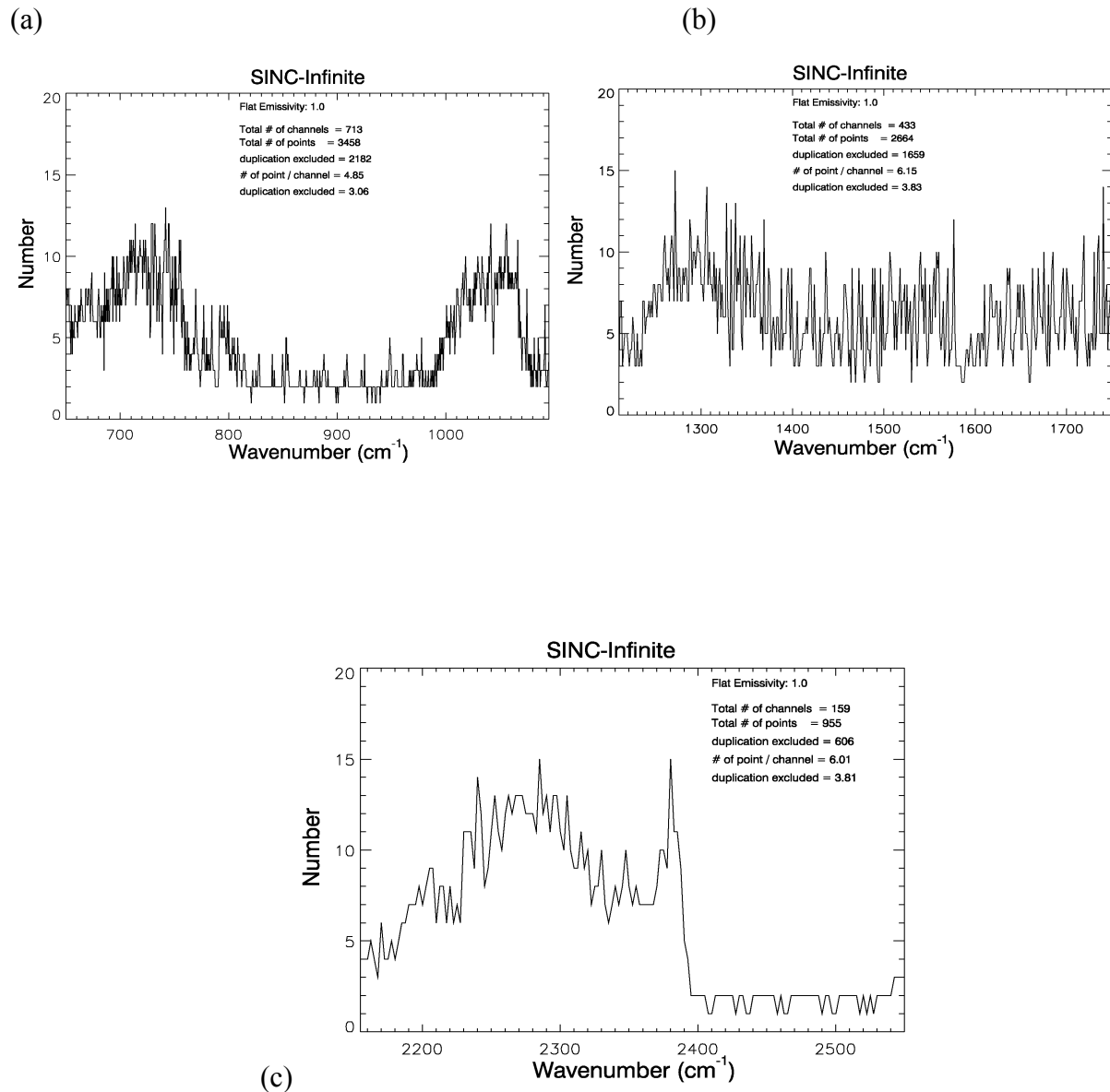


Figure 8: Number of spectral points per channel selected for *Sinc* ILS:
(a) LWIR, (b) MWIR, (c) SWIR.

SECTION 5: FORWARD MODEL

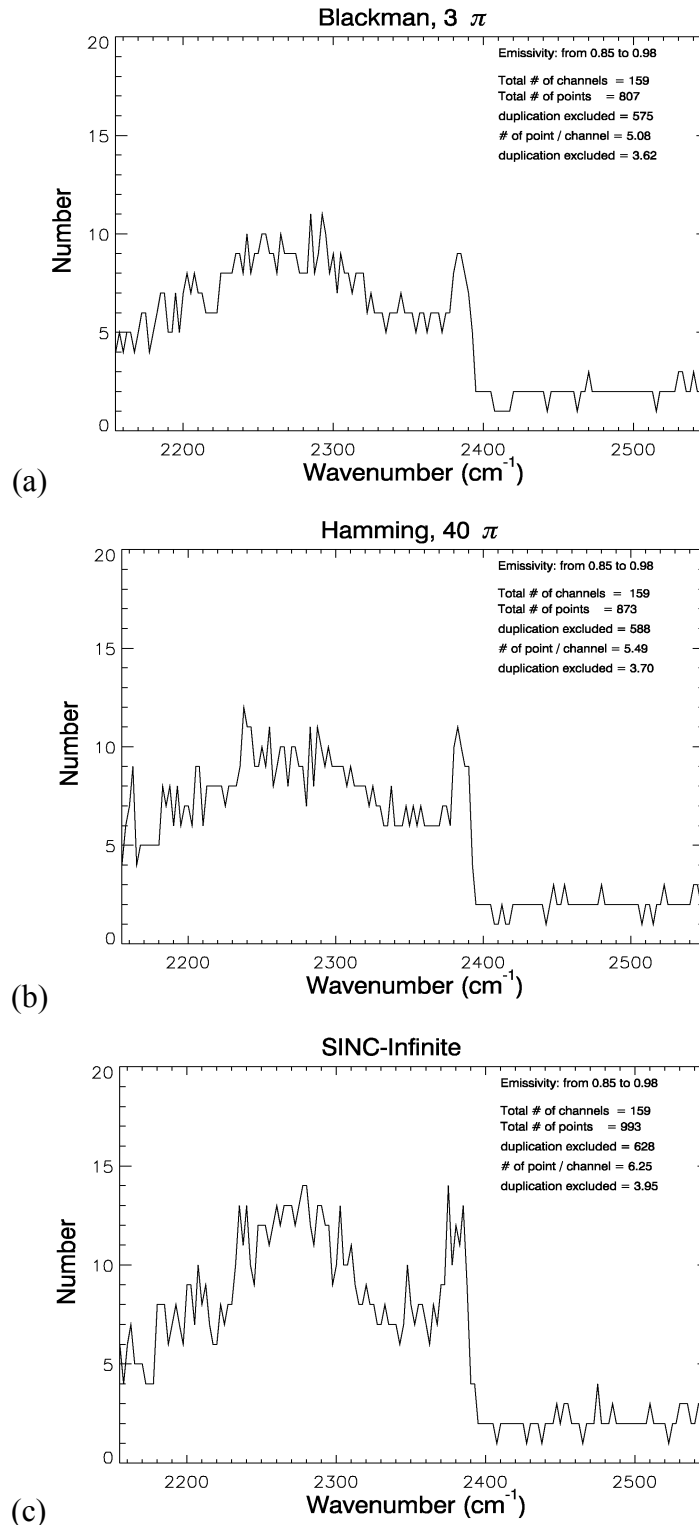


Figure 9: Number of spectral points selected in SWIR with variable surface emissivity for (a) *Blackman* ILS, (b) *Hamming* ILS, (c) *Sinc* ILS.

SECTION 5: FORWARD MODEL

Table 9: Number of OSS points in LWIR.

ILS	Emissivity	Number of Channels	Number of Points: Total / per Channel	Number of Points without Duplication: Total / per Channel
Blackman	1.0	713	3093 / 4.34	2127 / 2.98
Hamming			3075 / 4.31	2023 / 2.77
Sinc			3458 / 4.85	2182 / 3.06
Blackman			3313 / 4.65	2201 / 3.09
Hamming	from 0.85 to 0.98	713	3402 / 4.77	2207 / 3.10
Sinc			4250 / 5.96	2455 / 3.43

Table 10: Number of OSS points in MWIR.

ILS	Emissivity	Number of Channels	Number of Points: Total / per Channel	Number of Points without Duplication: Total / per Channel
Blackman	1.0	433	2372 / 5.48	1594 / 3.68
Hamming			2362 / 5.45	1537 / 3.55
Sinc			2664 / 6.15	1659 / 3.83
Blackman			2405 / 5.55	1617 / 3.73
Hamming	from 0.85 to 0.98	433	2439 / 5.63	1566 / 3.62
Sinc			2790 / 6.44	1702 / 3.93

Table 11: Number of OSS points in SWIR.

ILS	Emissivity	Number of Channels	Number of Points: Total / per Channel	Number of Points without Duplication: Total / per Channel
Blackman	1.0	159	795 / 5.00	567 / 3.57
Hamming			837 / 5.26	562 / 3.53
Sinc			955 / 6.01	606 / 3.81
Blackman			807 / 5.08	575 / 3.62
Hamming	from 0.85 to 0.98	159	873 / 5.49	588 / 3.70
Sinc			993 / 6.25	628 / 3.95

SECTION 5: FORWARD MODEL

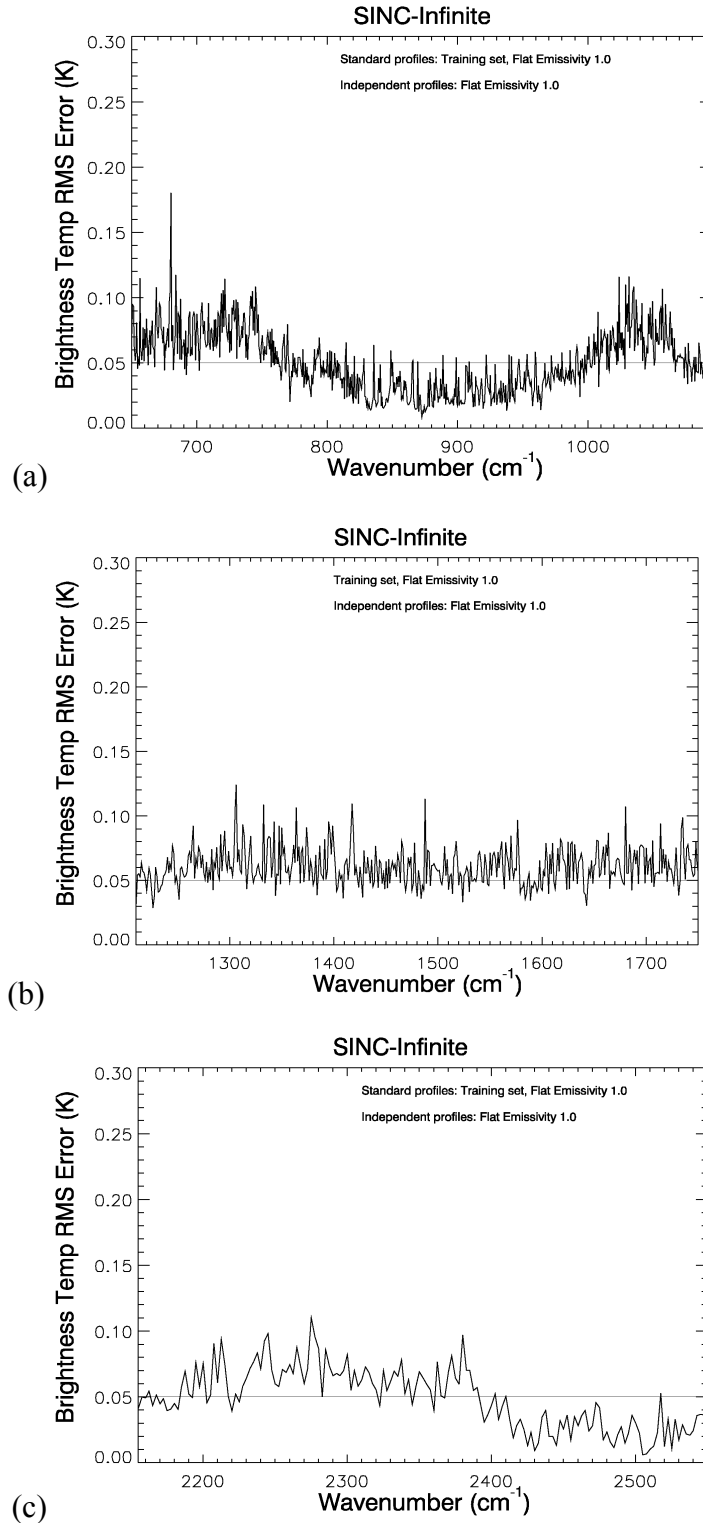


Figure 10: RMS differences between OSS-generated and true radiances for *Sinc* ILS.
(a) LWIR, (b) MWIR, (c) SWIR.

SECTION 5: FORWARD MODEL

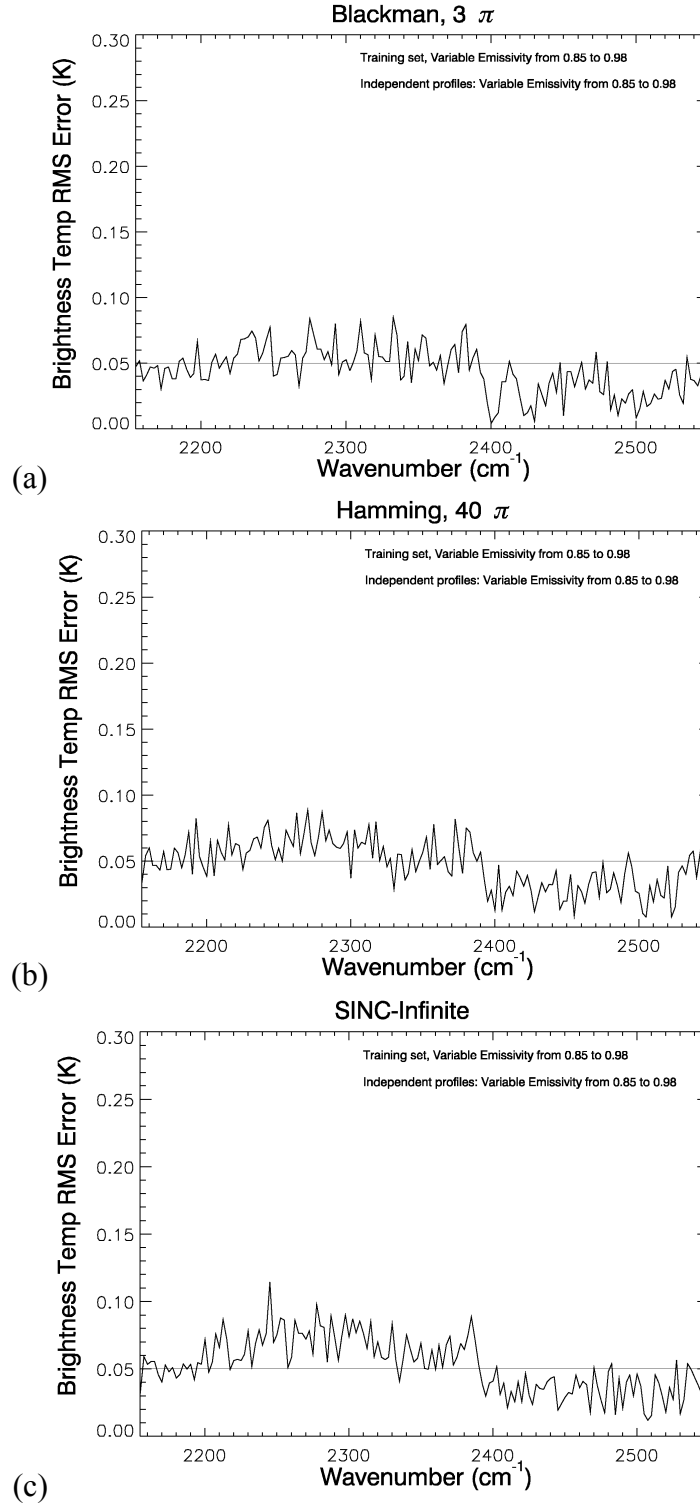


Figure 11: RMS differences between OSS-generated and true radiances in SWIR with variable surface emissivity for training and independent profiles. (a) *Blackman-3 π* , (b) *Hamming-40 π* , (c) *Sinc*.

SECTION 5: FORWARD MODEL

While the validation results shown above indicate that the band-averaged RMS error for OSS forward model is about 0.05 K, some channels have errors larger than this preset threshold. These channels are generally located in spectral regions with large atmospheric emission (e.g., the CO₂ spectral regions). A straightforward way to increase the accuracy of the OSS forward model would be to lower the accuracy threshold, but this could lead to a significant increase in the number of selected points. To mitigate this problem, only channels with RMS errors larger than 0.05 K should be re-selected using a lower threshold (e.g. 0.045 K). For channels that have RMS errors larger than 0.05 K after the 0.045-K selection, another re-selection should be done with an even lower threshold (e.g. 0.04K), etc. and the process should be repeated until the RMS errors for all channels are within 0.05 K. This approach has been used with the *Hamming* ILS, with the results for LWIR shown in Figure 12. Since only a small number of channels exceeds the original 0.05-K threshold, the overall number of points increases by less than 15% when the threshold is lowered in selected channels (the overall increase is less than 10% for the case of flat emissivity).

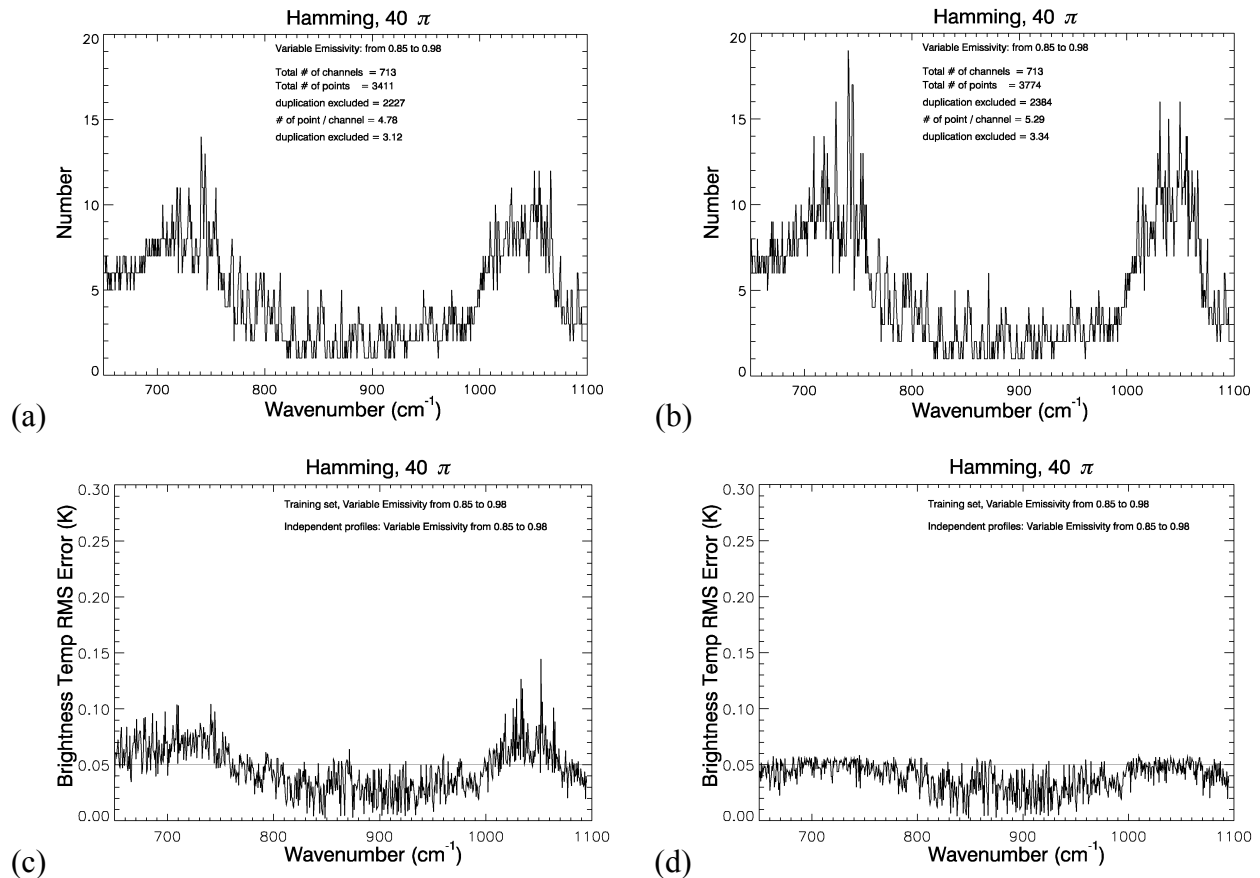


Figure 12: LWIR, *Hamming*-40 π ILS, variable emissivity.

Number of spectral points and RMS error differences:

(a) and (c) with a constant threshold; (b) and (d) with a variable threshold.

Another approach to the validation of the OSS method utilizes the so-called transformation between apodized and unapodized spectra. Details of such transformation are described in Appendix 1. In brief, the radiances for an apodized ILS are expressed using radiances computed for an unapodized ILS and compared with radiances computed directly for the apodized ILS. The RMS errors for the transformation from *Sinc* to *Blackman-3 π* and *Hamming-40 π* are plotted in Figure 13 for LWIR. The errors in Figure 13 are on the order of 0.05 K and this can be interpreted in two ways. If it is known (from an independent validation) that the OSS method for *Sinc* is accurate to 0.05 K, then the results shown in Figure 13 validate the method for *Blackman-3 π* and *Hamming-40 π* (in general, the transformation errors are sensitive to the truncation of the side-lobes). Alternatively, if *Blackman-3 π* or *Hamming-40 π* are independently validated, then the results shown in Figure 13 validate the OSS method for the *Sinc* function.

In general, the accuracy of the OSS model depends on the atmospheric profiles used in the training and validation. The 32 training profiles and 50 validation profiles span the range of variability encountered in the TIGR database, but they may not be representative of other climatological datasets, e.g., NOAA-88 (in fact, the NOAA-88 atmospheres appear moister than the TIGR atmospheres). More work is needed to select training and validation profiles that are likely to produce results applicable to the widest possible variety of atmospheric conditions.

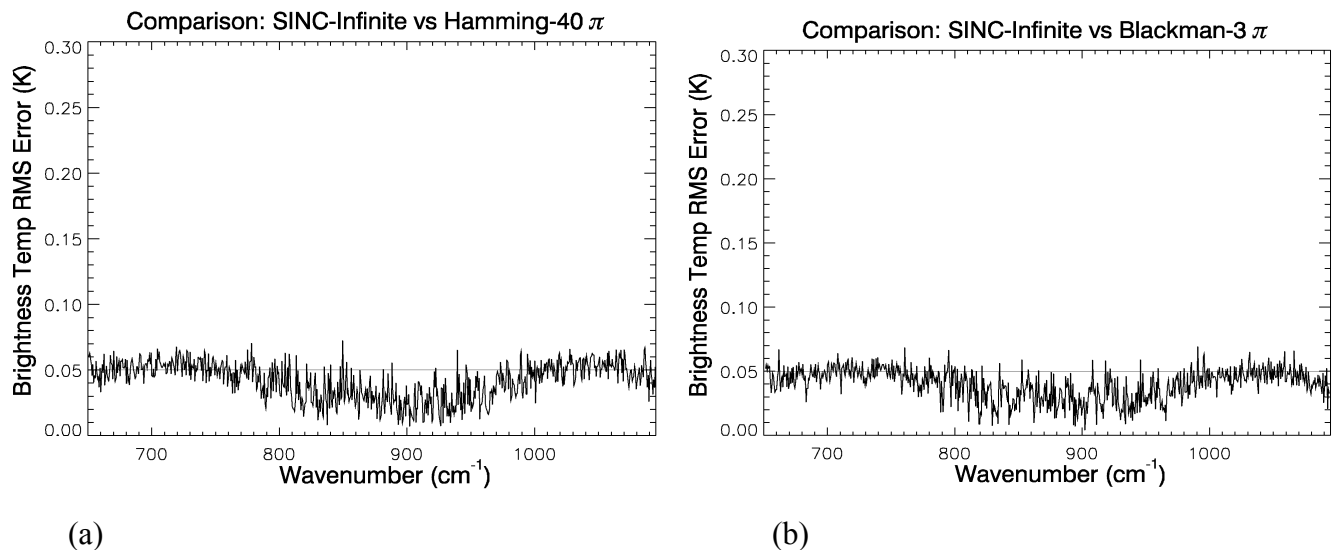


Figure 13: LWIR, variable emissivity. Transformation between *Sinc* with unlimited number of side-lobes and (a) *Blackman-3 π* , (b) *Hamming-40 π* .

5.4.2 Microwave

In the microwave, the OSS forward model has been trained using the line-by-line radiative transfer model of Rosenkranz (1995). This model is easier to use than LBLRTM in the microwave region and includes a complete treatment of the Zeeman effect (however, the results presented in this section have been obtained without including this effect and the impact of this omission remains to be evaluated). Since the AMSU/MHS SFRs are localized, a sequential search method is used to perform the OSS selection.

Table 12 shows the number of OSS points used in the modeling of AMSU and MHS radiances. The average RMS error resulting from validation using independent profiles is 0.0135 K, which is much smaller than the 0.05 K threshold. This is because the instrument SRF is smaller than the spectral features for AMSU and MHS channels. Spectral variations within the SRF are relatively small. The total number of monochromatic points needed to model all 20 channels is 48 (2.4 points per channel).

Table 12: Number of Spectral Points Selected in the MW.

Channel Number	Center Frequency (GHz)	Number of OSS Frequencies	RMS
1	23.800	1	0.0009
2	31.400	1	0.0019
3	50.300	1	0.0060
4	52.800	3	0.0042
5	53.596	3	0.0049
6	54.400	3	0.0016
7	54.940	3	0.0263
8	55.500	3	0.0168
9	57.290	1	0.0188
10	57.290	3	0.0221
11	57.290	3	0.0310
12	57.290	3	0.0290
13	57.290	3	0.0258
14	57.290	3	0.0378
15	89.000	2	0.0006
16	89.000	2	0.0005
17	150.000	2	0.0025
18	183.310	2	0.0164
19	183.310	3	0.0066
20	183.310	3	0.0166

Figure 14 compares brightness temperatures in the AMSU (1 to 15) and MHS (16 to 20) channels obtained with the OSS approach and the “central frequency” approximation with the “exact” calculations from Rosenkranz’s model.

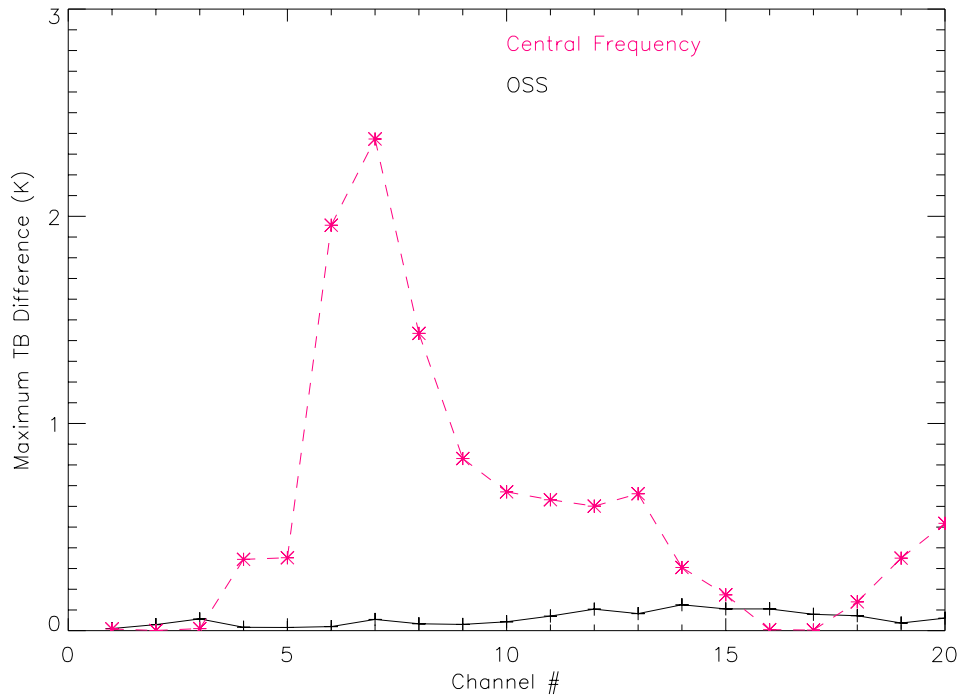


Figure 14: Comparison OSS/Central Frequency (Maximum Differences).

5.5 Radiance Calculations in the OSS forward model

Computation of radiances and derivatives with the OSS method uses a generic recursive scheme developed for the modeling of upward, downward-looking and limb-viewing instruments and used in atmospheric retrievals from CIRRIS (Miller *et al.* 1999).

5.5.1 Optical Depth Tables

To compute transmittances and radiances, the OSS model makes use of pre-computed monochromatic layer optical depths for the relevant atmospheric gases at the wavenumber locations selected by the OSS method. The gases are split into two groups, those that have a fixed molecular amount and those that are variable. Because a single optical depth represents the

fixed gases this grouping reduces storage requirements for the optical depth tables. For each species, the optical depths are stored at a set of temperatures for each pressure layer used in the discrete radiative transfer model. For each layer this temperature range spans the temperatures expected for that layer based on the profiles in the TIGR and NOAA-88 databases.

The optical depth tables are calculated using the LBLRTM radiative transfer model along with the molecular amounts from the US Standard Atmosphere profile (Anderson *et al.* 1986). Because of the formulation adopted for the water vapor continuum in the LBLRTM model (Clough *et al.* 1989), the method of optical depth calculation has been modified slightly for water vapor, since the self-broadened component of the water vapor continuum contains a quadratic dependence on the number density. As such the self-broadened component is separated from the water lines and the foreign-broadened component of the continuum. Absorption coefficients of water vapor lines and foreign broadened continuum are grouped together in one table. A second table contains absorption coefficients of self-broadened water vapor continuum.

For a given layer each optical depth is linearly interpolated to the layer temperature. The correct optical depths for the variable species are then obtained by multiplying the temperature-interpolated optical depth by the ratio of the actual layer amount to the standard amount. This is equivalent to multiplying the species' molecular absorption coefficients by their molecular amounts, but it reduces numerical accuracy problems caused by the many orders of magnitude difference in the values of the absorption coefficient and the molecular amount. Of minimal impact, and thus neglected in the current formulation, is the difference in the self-broadened component of the line shape between the standard density used to compute the stored optical depths and the actual layer density.

In the infrared, the total optical depth τ_l^o for layer l at nadir is computed as the sum of contributions from the fixed and variable gases:

$$\begin{aligned}\tau_l^o = & \tau_{fx}(\bar{p}_l, \Theta_l) + (k_{H_2O}(\bar{p}_l, \Theta_l) + k_{H_2O}^{self}(q_{H_2O}, \Theta_l)\omega_{H_2O} + k_{O_3}(\bar{p}_l, \Theta_l)\omega_{O_3} \\ & + \tau_{CH_4}(\bar{p}_l, \Theta_l) + \tau_{CO}(\bar{p}_l, \Theta_l) + \tau_{N_2O}(\bar{p}_l, \Theta_l)\end{aligned}$$

Equation 6

where κ is the absorption coefficient, ω is the absorber amount, p is the layer pressure, and Θ is the temperature. The current set of optical depths is stored at selected monochromatic spectral points for 39 pressure layers and 10 temperatures. The optical depth tables in the microwave are structured in a similar way as in the IR, with minor differences because of the nature of the microwave spectrum. The total optical depth is computed for each layer l at nadir as:

$$\tau_l^0 = \tau_{O_2+N_2}(\bar{p}_l, \Theta_l, \omega_{H_2O}) + \tau_{H_2O}(\bar{p}_l, \Theta_l, \omega_{H_2O})$$

Equation 7

where the variables are defined as in the infrared equation given above. The microwave optical depths are computed using the model of Rosenkranz (1995) and are tabulated as functions of temperature and water vapor. Simulation studies indicate that 20 temperature and water vapor interpolation points are required for an accurate OSS representation under a wide variety of atmospheric conditions.

5.5.2 Radiance and derivative calculation

Figure 15 defines the numbering conventions for the layered atmosphere. T_l and T_l^* denote the transmittances from space to level l and from surface to level l , respectively. They are defined as:

$$T_l = \exp\left(-\sum_{i=1}^l \tau_i^0 \sec \theta_{obs}\right)$$

Equation 8

$$T_l^* = \exp\left(-\sum_{i=l+1}^N \tau_i^0 \sec \theta_d\right)$$

Equation 9

SECTION 5: FORWARD MODEL

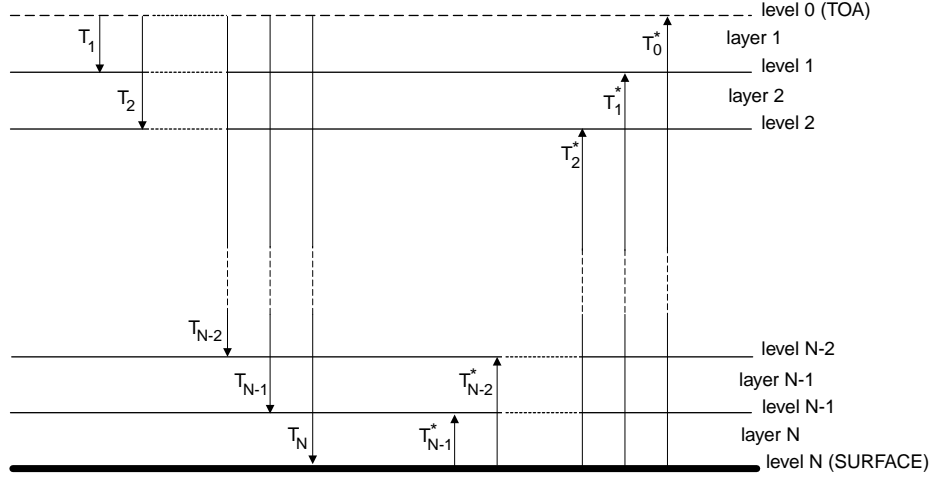


Figure 15: Numbering convention for the atmospheric layers used by OSS.

Radiances R in clear conditions are computed using the following expression derived by discretizing the radiative transfer equation (Equation 1 and Equation 2):

$$R_v = \sum_{i=1}^N (T_{v,i-1} - T_{v,i}) B_{v,i}^+ + \varepsilon_{vs} T_{v,N} B_{v,s}^+ + (1 - \varepsilon_{vs}) T_{v,N} \sum_{i=1}^N (T_{v,i}^* - T_{v,i-1}^*) B_{v,i}^-$$

Equation 10

where B_v^\pm represents the upward and downward Planck emission of the layer/surface and ε_{vs} is the surface emissivity. Derivatives of R_v with respect to constituent concentrations and temperature in layer l are obtained by differentiating the previous equation:

$$\begin{aligned} \frac{\partial R}{\partial X_l} = & -\frac{\partial \tau_l^0}{\partial X_l} \left\{ \left[-T_l B_l^+ + \sum_{i=l+1}^N (T_{i-1} - T_i) B_i^+ + T_N \varepsilon_s B_s^+ + (1 - \varepsilon_s) T_N \sum_{i=1}^N (T_i^* - T_{i-1}^*) B_i^- \right] \sec \theta_{obs} \right. \\ & + \left. \left[-(1 - \varepsilon_s) T_N T_{l-1}^* B_l^- + (1 - \varepsilon_s) T_N \sum_{i=1}^{l-1} (T_i^* - T_{i-1}^*) B_i^- \right] \sec \theta_d \right\} \\ & + \frac{\partial B_l^+}{\partial X_l} (T_{l-1} - T_l) + (1 - \varepsilon_s) T_N \frac{\partial B_l^-}{\partial X_l} (T_l^* - T_{l-1}^*) \end{aligned}$$

Equation 11

or, by introducing the two-path attenuation from level l to space, $T_l' = (1 - \varepsilon_s) T_N T_l^*$:

$$\begin{aligned} \frac{\partial R}{\partial X_l} = & -\frac{\partial \tau_l^0}{\partial X_l} \left\{ \left[-T_l B_l^+ + \sum_{i=l+1}^N (T_{i-1} - T_i) B_i^+ + T_N \epsilon_s B_s^+ + \sum_{i=1}^N (T'_i - T'_{i-1}) B_i^- \right] \sec \theta_{obs} \right. \\ & \left. + \left[-T'_{l-1} B_l^- + \sum_{i=1}^{l-1} (T'_i - T'_{i-1}) B_i^- \right] \sec \theta_d \right\} + \frac{\partial B_l^+}{\partial X_l} (T_{l-1} - T_l) + \frac{\partial B_l^-}{\partial X_l} (T'_l - T'_{l-1}) \end{aligned}$$

Equation 12

where X_l stands for either Θ_l or ω_l^m .

With the exception of the handling of the surface terms, the recursive procedure for the integration of the RTE and the calculation of derivatives over a reflective surface is similar to the one used for limb viewing. This procedure uses the fact that a perturbation in temperature or constituent concentration in any given layer of the atmosphere does not affect the emission in the atmospheric slab comprised between this layer and the observer. Therefore, derivatives can be obtained at low cost if the RTE is integrated by adding layers sequentially in the direction of the observer. The procedure is more apparent by introducing the quantities Σ_l^- and Σ_l^+ defined as the contribution to the observed radiance of the downward emission (reflected at the surface) from the atmosphere above level l and the contribution of the atmosphere below level l plus reflected downward radiation, e.g.:

$$\Sigma_l^- = \sum_{i=1}^l (T'_i - T'_{i-1}) B_i^-$$

Equation 13

and

$$\Sigma_l^+ = \sum_{i=l+1}^N (T_{i-1} - T_i) B_i^+ + \epsilon_s T_N B_s^+ + \sum_{i=1}^N (T'_i - T'_{i-1}) B_i^-$$

Equation 14

Using the definitions of the previous equations, one can write:

$$\begin{aligned} \frac{\partial R}{\partial X_l} = & \left[\frac{\partial R}{\partial X_l} \right]_d + \left[\frac{\partial R}{\partial X_l} \right]_u = \left[\frac{\partial \tau_l^d}{\partial X_l} (-\Sigma_{l-1}^- + B_l^- T'_{l-1}) + \frac{\partial B_l^-}{\partial X_l} (T'_l - T'_{l-1}) \right] \\ & + \left[\frac{\partial \tau_l^u}{\partial X_l} (-\Sigma_l^+ + B_l^+ T_l) + \frac{\partial B_l^+}{\partial X_l} (T_{l-1} - T_l) \right] \end{aligned}$$

Equation 15

In this equation we used the following definitions: $\tau_l^d = \tau_l^0 \sec \theta_d$ and $\tau_l^u = \tau_l^0 \sec \theta_{obs}$.

In the current version of the CrIMSS algorithm, the dependence of atmospheric transmittances on temperature is neglected in the calculations of derivatives in the infrared channels

$$\partial \tau_l^0 / \partial \Theta_l = 0$$

Equation 16

This assumption is made for the sake of computational efficiency only and the code can handle the general case of $\partial \tau_l^0 / \partial \Theta_l \neq 0$ without difficulty (it should be noted that even with this extra term included, the computational cost of computing derivatives in the OSS model is always at least an order of magnitude lower than in finite-difference methods). Another more critical approximation concerns the treatment of layer-averaged emission. In the current version of the code, the layer emission is computed using the Planck function evaluated at the density-weighted mean temperature $\bar{\Theta}$ for the layer

$$B_l^+ = B_l^- = B(\bar{\Theta})$$

Equation 17

with the result that $\partial B_l / \partial \tau_l = 0$. The above approximation to the layer-mean Planck function is adequate as long as layers are not optically thick, e.g. vertical pressure grid is sufficiently fine and no cloud is present. A preliminary trade study has revealed that this approximation can produce occasional errors exceeding 0.5 K on the currently adopted 40-level grid (the errors are computed as radiance residuals relative to a reference calculation utilizing a 196-level grid). In future versions of the algorithm, these errors could be reduced by adopting alternative definitions of $\bar{\Theta}$ (e.g., using water-density rather than air-density weighting to compute $\bar{\Theta}$) and/or more sophisticated approaches to the computation of layer-mean emission, such as the linear-in-tau or Pade approximations (Clough et al. 1992).

5.6 Practical Implementation

In a first pass, at any given wavenumber, the algorithm computes the profile of transmittance from space. The recursive procedure for the computation of radiances and analytical derivatives follows equation (16):

- 1) Initialization: set $\Sigma_0^- = 0$.
- 2) If $(1 - \epsilon_s)T_N > 10^{-4}$, add layers successively from TOA down to surface. Update Σ_l^- at each step and compute first part of radiance derivatives:

$$\Sigma_l^- = \Sigma_{l-1}^- + (T_l' - T_{l-1}')\bar{B}_l$$

Equation 18

$$\left[\frac{\partial R}{\partial \tau_l} \right]_d = -\Sigma_{l-1}^- + \bar{B}_l T_{l-1}'$$

Equation 19

$$\left[\frac{\partial R}{\partial \Theta_l} \right]_d = \frac{\partial \bar{B}_l}{\partial \Theta_l} (T_l' - T_{l-1}')$$

Equation 20

- 3) Add surface term and compute derivatives with respect to skin temperature and surface emissivity

$$\Sigma_N^+ = \Sigma_N^- + T_N \epsilon_s B_s$$

Equation 21

$$\frac{\partial R}{\partial \Theta_s} = T_N \epsilon_s \frac{\partial B_s}{\partial \Theta_s}$$

Equation 22

$$\frac{\partial R}{\partial \varepsilon_s} = T_N B_s - \Sigma_N^- / (1 - \varepsilon_s)$$

Equation 23

4) Update Σ_l^+ by adding layers from surface up to TOA and compute second part of derivatives

$$\Sigma_{l-1}^+ = \Sigma_l^+ + (T_{l-1} - T_l) \bar{B}_l$$

Equation 24

$$\frac{\partial R}{\partial \tau_l} = -\Sigma_l^+ + \bar{B}_l T_l + \left[\frac{\partial R}{\partial \tau_l} \right]_d$$

Equation 25

$$\frac{\partial R}{\partial \Theta_l} = \frac{\partial \bar{B}_l}{\partial \Theta_l} (T_{l-1} - T_l) + \left[\frac{\partial R}{\partial \Theta_l} \right]_d$$

Equation 26

5) Set $R_v = \Sigma_0^+$ and compute derivatives with respect to temperature and layer amounts for all molecular species.

$$\frac{\partial R}{\partial \omega_l^m} = \frac{\partial R}{\partial \tau_l} \times k_l^m, \quad m = 1, \dots, M$$

Equation 27

5) Background terms. In the microwave, the cosmic background is computed as

$$R_{\cos} = (1 - \varepsilon_v) T_N^2 \Theta_c$$

Equation 28

with $\Theta_c = 2.73$ K. The solar contribution to the observed radiance is computed as

$$R_{sol} = \rho_s T_N F_0 \cos \theta_{sun} \exp\left(-\sum_l \tau_l^0 \sec \theta_{sun}\right)$$

Equation 29

and the derivative is computed as

$$\partial R_{sol} / \partial \tau_l^0 = -(\sec \theta_{obs} + \sec \theta_{sun}) R_{sol}$$

Equation 30

5.7 Treatment of Clouds

5.7.1 Microwave

Cloud optical depths in the microwave are represented at the central frequency for each channel by two parameters, total liquid water Q and top pressure p_t , and they are computed as the sum of optical depths in each atmospheric layer. The cloud optical depths τ_{ij} for frequency index i and layer j are given as:

$$\tau_{ij} = Q k_{ci}(\bar{\Theta}_j^c) f \frac{\Delta_j}{\Delta}$$

Equation 31

where k_{ci} is the mass absorption coefficient for liquid water, $\bar{\Theta}_j^c$ is the average temperature of the cloud within layer j , and f is the cloud fraction within the FOR. The cloud proportion in layer j is equal to $\frac{\Delta_j}{\Delta}$, where Δ_j is the cloud thickness in layer j and Δ is the total cloud thickness (such that the cloud base pressure $p_b = p_t + \Delta$). If the entire cloud depth is within layer j , then $\Delta_j = \Delta$. For CrIMSS, Δ is held constant and the cloud proportions depend on the location of the cloud within the atmospheric grid. The absorption coefficients are computed from the model of Liebe *et al.* (1991) using an exponential formulation for the primary relaxation frequency dependence on temperature:

$$\gamma_1 = 20.1 \exp(7.88\theta), \quad \theta = 1 - \frac{300 \text{ K}}{T}$$

Equation 32

Derivatives with respect to total cloud liquid and cloud top are obtained from:

$$\frac{\partial \tau_{ij}}{\partial Q} = k_{ci}(\bar{\Theta}_j^c) f \frac{\Delta_j}{\Delta}$$

Equation 33

$$\frac{\partial \tau_{ij}}{\partial p_t} = Q k_{ci}(\bar{\Theta}_j^c) f \frac{1}{\Delta} \frac{\partial \Delta_j}{\partial p_t}$$

Equation 34

5.7.2 Infrared

Except for the calculation of cloud absorption coefficients, the OSS forward model is capable of treating clouds in the IR in way similar to that adopted for the MW. However, as described in Section 12, the method adopted in the current code for the treatment of clouds in the IR is cloud-clearing and this does not require the modeling of cloud properties. In radiance simulations, non-transmissive clouds are simulated by moving the surface to the cloud top pressure level in the RT calculation. The cloud parameters needed are top pressure, emissivity, and reflectivity.

6 INVERSE MODEL

The inversion methodology adopted for both microwave and infrared is based on a constrained non-linear least squares approach (e.g., Rogers 1976). The solution to the inverse problem is found by minimizing a cost function of the form:

$$\phi(x) = \|y_o - F(x)\|^2 + g(x)$$

Equation 35

where the first term is the error associated with the unconstrained solution and the second term is the penalty function which constrains the solution. The vectors y_o and $F(x)$ represent observed radiances and radiances calculated using the forward model, respectively. If both the state vector and the radiances are characterized by Gaussian distributions, then the cost function has the form

$$\phi(x) = [y_o - F(x)]^T S_y^{-1} [y_o - F(x)] + (x - x_a)^T S_x^{-1} (x - x_a)$$

Equation 36

where S_y is an error covariance matrix describing the measurement and other errors and x_a and S_x are the background (*a priori*) vector and the associated error covariance matrix, respectively. An iterative solution to the inverse problem can be obtained by minimizing this cost function via a Gauss-Newton method. When the second derivative of $F(x)$ is neglected, the solution x_{i+1} at the $(i+1)^{\text{th}}$ iteration, given the solution x_i at the i^{th} iteration, is equal to

$$x_{i+1} = x_a + (K_i^T S_y^{-1} K_i + S_x^{-1})^{-1} K_i^T S_y^{-1} [y_o - y_i + K_i (x_i - x_a)]$$

Equation 37

where y_i is the current value of $F(x)$ linearized about x_a and K_i is the matrix containing partial derivatives of y_i with respect to x . This form of solution for the state vector is used in the joint microwave and infrared retrieval. For the microwave-only retrieval, in which the number of retrieved variables exceeds the number of channels, an equivalent form is employed in order to accelerate the solution

$$x_{i+1} = x_a + S_x K_i^T (K_i S_x K_i^T + S_y)^{-1} [y_o - y_i + K_i (x_i - x_a)]$$

Equation 38

The need for an *a priori* constraint relates to the fact that the inversion problem is generally ill-conditioned, e.g. the existence of null-space of the observing system leads to a non-uniqueness of solution. The use of *a priori* information, when available, is a way to ensure that the derived solution is physically acceptable. This information may be used to stabilize the solution and control the step size. The background covariance constraint introduces inter-level correlation in the temperature and moisture profiles, which prevents the solution from being unstable, particularly in the microwave-only retrieval. There are some concerns that if the constraint is biased, it will introduce errors into the solution. To ensure a successful retrieval, the covariance must be derived from a large ensemble of independent measurements that describe large variability in the state parameters. For atmospheric temperature and moisture profiles, S_x is derived from global radiosonde and rocketsonde measurements that meet the variability requirement. For the joint MW+IR retrieval, there is more information due to the increase in the number of channels, and therefore the solution is much less dependent on the background error covariance.

6.1 Linearization Noise

A major shortcoming of the standard Gauss-Newton procedure is that it does not account for errors due to linearization. In high-resolution spectra, these linearization errors have high frequency structures, which resemble pseudo random noise. Ignoring this error term degrades the rate of convergence when the problem is highly non-linear or when the first-guess is far away from the solution. It is implied that the “best” solution is one that fits the observation within the model noise, i.e., it ignores the fact that the linear model cannot fit the observation better than:

$$\varepsilon_{NL}(x) = F(x) - F(x_0) - K(x - x_0)$$

Equation 39

There are two consequences of failing to take $\varepsilon_{NL}(x)$ into account:

- For univariate problems there is a risk of overshooting, which may slow down convergence rate.

- For multivariate optimization problems, where conditioning is marginal, it destabilizes the solution by giving too much weight to the unconstrained solution. This tends to overfit the radiances and to introduce spurious structures in the solution vector due to amplification of non-linear noise (e.g., for cloud parameters spurious structure moves the result further away from the actual solution and convergence may never be reached).

An acceptable solution for a certain class of multivariate optimization problems (such as atmospheric profiling) is to reduce the dimension of the state vector at the beginning of the iterative process and increase it progressively as the solution gets closer to the truth. This avoids the problem of noise amplification. Such a method has been successfully applied for ozone profiling (Snell et al. 1999). However, this procedure is not applicable for loosely correlated parameters such as cloud optical depth and cloud top altitude. For such problems, ill conditioning can be avoided by estimating the linearization error from the radiance residuals.

6.2 Non-Linear Physical Inversion Method for CrIMSS

The maximum likelihood method, which is essentially the inverse Hessian method, attempts to minimize the errors in the measurement space based on the assumption that the cost function is quadratic (Press *et al.* 1992, Clough *et al.* 1995). When x is far away from the solution, or $F(x)$ is very non-linear, the quadratic cost function may be a poor local approximation. In this case, the inversion may be unstable if the solution step is too large.

The standard Levenberg-Marquardt (L-M) algorithm (Levenberg 1944, Marquardt 1963) uses a control parameter λ to choose between the inverse Hessian algorithm when the error is approximately quadratic and a more conservative approach, the steepest descent method, when the error is nonlinear in nature. We have implemented this technique, in combination with the maximum likelihood (ML), to test our retrieval algorithm. L-M is an improvement over the ML approach when the initial guess is far away from the solution. However, it is hard to find an optimal initial value and step size for λ which are applicable for all atmospheric conditions, since their values depend on the solution.

An ad-hoc method was devised based on extensive retrieval simulations. This method attempts to use information about the problem (e.g. the degree of non-linearity) in combination with the radiance residual, which is used as a measure of the distance from the truth, to provide a crude estimate of $\varepsilon_{NL}(x)$. In this approach the values of the covariance matrix of the modeling errors (the diagonal elements of S_y) are set to either some fraction of the error in the observed space, i.e., the difference between y_i and y_o , or to the noise variance:

$$S_y(j, j) = \max \left\{ \frac{1}{\alpha} [y_i(j) - y_o(j)]^2, \sigma^2(j) \right\}$$

Equation 40

where α is the error control parameter and $\sigma^2(j)$ is the instrument noise variance for the j^{th} channel. This is done for each iteration of the retrieval and the role of α is to limit the magnitude of Δx at each iteration step. The parameter α is relatively insensitive to the initial guess, with typical values ranging between 4 (for highly non-linear problems encountered in atmospheric remote sensing) and 100 for temperature inversion problems (tends toward ML result).

A comparison of the convergence characteristics of the above non-linear inversion algorithm (referred to as “DRAD”) with the L-M and ML methods, provided in Appendix 5, demonstrates an overall superior performance for the DRAD method. The most noticeable improvement in performance was achieved when the initial guess for each algorithm was based on climatology information. It is well known that cloud parameters change the radiative transfer equation in a highly non-linear way. It has been demonstrated that the DRAD method is capable of simultaneously solving for cloud parameters and atmospheric/surface parameters. This is an important consideration in selecting an appropriate inversion technique for an operational algorithm.

6.3 Eigenvector Transformation of Retrieved Parameters

Several methods to reduce the dimensionality of the inverse problem (and thus stabilize the solution) have been proposed in the literature (Pseudo Inverse, Single Value Decomposition). In the CrIMSS algorithm, this is achieved by projecting the state vector onto a set of pre-computed

Empirical Orthogonal Functions (EOFs). The EOFs are obtained by applying principal component analysis (PCA) to an error covariance matrix derived from a large ensemble of temperature and moisture profiles representative of global climatology. This procedure is described in detail in Appendix 3. The two main purposes of transforming x into the EOFs domain are: 1. Eliminating EOFs with small eigenvalues in order to stabilize the solution and 2. Reducing the number of retrieved parameters (and thus reducing the time needed for inversion).

When atmospheric profiles are retrieved at 40 vertical levels, the background covariance matrix is ill-conditioned for the upper level moisture profiles due to the lack of real measurements above 300 mb. Increasing the number of levels retrieved from 40 to 100 made this problem worse because inter-level correlation increases with the number of levels used to represent vertical profiles. The PCA approach avoids this potential problem. The number of retained EOFs is dependent on the noise and spectral resolution of the sensor. Trade studies for the CrIS instrument show that the temperature profiles may be represented by the first 20 EOFs derived from temperature covariance matrix, and moisture profiles by 10 EOFs derived from moisture covariance matrix (see Appendix 3).

It should be mentioned here that the iterative equation is not changed by the EOFs transformation. Before the inversion, $\Delta x = x_{i+1} - x_a$ and K_i are transformed into the EOFs domain according to the following equations:

$$\Delta \tilde{x} = U^T \Delta x$$

Equation 41

and

$$\tilde{K}_i = K_i U$$

Equation 42

where U is a matrix which contains only the selected significant EOFs. The diagonalization of S_x is given by:

$$\Lambda = U^T S_x U$$

Equation 43

The transformed retrieval equation may now be written as:

$$\Delta \tilde{x}_{i+1} = (\tilde{K}_i^T S_y^{-1} \tilde{K}_i + \Lambda^{-1})^{-1} \tilde{K}_i^T S_y^{-1} (y_0 - y_i + \tilde{K}_i \Delta \tilde{x}_i)$$

Equation 44

The microwave retrieval uses the same non-linear physical inversion scheme described above, except that the above equation is rearranged:

$$\Delta \tilde{x}_{i+1} = \Lambda \tilde{K}_i^T (\tilde{K}_i \Lambda \tilde{K}_i^T + S_y)^{-1} (y_0 - y_i + \tilde{K}_i \Delta \tilde{x}_i)$$

Equation 45

For the microwave retrieval, the above equation is computationally more efficient since the number of state vectors is more than the number of channels used in the retrieval. A flowchart for the inversion is shown in Figure 16.

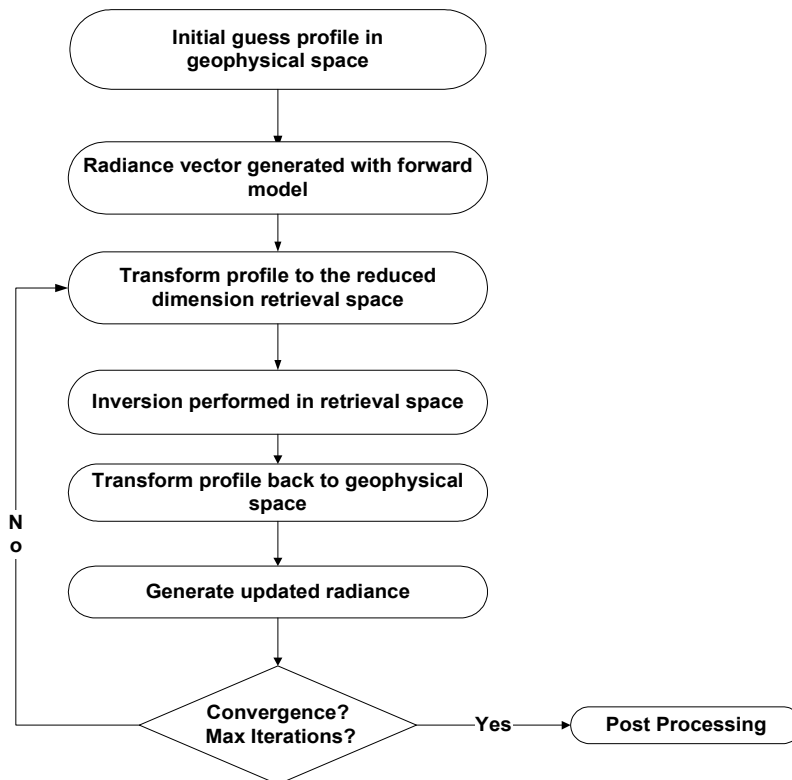


Figure 16: Inversion flowchart.

7 RETRIEVAL STRATEGIES UNDER CLOUDY CONDITIONS

A critical consideration in the design of an infrared retrieval process is the treatment of clouds. For the current size of the CrIS footprint size, the likelihood of cloud contamination within a FOR is high, for example the probability of one clear FOV is only 45%, whereas the probability of two clear FOVs is only 35% (Smith et al. 1996). Clouds are difficult to model in the IR radiative transfer because of multiple scattering effects, complex cloud geometry, multiple cloud layers with multiple reflection and scattering etc. A brief overview of three cloud-treatment methods is given in this section.

7.1 Cloud Clearing (CC)

The CC approach exploits the radiance contrasts between adjacent FOVs without modeling the cloud effects and performs a clear-sky retrieval on “cloud-cleared” radiances computed for each selected FOV cluster within one FOR. The method is based on the work by Smith (1968) and Chahine (1974, 1977) and it is the only cloud-treatment strategy currently implemented in the CrIMSS code. The implementation of the CC method in the CrIMSS algorithm is similar to that adopted in the AIRS code and is described in Appendix 6. The current implementation accommodates up to 8 cloud formations within one FOR (1 FOR contains 9 FOVs).

A potential shortcoming of the CC method is its underlying assumption that the only source of spatial inhomogeneities in the retrievals are due to clouds and that other atmospheric/surface constituents can be treated as spatially homogeneous.

7.2 Simultaneous Cloud Parameter Retrieval (SCPR)

In SCPR, cloud parameters (e.g. cloud top height and effective spectral emissivity) are retrieved in conjunction with the atmospheric temperature and constituent profiles. This method provides a single footprint capability in cloudy conditions and complements the CC approach in cases where the contrast between adjacent FOVs is low (e.g. low clouds, thin cirrus clouds, overcast situations) or when inhomogeneity prevents the application of the CC method. A brief description of the method is described section 12.4.

The disadvantage of SCPR is the high risk associated with the modeling of cloud optical properties (especially for ice clouds and when the cloud geometry is viewed at off-nadir angles), but this risk should diminish as our understanding of the radiative properties of clouds improves. In addition, SCPR is computationally slower than the CC method, because cloud parameters must be incorporated into the radiance model and the inversion method. Some of this computational loss can be mitigated for by our OSS forward model, which calculates the cloud parameter derivatives analytically.

7.3 Hole Hunting (HH)

HH identifies FOVs that are not contaminated with clouds and performs clear retrievals on these FOVs only. Measurements from high spatial resolution visible/infrared imaging instrument such as VIIRS could be used to detect the presence of clouds within a CrIS FOV. Another possible method of clear FOV detection involves a regression synthesis of microwave radiances using selected IR channels, as was done by Rizzi et al. (1994) for MSU-2 and HIRS data.

A serious drawback of the HH method is that it may fail to detect optically thin clouds, e.g., clouds with low cloud liquid amount or ice water path, clouds with very small fraction within a FOV, or very thin cirrus clouds. However, some of these clouds can strongly affect CrIS radiances and their non-detection can lead to large biases in the retrieved profiles. On the other hand, SCPR performs well under these circumstances. Therefore the HH method should be augmented with the SCPR, i.e., SCPR should be performed even if the HH method finds a clear FOV. If the scene is truly clear, the SCPR algorithm will retrieve zero cloud amounts.

As mentioned above, the approach adapted by the current CrIMSS algorithm is CC. However, when the cloud is optically thin and the radiance contrast between adjacent fields of views is small (or when the surface within a FOR is inhomogeneous), CC may not produce the best results. As a future technology insertion, the HH/SCPR approach could be used to improve the performance in these situations.

8 INITIALIZATION

The initialization process provides the “static” data (i.e., data that do not change with time) required by the retrieval algorithm. These include:

- Instrument specifications (AMSU and MHS frequencies and NEdT tables, CrIS frequencies and noise files, channel selection files)
- Forward model parameters (OSS optical depth tables for MW and IR, solar spectrum). In the current version of the code, the solar spectrum is approximated as Planck function at 5300 K, but this will be updated with a realistic spectrum in the future.
- Topography and land/ocean mask from a digital elevation map (DEM). Currently, the algorithm relies on the HRTPO map with 1/6° resolution for both purposes, but future plans include using the USGS GTOPO30 map for topography (more information about the map can be found in <http://edcwww.cr.usgs.gov/landdaac/gtopo30/gtopo30.html>).
- NWP time-independent surface elevation fields.
- Atmospheric mean profiles and background covariances for use by the inverse model. They have been derived separately for ocean and land using the NOAA-88 dataset.
- Covariance for MW surface emissivity. For ocean, it can be obtained using either the Wilheit (1979) or the Grody (1988) model. When using Wilheit’s model, random values of wind speed (between 0 and 20 m s⁻¹), surface temperature, and scan angle are used. For land, the emissivities are obtained either from Grody’s model or from the monthly-mean maps generated by Prigent et al. (1997) from SSM/I data.

9 INPUT AND PRE-PROCESSING

The main inputs to the CrIMSS retrieval algorithm are the calibrated microwave and infrared radiances.

9.1 Microwave SDR

The microwave SDR data are the AMSU and MHS radiances as specified by at the Goddard Space Flight Center in December 1995 for AMSU and by Matra Marconi in 1995 for MHS. Latitude and longitude for each AMSU and MHS FOV are provided within a 5 km mapping error, with the MHS data interpolated to AMSU footprints. NEdN and radiometric bias errors due to calibration and interpolation are associated with microwave SDRs.

9.2 Infrared SDR

The infrared SDRs consist of spectra apodized with a specified Instrument Line Shape (ILS) function and corrected for the off-optical axis effects (e.g., spectral shift, self-apodization, and phase distortion), with associated quality control flags. Information about NEdN, radiometric uncertainties, spectral shift errors, band-to-band co-registration errors, and line-of-sight (LOS) jitter errors are used to define the error covariance matrix for the infrared retrieval. Additional information in the infrared SDRs includes the scan angle, latitude and longitude for each CrIS FOV (5 km mapping error), and channel centers interpolated to the CrIS frequency grid defined in Table 7.

9.3 External Data Inputs

There external data required for the retrieval are of the “static” and “dynamic” type. The “static” database (i.e., information that is provided once and for all, and may or may not be updated as better information becomes available) is read in during initialization. The “dynamic” database is updated on a regular basis. It includes surface pressure and virtual temperature fields from an NWP model (to determine surface pressure at the CrIS footprint) and a microwave surface emissivity database.

Additional external data will be required if the microwave sensor is lost and other data could be used to improve the quality of retrievals under certain conditions.

9.3.1 Required Data in Case of Failure of the Microwave Instruments

- CMIS temperature and humidity EDR can be used as initial guess for the IR retrieval if AMSU becomes unavailable (taking into account that the CMIS swath is about 500 km smaller than AMSU).
- NWP fields are a second option to provide an initial guess for the IR retrieval, which will be required if CMIS is unavailable.

9.3.2 Optional Data for Performance Enhancement

- CMIS EDRs can be used for quality control of the retrieved products from the CrIMSS algorithm.
- CMIS instrument also provides surface skin temperature and emissivity, cloud liquid water content, and information on snow cover and ice.
- VIIRS can be used for cloud characterization, i.e., determination of the cloud fraction, the number of cloud formations, and the cloud height. This information could be used in the FOV selection for the CC method and in the quality control.
- Normalized Difference Vegetation Index (NDVI) and surface type, as well as information on snow cover and ice, can also be derived from VIIRS.
- NCEP forecasts for temperature and water vapor can be used as the initial guess for the microwave retrieval instead of climatology. An error covariance matrix associated with these profiles is also required.

9.4 Precipitation Check

Precipitation is detected prior to the retrieval process using the NESDIS algorithm (<http://orbit18i.nesdis.noaa.gov>). Over land, the algorithm applies a scattering index test using the 23 and 89 GHz channels (alternatively, the 89 and 150 GHz channels could be used). Over ocean, precipitation is detected using a cloud liquid water regression test based on the use of the

23, 31, and 50 GHz channels. If precipitation is detected, no retrieval is performed and the FOR is flagged accordingly. A possible alternative approach would be to ignore precipitation and perform a clear-sky IR retrieval (without MW channels). Such a retrieval may still provide useful information above the precipitating cloud, but it would require information about the cloud top (this could be obtained from external sources, e.g., VIIRS). Any retrieval problems caused by precipitation not detected during pre-processing will be identified during quality control (using chisq tests on MW radiances).

9.5 Surface Type Determination

Given the land/ocean mask, the AMSU brightness temperatures are used to classify the AMSU FOVs into one of the 6 following categories:

- ocean
- land
- ice
- snow
- coastal 1 (snow/ice)
- coastal 2 (ocean/land)

Figure 17 illustrates the decision tree for the surface type identification. The training for this scheme is based on the emissivity model of Grody (1988) which may not represent all land surface types. This surface type classification was successfully applied to the scan line scenes provided by IPO. Once the surface type is determined, the corresponding covariance matrix, which is trained with emissivities in that category, will be used in the retrieval. Another way to model the surface emissivity over land is to use the emissivity database derived by Prigent et al. (1997). This database has good global coverage and could be improved by using MSU/HIRS or future satellite sensors such as AMSU/HSB/AIRS. When the Prigent et al. database, which has more variations in surface emissivity, is used to simulate MW SDRs, it is difficult to classify the surface type into distinct surface types. In the current algorithm, two emissivity covariance matrices (ocean and land) are used for the microwave retrieval. The land covariance matrix

contains information about coastal surfaces. Further studies are needed to optimize the surface type classification scheme.

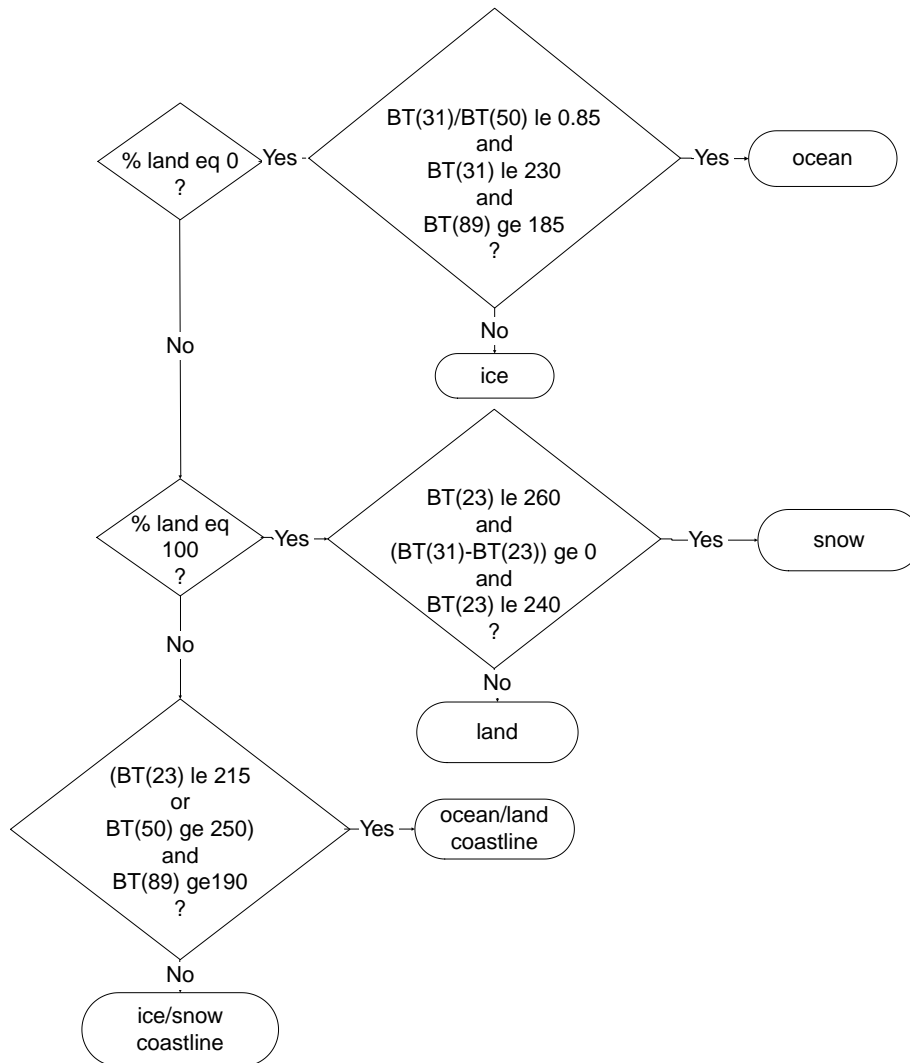


Figure 17: Surface Type Identification.

9.6 Surface Pressure Computation

Surface pressure at the center of a CrIS footprint is calculated using the hydrostatic equation, with inputs obtained from NWP surface pressure and virtual temperature fields and from a high-resolution digital elevation map (DEM). The meteorological data are obtained from an NWP model output and should be a past (prior to the satellite measurement) analysis field and a forecast field. Alternatively, two forecast fields surrounding the time of the satellite measurement can be used. The DEM is used to determine the local elevation. These high-resolution elevation

data are averaged over the CrIS footprint, taking into account the distortion in the shape of the CrIS FOV for off-nadir views. A detailed description of the inputs required for the computation of surface pressure is given below.

9.6.1 Hydrostatic Equation

The inputs required for the computation of surface pressure at a CrIS footprint include:

- NWP surface pressure P_{ref} interpolated to the center of the footprint
- NWP surface elevation H_{ref} interpolated to the center of the footprint
- DEM-derived surface elevation h averaged over the footprint
- Virtual temperature T_v interpolated to the elevation $h_m = (h + H_{ref})/2$. T_v is computed from temperature T and water vapor mixing ratio q (both of which are obtained from the gridded NWP fields) using the formula:

$$T_v = \frac{1 + q/\varepsilon}{1 + q} T$$

Equation 46

where $\varepsilon = 0.622$. Given these inputs, the surface pressure P_s is calculated from the hydrostatic equation:

$$P_s = P_{ref} \exp \left[\frac{g}{R_d T_v} (H_{ref} - h) \right]$$

Equation 47

where $R_d = 287.04 \text{ J K}^{-1} \text{ kg}^{-1}$ is the gas constant for dry air and g is the gravity acceleration at elevation h_m .

Since the NWP data are available at finite spatial and temporal resolution, their values at the center of the CrIS footprint are obtained by linear interpolation in space and time. If the refresh period for NWP data is Δt_{nwp} and the CrIS measurement time t_m falls between NWP reporting

times t_{nwp_i} and $t_{nwp(i+1)}$ such that $t_m = t_{nwp_i} + p \Delta t_{nwp}$ (where $\Delta t_{nwp} = t_{nwp(i+1)} - t_{nwp_i}$ and $p \leq 1$), then the linear interpolation in time gives:

$$f(t_m) = (1-p)f_{nwp_i} + pf(t_{nwp_{i+1}})$$

Equation 48

where f is the required field (e.g., surface pressure or temperature). Similarly, horizontal interpolation in latitude and longitude utilizes the four NWP gridpoints surrounding the center of the footprint:

$$f(lat_m, lon_m) = (1-p)(1-q)f_{0,0} + p(1-q)f_{1,0} + q(1-p)f_{0,1} + pqf_{1,1}$$

Equation 49

where $lat_m = lat_o + p\Delta Lat_{nwp}$ and $lon_m = lon_o + q\Delta Lon_{nwp}$ are the latitude and longitude of the center of the footprint, lat_o and lon_o are the latitude and longitude of the nearest NWP gridpoint, and ΔLat_{nwp} and ΔLon_{nwp} are the resolution of the NWP data in the latitudinal and longitudinal direction, respectively. For virtual temperature, the vertical interpolation to elevation h_m is performed assuming that the gradients of temperature and humidity are constant within the NWP vertical layer containing h_m , i.e., $\partial T/\partial z = const$ and $\partial \ln q/\partial z = const$ within the layer. Alternatively, we could also assume that $\partial T_v/\partial z = const$.

During the interpolation of NWP data, several particular cases can occur:

- If during the satellite swath, the time of acquisition crosses the Δt_{nwp} period and the inputs have not been refreshed, the module will make an extrapolation for all times falling outside the range $[t_{nwp_i}, t_{nwp(i+1)}]$.
- For the horizontal interpolation, we have assumed that the footprint of the satellite is smaller than the NWP model grid size, i.e., $dlat_m \leq \Delta Lat_{nwp}$ and $dlon_m \leq \Delta Lon_{nwp}$. If this is not the case, then the NWP model resolution must be degraded to fit approximately the satellite footprint size.

A flowchart for surface pressure computation is shown in Figure 18. Figure 19 illustrates the geometry of the interpolation problem, with the numbers in parenthesis indicating the number of

gridded values (time, height, latitude, longitude) needed for the interpolation of a particular NWP field.

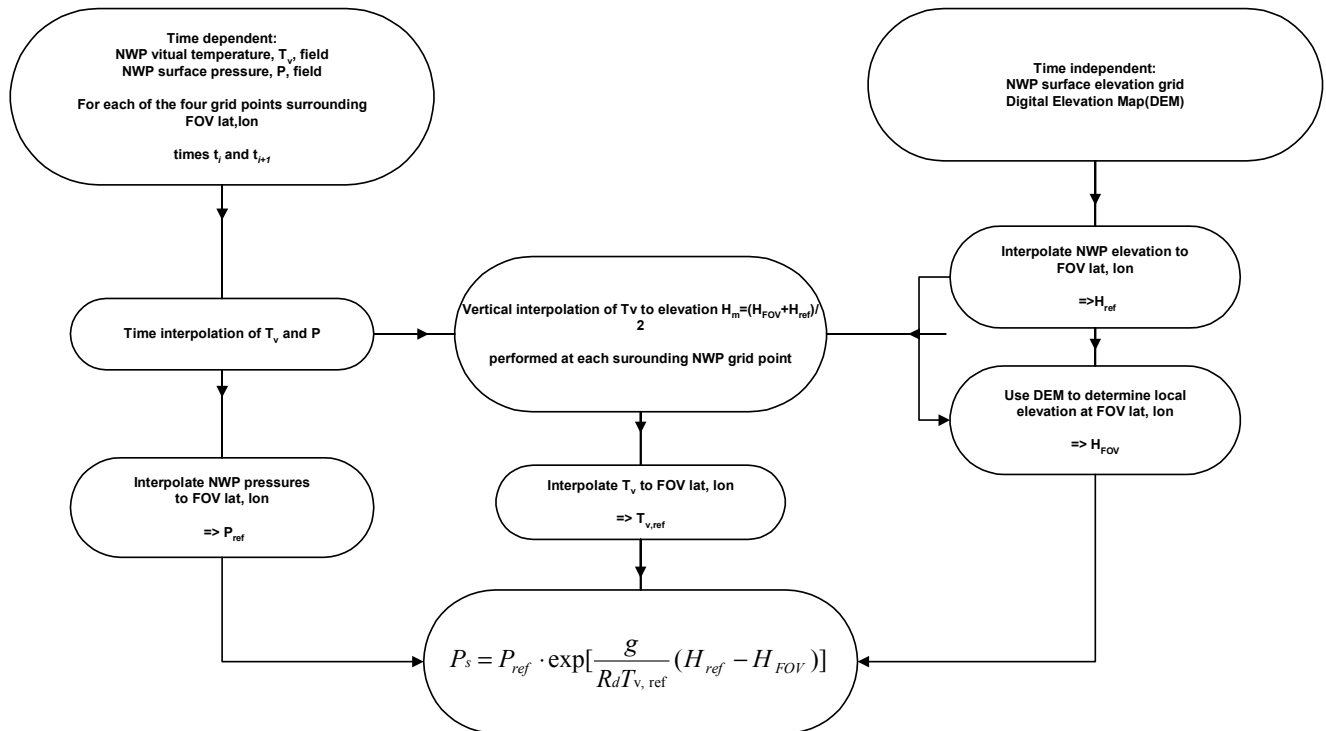


Figure 18: Flowchart for surface pressure calculation.

9.6.2 Possible Improvement

Instead of storing a high-resolution topography database containing height only, one could instead store the difference between the individual heights and the mean NWP height. The mean NWP topography would have to be processed off-line with the high-resolution topography. This will accelerate the processing of the hydrostatic equation. This will also reduce the number of inputs as we will not need the H_{ref} input anymore. The downside of this improvement is that the module will be less agile. Each time the NWP topography or the high-resolution topography are modified, the database will have to be processed again.

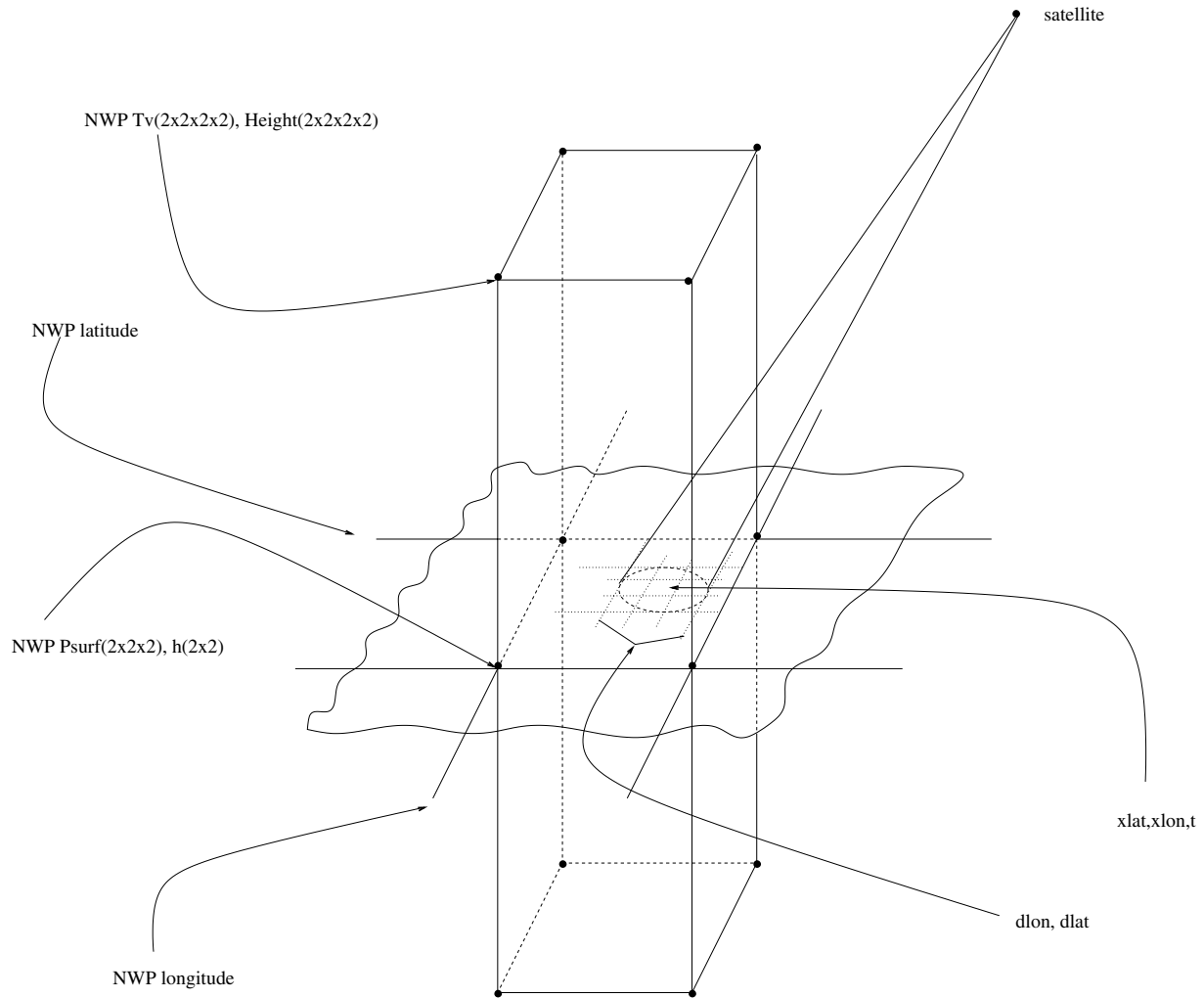


Figure 19: Illustration of configuration. Input from NWP: surface pressure, surface elevation, and temperature and water vapor profiles.

9.6.3 Example

The method of determining surface pressure described above has been applied to the Tibetan Plateau/India region, i.e., Lat: 0-35N, Lon: 65-95E at 0.1° resolution in latitude and longitude. The DEM points falling within 15-km sized regions corresponding to the size of CrIS footprints at nadir are included in the determination of average elevation. Figure 20a shows the footprint-averaged surface pressure field determined using the above technique, whereas Figure 20b shows the distribution of surface pressure P_{ref} interpolated to the center of each footprint from the NWP field. As can be seen, a straightforward interpolation of the NWP surface pressure captures the general shapes and boundaries of elevated terrain, but misses the localized variations.

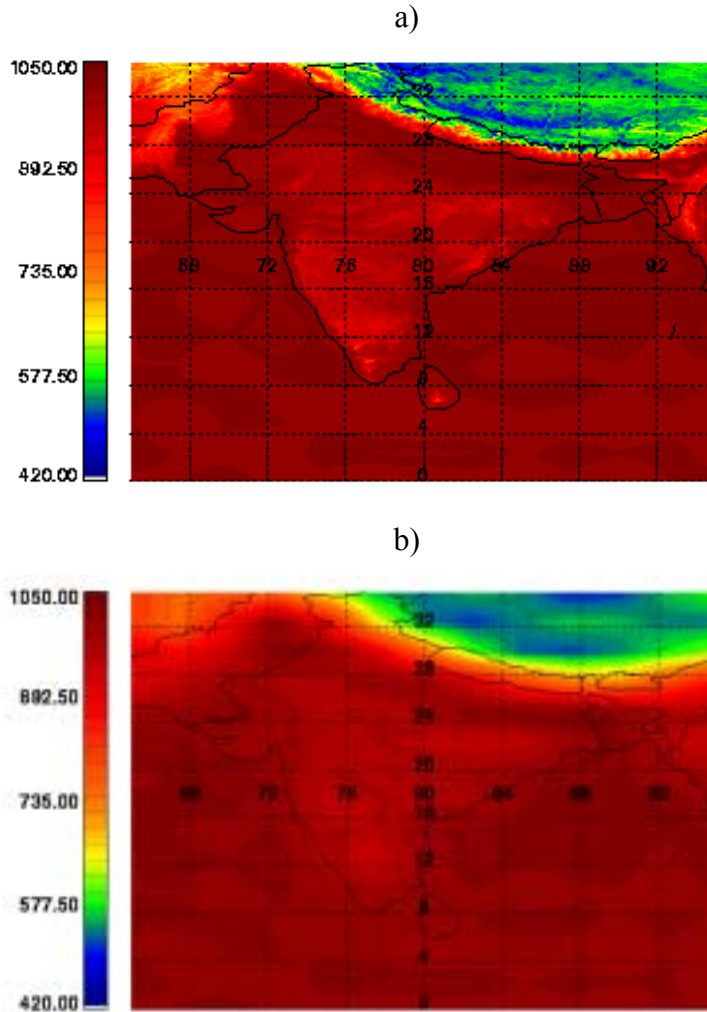


Figure 20: Surface pressure for the Tibetan Plateau/India region at 0.1° resolution (a) Calculated using the method described in this section (b) Obtained from a direct interpolation of NWP data.

9.6.4 Alternative Method

If the NWP-determined sea level pressure is available, the hydrostatic equation can be used with the average virtual temperature defined between sea level and the elevation h . Differences between the two methods are expected to be largest for high elevations. The benefit of this method is that reduces the computational time for each surface pressure calculation, as the process of determining T_v at h_m is eliminated.

9.7 NWP Initial Guess Profiles

If the microwave instruments fail, the first guess profiles for the infrared retrievals will be obtained from NWP fields using a time and space interpolation procedure similar to that employed in the surface pressure determination. Appropriate covariance matrices based upon NWP data will be used in the retrievals. Depending upon the source of NWP data, the number of pressure levels will vary. Typically there are more reported levels for temperature than for water vapor. These levels will have to be interpolated/extrapolated to the CrIS pressure level grid for input into the retrieval programs. A least-square method will be used to determine a regression matrix to map the NWP levels to the CrIS levels and extend the profile to 0.1 mb. In application, the mapping will indeed generate 40 temperature levels but only up to 100 mb for water vapor. To fill in the upper levels we apply the (pressure ratio)**3 drop off up to 100 mb and a constant value up to 0.1 mb. The regression matrix can be built from any data set that includes both the NWP and the CrIS levels.

10 MICROWAVE-ONLY RETRIEVAL

10.1 Description of the Algorithm

The functional flow diagram for microwave retrieval is shown in Figure 21.

The microwave retrieval algorithm uses radiances measured by the AMSU and MHS sensors and performs a physical inversion using a climatology background and the associated covariance as a constraint. A simultaneous retrieval of temperature, moisture, skin temperature, surface emissivity, cloud liquid water path, and cloud top pressure is accomplished using the AMSU and averaged MHS observations. For this step, the higher resolution MHS observations are averaged over the AMSU FOV (nine MHS FOVs per one AMSU FOV). A total of 20 microwave channel radiances are used in the inversion. Since the inversion process is highly non-linear in the presence of cloud, a modification to the maximum likelihood method has been applied (see Appendix 5). The iteration continues until the normalized χ^2_{MW} value of the difference between the measured and simulated radiances is less than 1 (see Appendix 5). The *a priori* information for the retrieval is described in Sections 8 and 9. It could be improved using a database of AMSU/MHS observations collocated with HIRS or AIRS retrieved temperature and moisture profiles. The maximum likelihood inversion also has the capability to incorporate additional external information, e.g., CMIS- or NWP-derived temperature and moisture profiles and surface parameters can be used to improve the background.

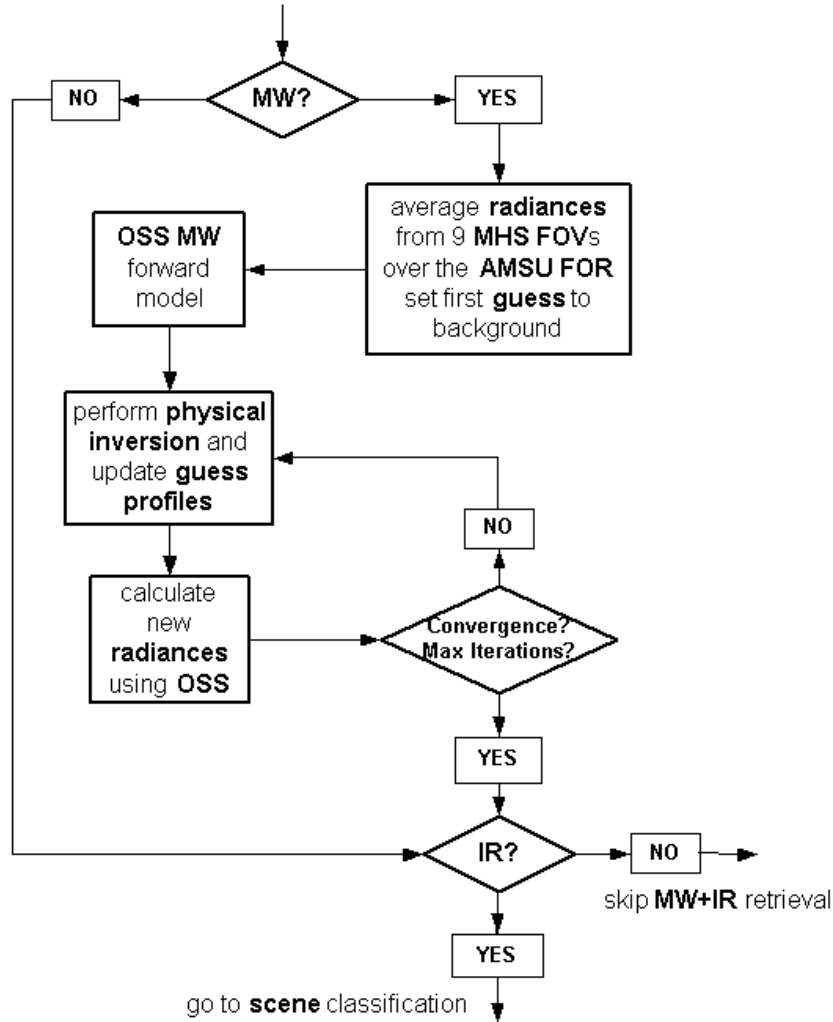


Figure 21: Functional Flow Diagram for MW Retrieval.

A normalized χ^2_{MW} is used to check the convergence of the retrieval.

$$\chi^2_{MW} = \sum_{i=1}^{nchanmw} \frac{(\Theta_i^{retr} - \Theta_i^{obser})^2}{N_i^{MW}} \bigg/ nchanmw$$

Equation 50

where $nchanmw$ is the number of microwave channels, Θ^{retr} is the retrieved brightness temperature, Θ^{obser} is the observed brightness temperature, and N_i^{MW} is the noise variance for the i -th MW channel. Currently the convergence criterion is for χ^2_{MW} to be less than 1.0 and the maximum number of iterations is set to 7.

10.2 Retrieved Parameters

The parameters retrieved in the microwave are listed in Table 13.

Table 13: List of Parameters Retrieved in the Microwave.

Parameter	# of elements
Temperature	20 EOFs
Water vapor	10 EOFs
Skin Temperature	1
Surface Emissivity	5 EOFs
Cloud Liquid Water	1
Cloud Top Pressure	1

In the current algorithm, the surface pressure is obtained from an NWP model output combined with knowledge of local topography (see Section 9.6). Uncertainties in surface pressure produced by current NWP models vary seasonally and are estimated at 2.5 mb globally (e.g., Devenyi and Schlatter 1994, Goerss and Phoebus 1993). These errors do not include errors in the interpolation performed as part of pre-processing. The errors can be much larger locally in instances of rapid cyclogenesis. Comparisons between mesoscale models and actual measurements performed in the context of North Atlantic Storm Experiment indicated errors as large as 13 mb.

Note that variable surface pressure causes some difficulties in the microwave, because the retrieval relies heavily on the natural correlation between surface skin temperature and surface air temperature. In order to avoid the additional complexity of having to modify background error covariance to accommodate variations in surface terrain height, the algorithm is set to retrieve T_{sfc} and $\Delta T = T_{skin} - T_{sfc}$ instead of T_{sfc} and T_{skin} . In this scheme the surface air temperature also drives the surface skin temperature and the correction term ΔT represents the departure of actual surface skin temperature from T_{sfc} . It should be noted that the retrieval is unaffected by this change of variables. However, because ΔT is statistically uncorrelated with T_{sfc} , the background and background error covariance matrix for ΔT remain independent of terrain height (i.e., the covariance need not be modified over elevated terrain).

The microwave algorithm is configured to retrieve surface emissivity in the EOF representation (currently, 5 EOFs are used). This approach captures correlation between different MW

channels. The emissivity retrieval is constrained using appropriate covariances described in Sections 8 and 9, with the matrices stabilized by the use of the EOF transformation.

The treatment of clouds in the microwave is described in Section 5.7.1. The two cloud parameters retrieved in the microwave are the total liquid water and the cloud top pressure, but trade studies have shown that when MHS is included with AMSU channels, cloud top temperature may also be necessary. Currently, clouds are modeled assuming a fixed thickness and a uniform vertical distribution of droplets within the cloud and variations in cloud effective temperature are accounted for by adjusting cloud top pressure. The algorithm considers Rayleigh absorption by cloud droplets and ignores scattering by ice crystals and precipitation size particles. The clouds are treated in the linear regime of absorption, e.g. it is assumed that the impact of the vertical and horizontal distribution of clouds is negligible. This may not hold for clouds with high density of water droplets near the cloud top and the impact of this assumption needs to be more fully assessed.

11 SCENE CLASSIFICATION

The purpose of the scene classification module is to maximize the number of reports in a FOR and to maximize the chances of a successful retrieval by adopting an appropriate strategy for the treatment of clouds. The choice of strategy for the selection of FOV clusters and of the retrieval method is dictated by the requirement to produce retrievals in partly cloudy situations when none of the FOVs within a FOR is clear. The HH strategy is not applicable in such conditions and the method of choice for dealing with clouds is the CC method. This approach has already been proven in operational environment and is currently considered a lower risk than the SCPR method. Consequently, the current scene classification module is geared toward the CC method.

A scene classification strategy depends on the instrument configuration and the number of FOVs per FOR and the current scheme is designed for a 3×3 FOV configuration. The flow diagram of the scene classification module is shown in Figure 22.

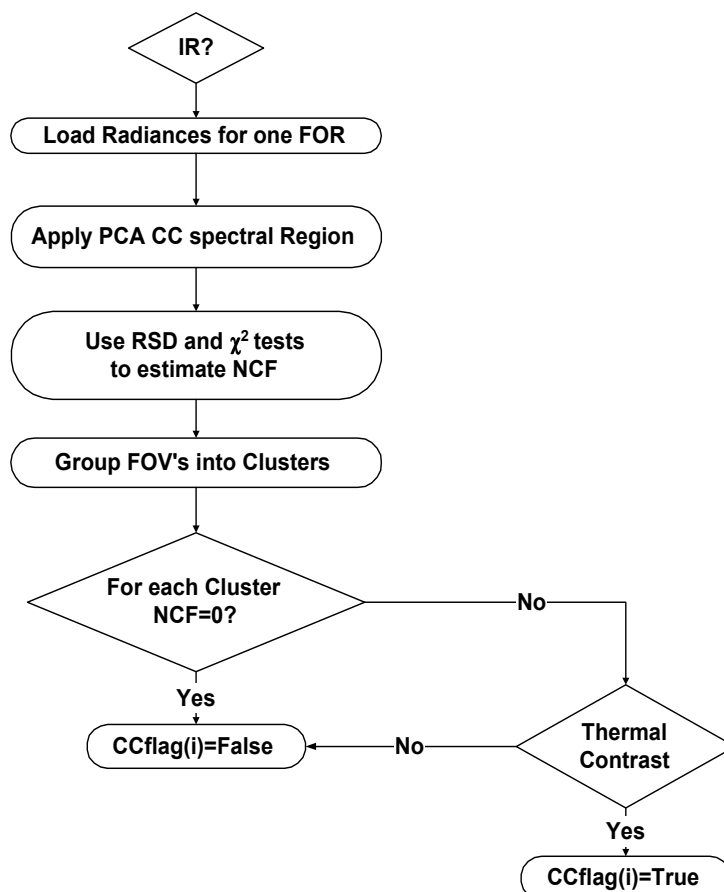


Figure 22: Flow Diagram of the Scene Classification Module.

Within one FOR, all 9 radiance spectra in the cloud clearing spectral region are used to form a data matrix. A Principal Component Analysis (PCA) is performed on this data matrix. In practical implementation, PCA is performed using a Singular Value Decomposition (SVD), with the eigenvalues equal to the square of singular values. At present, only the spectral region between 709 and 748 cm^{-1} is considered in this analysis. PCA expands the data matrix into 9 orthonormal principal components. These principal components can be classified into two classes. Those with large eigenvalues are called significant principal components, which are associated with cloud signatures. The remaining components are associated with measurement noise.

The number of FOVs needed to perform successful cloud clearing within a FOR depends on the number N_{CF} of cloud formations present in the scene. This number is determined from the PCA analysis using statistical tests described below. The number of significant principal components characterizing the scene, N_{CP} ($= N_{CF} + 1$) is usually associated with eigenvectors with the large eigenvalues.

Two threshold tests are currently considered for determining the appropriate number of cloud formations. The first test determines N_{CF} as the smallest value of n for which the Residual Standard Deviation (RSD), defined as:

$$RSD = \left(\frac{\sum_{j=n+1}^{n_{fov}} \lambda_j}{nchan * (n_{fov} - n)} \right)^{1/2}$$

Equation 51

where $nchan$ represents the total number of channels in the CC region, is smaller than the estimated measurement noise. The second test relies on the evaluation of χ_n^2 defined as:

$$\chi_n^2 = \sum_{i=1}^{nchan} \sum_{k=1}^{n_{fov}} \frac{[R_{ik} - \hat{R}_{ik}(n)]^2}{\sigma_{ik}^2} \langle (nchan - n)(n_{fov} - n) \rangle$$

Equation 52

where R_{ik} is the measured radiance in FOV k and channel i , $\hat{R}_{ik}(n)$ is the radiance reconstructed using the first n components, and σ_{ik} is the noise standard deviation associated with R_{ik} .

Figure 23 shows an example of Principal Components derived from simulated CrIS radiances for a FOR with 2 cloud layers with cloud tops at 300 and 400 mb and randomly assigned cloud fractions for each FOV. The associated eigenvalues, λ_n ; $n=1, \dots, N_{FOV}$ ($=9$), are shown in Figure 24. The first component, which is associated with the largest eigenvalue, represents the average radiance spectrum for the 9 FOVs. It is apparent in Figure 24 that the magnitude of λ_n decreases rapidly as n increases. The higher order components display significant random structure that is associated with the effect of instrumental noise. It is clear from Figure 24 that the first three principal components explain most of the variability of the scene. This is consistent with the fact that the radiances in each FOV are computed as a linear combination of one clear radiance and two cloudy radiances. The RSD and Chi-squares tests described above confirm that the number of cloud formation for this example is 2.

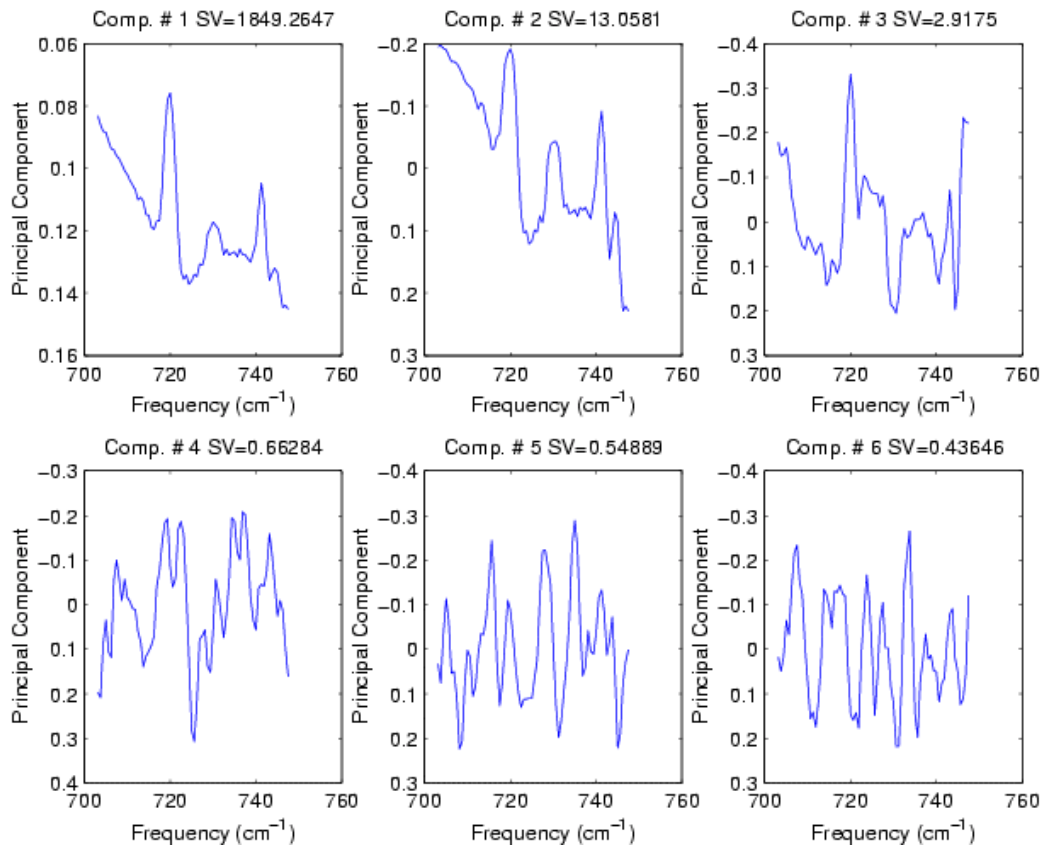


Figure 23: The first 6 EOFs resulting from PCA.

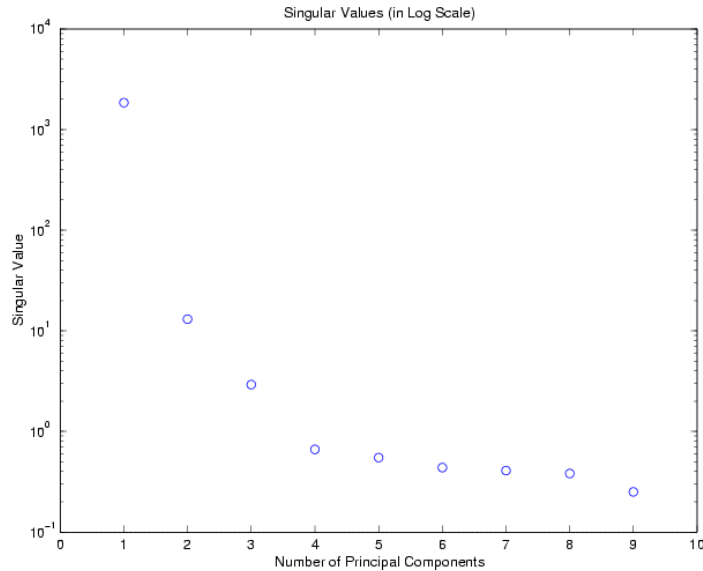


Figure 24: Magnitudes of singular values (equal to the square root of eigenvalues λ).

After N_{CF} is determined, the next step consists of grouping adjacent FOVs in sets of $N_{CF}+1$ to which the CC retrieval will be applied. Several clustering schemes are currently under consideration. One scheme uses the “adjacency” constraint, i.e., only neighboring FOVs are grouped to form a cluster (this constraint is imposed to mitigate risks associated with the assumption of homogeneous atmospheric and surface conditions within the cluster). The clustering pattern for $N_{CF} = 1$ in this scheme are shown in Figure 25. The central FOV is joined with neighboring FOVs to form clusters of 2 FOVs.

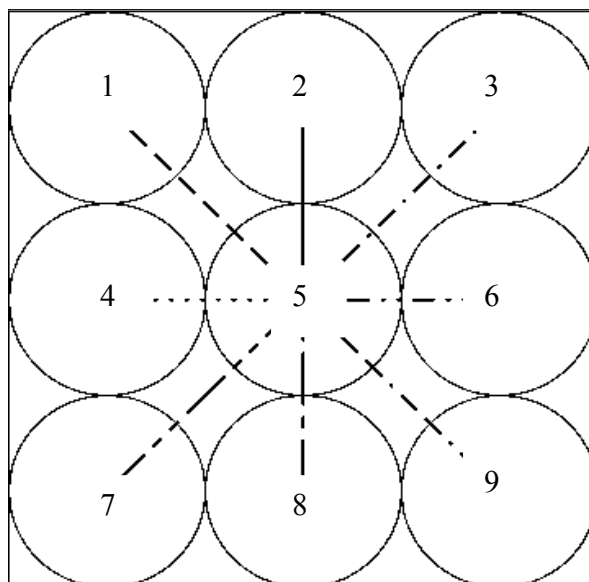


Figure 25: Clustering Pattern for 1 cloud formation.

This scheme, which uses fixed geometric patterns to group FOVs, does not take into account the thermal contrast between FOVs which needs to be sufficiently large for the CC algorithm to work properly. The occurrence of clusters that contain only clear FOVs is addressed by examining the radiance contrast between the FOVs in each selected cluster. When the maximum contrast is below a threshold, the radiances within the cluster are averaged and a single clear retrieval is performed on the resulting mean radiance. As discussed earlier, a small radiance contrast may be indicative of a totally overcast scene, high thin clouds, or low clouds. These conditions are addressed as part of the post-retrieval quality control (see Section 13). In order to increase the chances of success in such conditions, a subsequent retrieval should ideally be performed using the SCPR method (not implemented in the current code), which is more robust in the presence of clouds.

An example of the application of the PCA to estimate the number of cloud formations is shown in Figure 26. In this figure, the number of cloud formations is estimated for 16 scanlines, each with 30 FORs and 9 FOVs per FOV (see Section 13.5 for more information about the scanlines). In each FOV, 1 or 2 cloud formations have been defined by their average cloud top pressure and cloud fraction. (e. g., when the average cloud fraction for cloud 1 in the scene is zero, the true number of cloud formations is equal to 1). The PCA has been performed on radiances generated for these scenes. As can be seen, the estimated number of cloud formations is always less than 3 and in most cases it matches the number of true cloud formations. In cases where the estimated number of cloud formations is less than the true number, this indicates that either there is just one cloud formation or the two cloud formations are radiatively indistinguishable (within NedN) from each other. On the other hand, an overestimate of the number of cloud formations causes no problem for the CC algorithm; in fact it may lead to better temperature retrievals due to FOV averaging. One cause of the overestimation is the inhomogeneity in the scene for a particular FOR (such as coastline).

SECTION 11: SCENE CLASSIFICATION

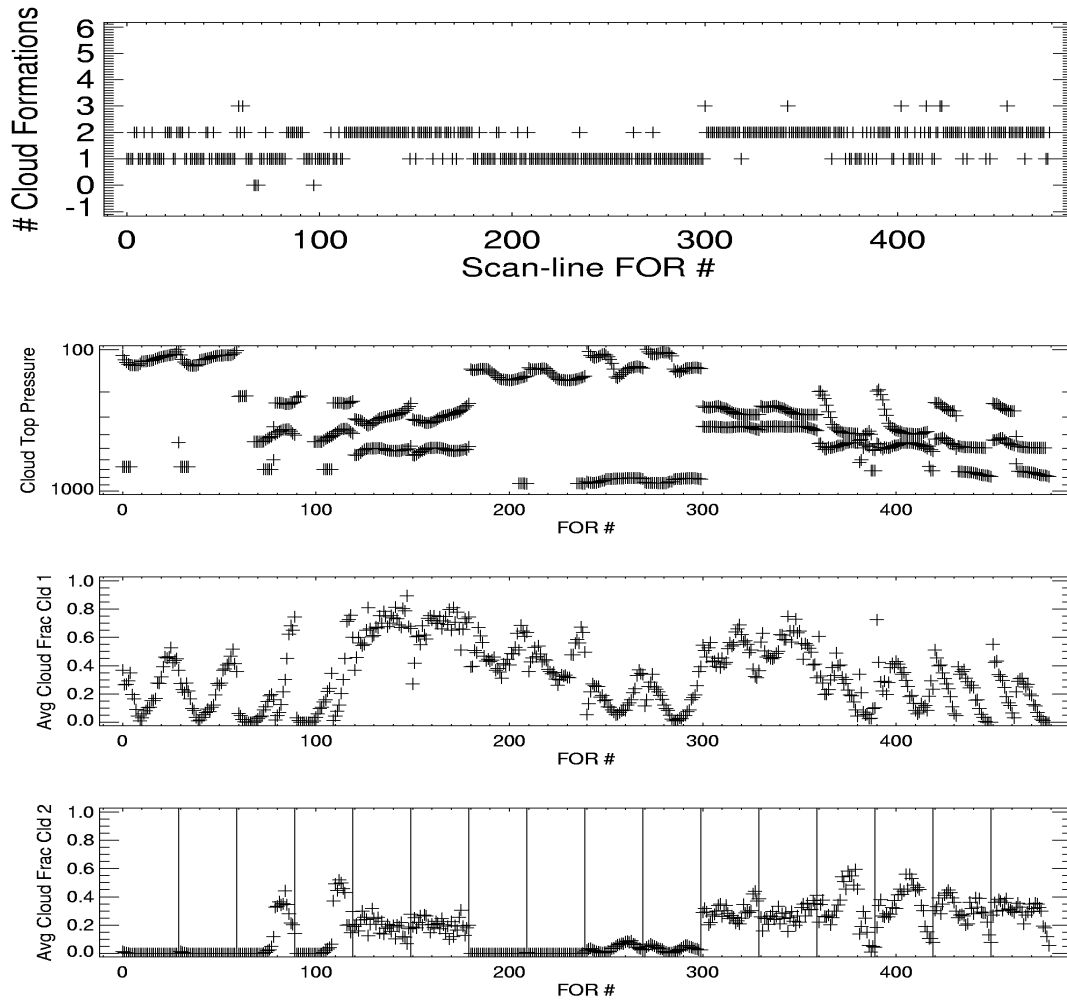


Figure 26: Application of PCA to estimate the number of cloud formations. (a) Number of estimated cloud formations. (b) Cloud top pressure of the clouds. (c) Cloud fraction of cloud 1 (d) Cloud fraction of cloud 2.

12 JOINT MICROWAVE AND INFRARED RETRIEVAL

12.1 General Description of the Algorithm

The joint microwave and infrared retrieval begins with the FOV selection within a FOR as described in Section 11. The results of the selection determine the appropriate cloud treatment strategy for this FOR and the retrieval could proceed using either the Cloud Clearing (CC) or the Simultaneous Cloud Parameter Retrieval/Hole Hunting (SCPR/HH) algorithm. This approach would maximize the chances of successful retrievals under cloudy conditions. In the current version of the algorithm, only the CC method has been implemented, but the code can be extended to include HH/SCPR. The CC algorithm is computationally more efficient than the SCPR algorithm and is low risk because it does not require an explicit treatment of clouds.

As in the microwave-only retrieval, the physical inversion at this stage is based on the modified maximum likelihood method, with the EOF representation used for reducing dimension of retrieved state vector and accelerating the inversion process. Channel weights are dynamically adjusted in order to take into account linearization errors and to further improve the convergence and execution time of the process. An optimization of the IR channel selection also improves execution time of the radiative transfer model and inversion (see Section 12.2 and Appendix 2).

The flow chart for the joint microwave and infrared retrieval is shown in Figure 27. The retrieval consists of the following steps:

1. Microwave-only retrieval provides first guess estimates of the temperature and moisture profiles and skin temperature, as well as estimates of surface emissivity and cloud parameters.
2. An estimate of clear infrared radiances R_{clr} is obtained using current temperature and moisture profiles. Cloud clearing is performed using R_{clr} and radiances from pre-selected FOVs (see Section 1). Spectral regions $709.5\text{--}746\text{ cm}^{-1}$ and $2190\text{--}2250\text{ cm}^{-1}$ are used to estimate the cloud-clearing parameter η . Errors due to uncertainties in temperature/moisture profiles and surface properties are estimated using sensitivity functions and they tend to

decrease at each iteration. The cloud clearing parameter η is used to calculate cloud-cleared radiances for all CrIS channels.

3. A physical retrieval is performed using the cloud-cleared CrIS radiances obtained from step 2 and the AMSU/MHS radiances. The temperature/moisture profiles, MW and IR emissivities, IR solar reflectivities, MW cloud parameters and surface skin temperature are retrieved simultaneously. Only one iteration is performed at this step.
4. Convergence test is performed using the χ^2 criterion. If the solution has converged or the maximum number of iterations is reached, the process stops. Otherwise, steps 2-4 are repeated.
5. Quality control is performed and EDRs are reported with appropriate quality flags.

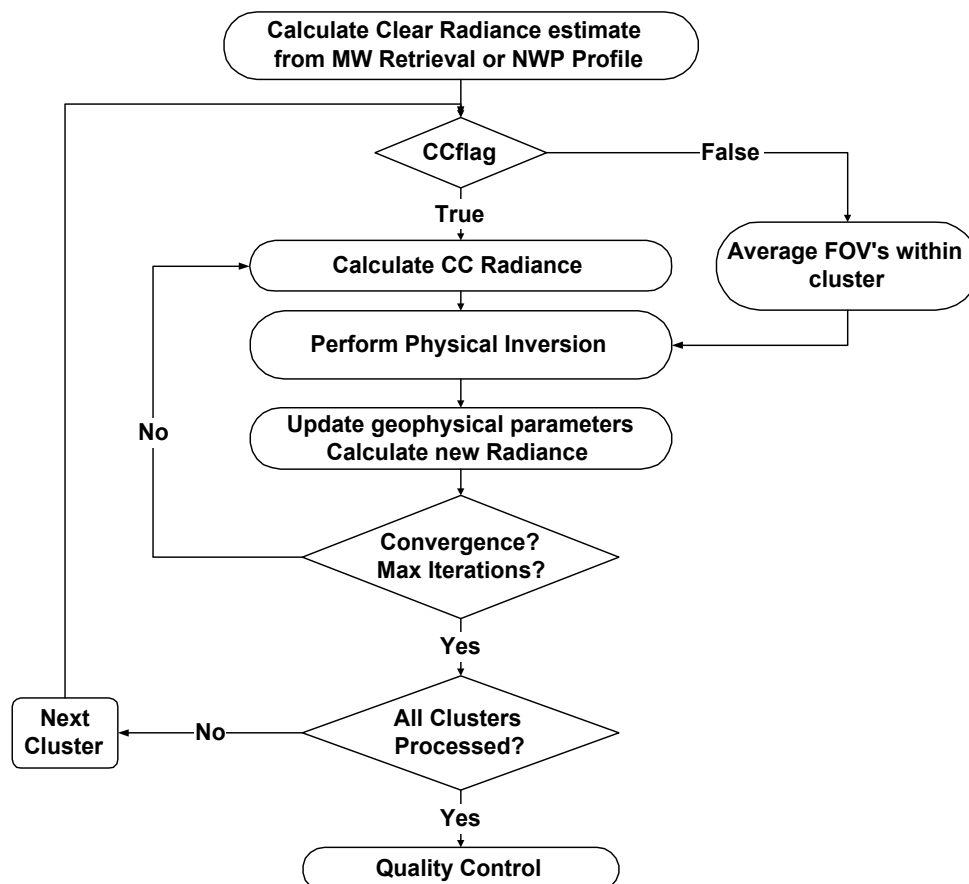


Figure 27: Flow Chart for the Joint Microwave and Infrared Retrieval.

The maximum number of iteration is currently set to 4. A normalized χ^2 is used to check the convergence of the retrieval:

$$\chi^2 = \sum_{i=1}^{nchan} \frac{(R_i^{retr} - R_i^{cc})^2}{N_i} \bigg/ nchan$$

Equation 53

where $nchan$ is the number of channels used in the retrieval, R^{retr} and R^{cc} are the retrieved and cloud-cleared radiances, respectively, and N_i is the noise variance for the i -th channel, which includes the noise amplification factor due to cloud clearing. Currently the convergence criteria are for χ^2 to be less than 0.7 and the relative change of χ^2 between the consecutive iterations to be less than 10%.

12.2 Channel Selection and Apodization

In the baseline algorithm, the retrieval is performed using all channels. However, the algorithm can also perform retrieval using only a subset of channels. While using all infrared channels maximizes the information contents of CrIS radiances, it requires significantly more computational resources than the method based on a subset of channels selected in order to satisfy the timing requirements discussed in Section 2.5. In fact, as described in Appendix 2, a subset of 300-400 channels can be selected to achieve significant time and memory savings with only a small degradation in the retrieval performance. The gain in computation between the two approaches is approximately a factor 3 (see Section 15). It should be emphasized that the benefits of channel selection are only significant when the ILS is spectrally localized. Channel selection does not improve the computational efficiency when the ILS is unapodized and a broad portion of the spectrum is needed to compute the radiance for a given channel.

When the spectra are apodized using either *Hamming* or *Blackman* window, the instrument noises are decreased at each channel but they become correlated between consecutive channels. In order to minimize the computational time spent in the inversion process, the inter-channel correlation is ignored in the error covariance matrix, resulting in a loss of information that degrades the retrieval slightly. Preliminary trade studies have shown that by keeping the diagonal

elements of the error covariance the same as the unapodized spectra, this degradation is can be minimized. This issue will be more fully investigated in the future.

12.3 Impact of Trace Gas Variability

The radiances measured by CrIS depend on the distribution of absorbing species, primarily H₂O, O₃, CO₂, N₂O, CO, and CH₄. In the baseline CrIS algorithm, only the variations in the vertical profiles of H₂O and column amounts of O₃ (relative to standard profile) are accounted for, with CO₂, N₂O, CO, and CH₄ treated as “fixed” gases for which standard distributions are assumed (e.g., 330 parts per million per volume for CO₂). However, trace gases exhibit large spatial and temporal variability caused by natural and anthropogenic sources. This variability needs to be accounted for in order to meet the accuracy requirements for CrIS EDRs. Preliminary results for ozone and nitrous oxide are presented in this section.

12.3.1 Ozone

A climatological database for ozone is contained within the NOAA-88 dataset. A set of these profiles has been used to simulate CrIS radiances and the retrieval has been performed on these radiances to assess the impact of ozone variability on the EDR performance. A nondimensional scaling factor equal to the ratio between the ozone column and the ozone column in the standard profile has been retrieved. During retrieval, the main ozone band near 1000 cm⁻¹ has been excluded.

For the limited set of NOAA-88 profiles, retrieving an O₃ column scaling factor appears adequate to minimize the impact of O₃ variability on the EDR retrievals under a variety of clear-sky and cloudy conditions. An example for a set of cloudy ocean scenes is shown in Figure 28. Future studies will show whether a column correction is adequate under more stressing conditions, e.g., those characteristic of a stratospheric ozone hole.

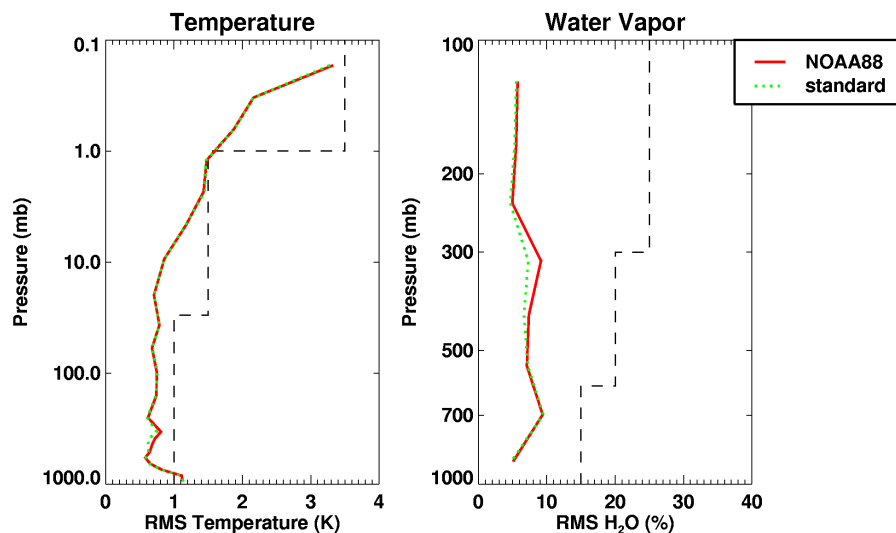


Figure 28: Impact of O_3 variability on temperature and moisture retrievals. Green lines: baseline algorithm (no O_3 variability), red lines: retrieval performed on simulated radiances including ozone profiles from the NOAA-88 database. In the retrieval, an O_3 column factor has been retrieved.

12.3.2 N_2O

The distributions of other trace gases are less well known than for ozone. The concentrations of N_2O are systematically measured only at five surface locations (Alaska, American Samoa, Hawaii, Colorado, and South Pole). These station measurements indicate little seasonal variability (less than 10 parts per billion per volume, ppbv, annually), but elevated concentrations of N_2O have been measured in polluted areas. Except during these pollution events, N_2O is rather well mixed in the troposphere (current mixing ratios are close to 320 ppmv) and falls off with height in the stratosphere due to a photolytical sink.

In the absence of global tropospheric measurements, the impact of variable N_2O on CrIS retrievals has been evaluated using profiles simulated by the Geophysical Fluid Dynamics Laboratory SKYHI general circulation model (Hamilton et al. 1995). Since the model simulates pre-industrial conditions, the global mean surface concentration of N_2O in the model is close to 260 ppbv. In order to simulate present conditions, the model profiles have been scaled by a factor of 320/260.

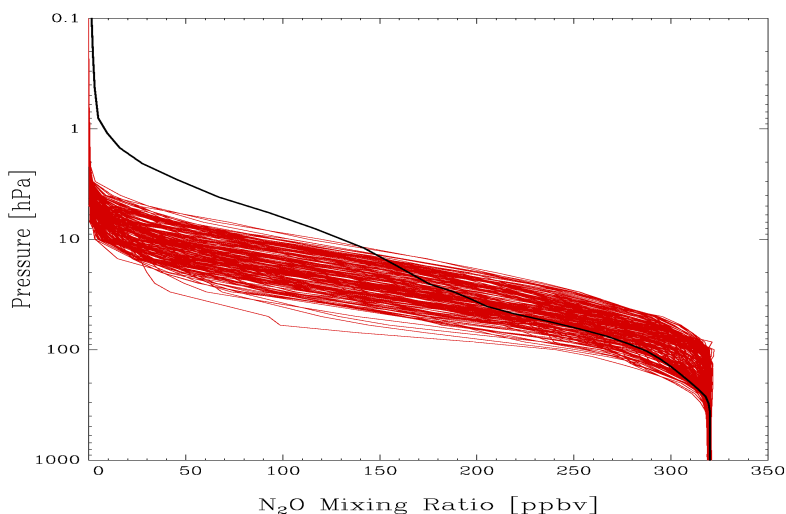


Figure 29: Simulated N_2O profiles from the SKYHI model (red lines). The black line represents the standard N_2O profile.

Figure 29 shows the N_2O profiles from the SKYHI simulation, together with the standard profile used to construct OSS optical depth tables. The model profiles show very little variability in the lower and middle troposphere and are unrepresentative of polluted conditions. However, as shown in Figure 30, the radiative effect of these idealized profiles exceeds the level of instrument noise in MWIR and SWIR and this can have a noticeable effect on the EDR retrievals.

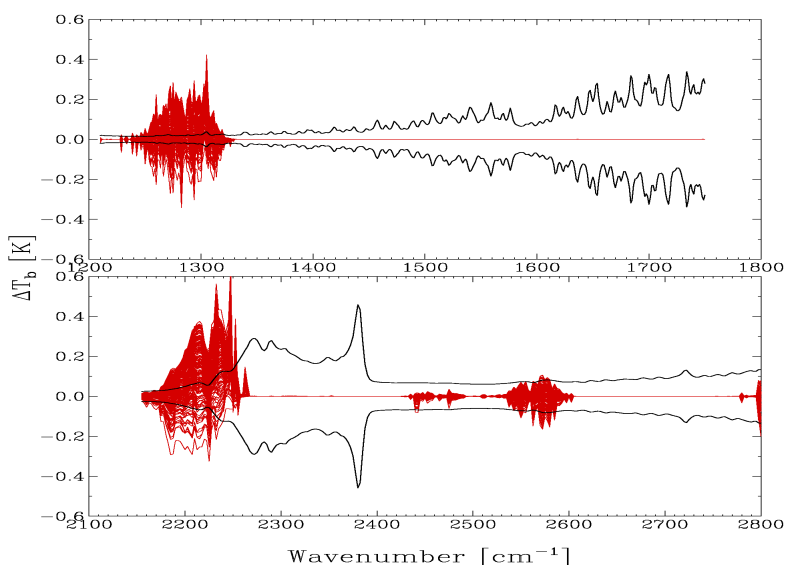


Figure 30: Radiative effect of variable N_2O . The red lines show the differences in brightness temperatures between radiances simulated using SKYHI N_2O profiles and the standard profile. Black lines represent CrIS instrument noise. Only results for the MWIR and SWIR bands are shown, as the impact of variable N_2O is minimal in LWIR.

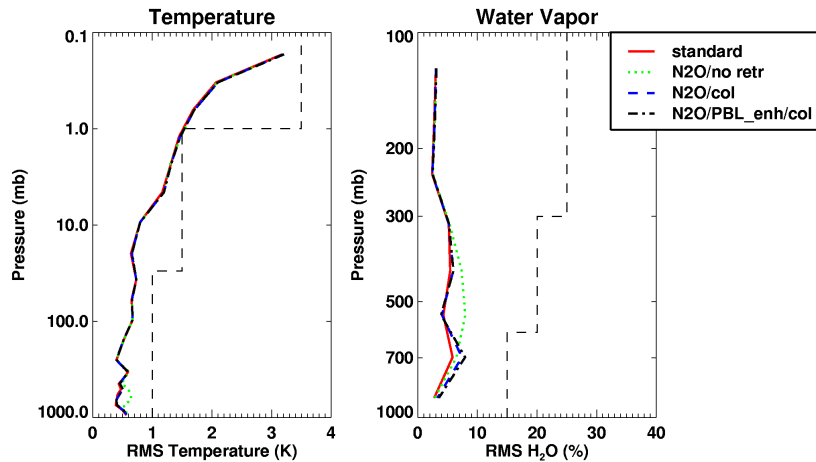


Figure 31: Impact of variable N_2O on the CrIS retrieval RMS error. Red: baseline algorithm (no N_2O variability), green: variable N_2O affecting radiances, ignored in the retrieval, blue: N_2O affecting radiances, retrieved as a column scaling factor, black: similar to blue, but N_2O enhanced by 50% between 1000 and 900 mbar.

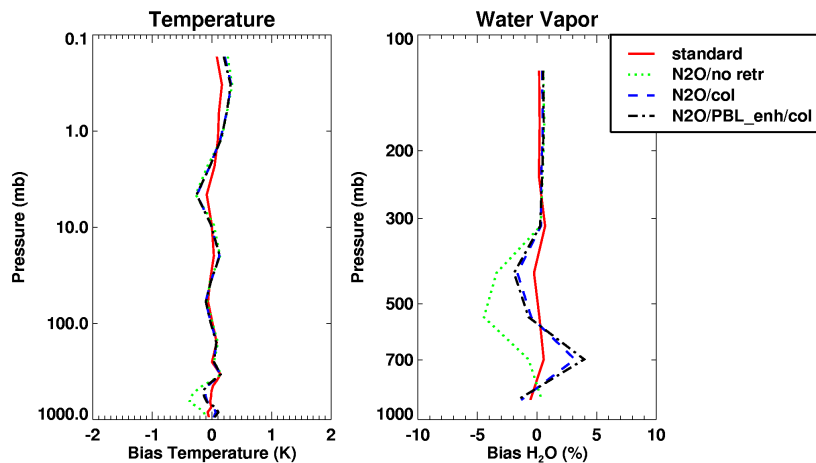


Figure 32: Similar to Figure 31, but for CrIS bias error.

Figure 31 illustrates the impact of variable N_2O on CrIS EDR retrievals under clear-sky conditions over ocean. Including variable N_2O in the radiance calculations, but ignoring it in the retrieval (green line) leads to EDR performance degradation (in the RMS sense) of more than 0.2 K for temperature and about 3% for moisture relative to the baseline algorithm (red line). The effect of ignoring variable N_2O appears even larger, especially for moisture retrievals, when the bias is considered (Figure 32). Retrieving an N_2O column scaling factor reduces the RMS error significantly, but it does not eliminate the bias. Similar results are obtained when the N_2O is enhanced by 50% near the surface in order to simulate polluted conditions.

12.4 Possible Strategy for IR Cloud Parameter Retrieval

The current version of the algorithm does not retrieve cloud properties in the infrared. However, the retrieval of infrared cloud parameters using SCPR will be assessed as a future technology insertion to provide cloud top and coverage as products used in NWP assimilation. Additionally, SCPR could be used to enhance the robustness of the EDR algorithm in cases where the HH method fails to correctly identify the presence of clouds.

A preliminary SCPR algorithm has been developed to retrieve cloud top altitude and effective cloud emissivity for single layer clouds in conjunction with other atmospheric EDRs. These cloud parameters are believed to adequately represent the radiative effects of clouds during nighttime in a wide range of conditions including different vertical distributions of cloud particles. In the scheme, the cloud radiative temperature is taken as the air temperature at the cloud top. Scattering is neglected, i.e., the clouds are assumed to be non-reflective and:

$$\epsilon_v^{cloud} = 1 - T_v^{cloud}$$

Equation 54

With this assumption, the following expression describes the radiance observed under cloudy conditions:

$$R_{cld} = \alpha \epsilon R_{clr} + (1 - \alpha \epsilon) R_{cld}^b$$

Equation 55

where α is the fractional cloud coverage within a FOV and R_{cld}^b is the radiance from a black cloud. This expression demonstrates that cloud fraction and emissivity play dual roles and are radiatively indistinguishable. In the context of OSS, it is computationally more efficient to compute directly R_{cld} for the entire mixed FOV than to perform two separate computations for the clear and cloudy columns. Therefore an effective emissivity that includes fractional cloud is defined as follows:

$$\epsilon_v^{cloud} = \alpha [1 - \exp(-k_v^{cloud} C)]$$

Equation 56

where C is the column density of cloud particles (cloud liquid water or ice water path), and k_v^{cloud} is the spectral absorption coefficient of the cloud particles which depends on effective size of cloud particles (size distribution), phase (ice/water) and shape of ice crystals. From a retrieval point of view, ϵ_v is represented by a set of 6 EOFs derived from a database of ϵ_v for an array of particle sizes with mixed ice/water phases and by randomly perturbing the elements of the above equation. It is possible that a database of ϵ_v can be derived from AERI, HIS, or NAST data.

The above SCPR scheme does not use radiances in SWIR. During daytime, SCPR is more difficult due to the scattering of solar radiation that depends not only on the bulk optical properties of the cloud but also on small-scale inhomogeneities within the cloud. Moreover, even during nighttime, difficulties in the modeling of ice crystal shape can be expected. In contrast to SWIR, these complications are minor in LWIR.

12.5 Retrieved Parameters

The parameters retrieved during the joint microwave and infrared retrieval are temperature and water vapor profiles and surface parameters, with the capability to retrieve the distributions of trace gases under investigation. The retrieved parameters are listed in Table 14.

Table 14: Parameters Retrieved in the Joint MW+IR Retrieval.

Parameter	# of elements
Temperature	20 EOFs
Water vapor	10 EOFs
Ozone	1 (column correction)*
Other trace gases	TBD
Skin Temperature	1**
MW Surface Emissivity	5 EOFs
MW Cloud Liquid Water	1
MW Cloud Top Pressure	1
IR Surface Emissivity	6 hinge points
IR Surface Reflectivity	6 hinge points

*In this mode, the 9.7- μ m band is not included.

** Currently a single skin temperature is retrieved for the microwave and IR bands.

Temperature and water vapor profiles are retrieved as the projection coefficients of the pre-determined EOFs. 20 EOFs for temperature profiles and 10 EOFs for water profiles are adequate

for representing the atmospheric variability and stabilize inversion algorithm. The correlation between the surface air temperature and surface skin temperature is removed from the climatology covariance matrix because of the high information content of the CrIS instrument.

The retrieved microwave cloud and surface emissivity parameters are the same as in the MW-only retrieval. The treatment of surface emissivity in the infrared is more complicated than in the microwave due to the hyperspectral nature of the measurement. The infrared surface emissivity can display complex spectral structure and depart significantly from unity in non-vegetated areas in the 10- and 3.7- μm windows. Estimates of this complexity can be determined based on the ASTER database (Advanced Spaceborne Thermal Emission Reflectance Radiometer, see <http://asterweb.jpl.nasa.gov> for more information). The ASTER emissivity database indicates that approximately one hinge point every 10 cm^{-1} is required in order to accurately represent the emissivity of rock formations and evaporation present in arid and semi-arid regions. Note, however, that the ASTER database relies on laboratory measurements, and significant smoothing may occur in nature due to mixing of materials within a FOV.

A good retrieval of surface emissivity is needed to maintain retrieval performance for lower troposphere temperature and water vapor. The cloud clearing algorithm also relies on a good retrieval in the presence of low clouds, since channels used for cloud clearing are sensitive to surface parameters. However, retrieval simulations have shown that *a priori* knowledge of the surface emissivity is not required for clear-sky retrievals. Currently, based on limited NOAA-88 database and AIRS simulated scanline scenes, six IR emissivity and solar reflectivity hinge points are retrieved (at 769, 909, 111, 2105, 2500, and 2857 cm^{-1}). It is anticipated that retrievals using real data will need a large number of hinge points in order to deal with highly variable surface emissivity in some areas of the land, even in the cloud clearing mode. As a future technology insertion, we intend to examine further this issue using data from airborne and future spaceborne sensors and assess the need for deriving surface emissivity characteristics on a regional basis to help improve the retrieval performance in non-vegetated areas. We also plan to use this information in support of dynamic channel selection in order to minimize number of retrieved hinge points.

13 QUALITY CONTROL

Assessing the quality of the retrieved atmospheric and surface parameters will be critical for the assimilation of these data into NWP models. We have identified three possible quality control tests that will estimate the accuracy, and hence the usability, of the retrievals. The tests determine the final output profile, either second stage MW and IR retrieval, first stage MW only retrieval or background. For instance, if the retrieval using only microwave SDR provided an accurate product and the combined microwave and infrared SDR retrieval appeared inaccurate, the microwave retrieval would be the final output. A quality control flag is also returned to indicate which profile is reported.

13.1 Normalized χ^2 Test

This test is performed at the end of the joint MW+IR retrieval. The normalized χ^2 used in the test is defined in Equation 53 and if its value is larger than 1.0, the retrieval is not reported.

13.2 Deviation Between MW-Only and Joint MW+IR Retrievals

Since the retrieval is less sensitive to cloud in the MW compared with IR, the RMS of the retrieved temperature profiles between the MW-only retrieval and the joint MW+IR retrieval can be used to assess the quality of the retrievals. The quantity used in this test is defined as

$$\sigma = \sqrt{\frac{\sum_{i=1}^{nlev} (T_i(MW) - T_i(MW / IR))^2}{nlev}}$$

Equation 57

where the sum is over the lowest 3 km of the atmosphere, $nlev$ is the number of pressure levels in that region and T is the retrieved temperature at each pressure level. If σ is larger than 3.0 K, the retrieval is not reported. This test is only performed if the first stage MW retrieval passes the quality control test described below. It should also be noted that this test is only useful if the MW-only retrieval is close to the truth to start with. If this is not the case, the joint MW+IR retrieval that varies little from the MW-only retrieval, but is far away from the truth, will pass the

test. It is also possible that the joint retrieval makes significant improvement over the MW-only first guess, but is nevertheless rejected. Since the MW retrieval performs better over oceans, this test is more reliable for these environments.

13.3 MW Quality Control Test

If the MW radiances generated during the joint MW+IR retrieval are very different from the observed radiances, this indicates that there is cloud signature in the cloud-cleared radiances and the normalized χ^2_{MW} for the MW channels, defined in Equation 50, is large. In the current code, if χ^2_{MW} is larger than 3.0 K, the retrieval is rejected.

13.4 Quality Control Procedure Flow Diagram

Figure 33 represents an overview of the quality control procedure.

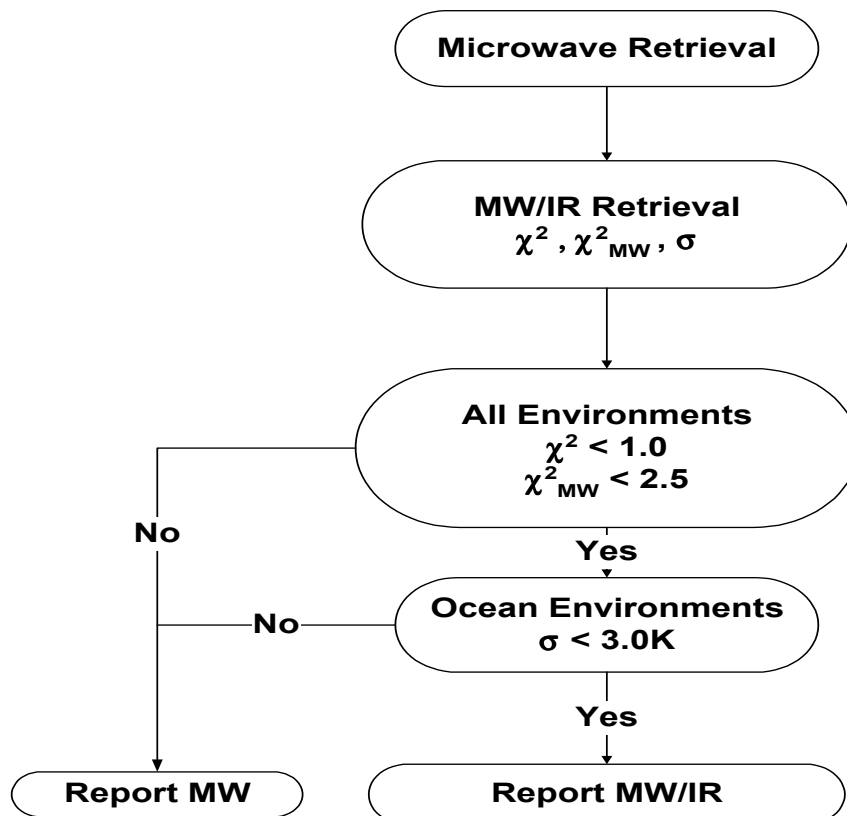


Figure 33: Quality Control Flow Diagram.

Some of the tests above have been ineffective in detecting erroneous retrievals for scenes with low level clouds in the FOR. Surface properties and atmospheric profiles can compensate for the cloud leading to a residual that is below the threshold.

Several other quality control methods are being investigated. For ocean scenes, the second stage MW and IR retrieved SST should have little variability for adjacent FORs across a single scan. Large differences in the retrieved SST for adjacent FORs could indicate errors in the cloud-cleared radiances. The cloud-clearing method is more effective for scenes with high clouds. Thus, a test on the variability of the retrieved SST could be used to detect low cloud.

13.5 Application of QC to Scanline Retrievals

The CrIS weather product testbed developed by the IPO consists of sets of profiles designed and grouped to represent the proposed CrIS and AMSU/MHS footprint configuration. The locations of the scan lines are shown in Figure 34. The set simulates CrIMSS scans, with sixteen scans sampled over the globe. Each scanline has 30 FORs and each FOR has 9 CrIS/MHS FOVs.

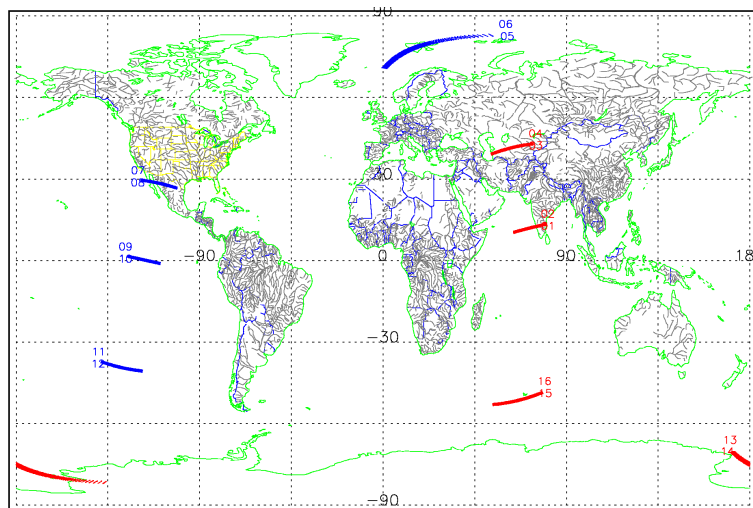


Figure 34: Location of scanlines.

There is a variety of cloud and surface conditions for each scanline. Figure 35 shows the average cloud top pressure, average cloud fraction, and maximum contrast within an FOR. These are the three most important factors affecting a successful application of the cloud-clearing method. The algorithm is least effective for low clouds and low contrast. Figure 36 shows the error in the

retrieved lower tropospheric temperature for each FOR (270 in all). A comparison of Figure 35 with Figure 36a reveals correlation between large cloud fraction, low contrast, low cloud top pressure and the goodness of the retrieval. In Figure 36b, the application of each QC test is illustrated. The first level below the zero line represents profiles rejected by the MW+IR χ^2 test, the second level are the profiles rejected by the MW-only χ^2_{MW} test, and the third level are profiles rejected by the RMS between the first and second stage temperature profile retrievals. There is much overlap between the second and third test, suggesting that one of them might be eliminated.

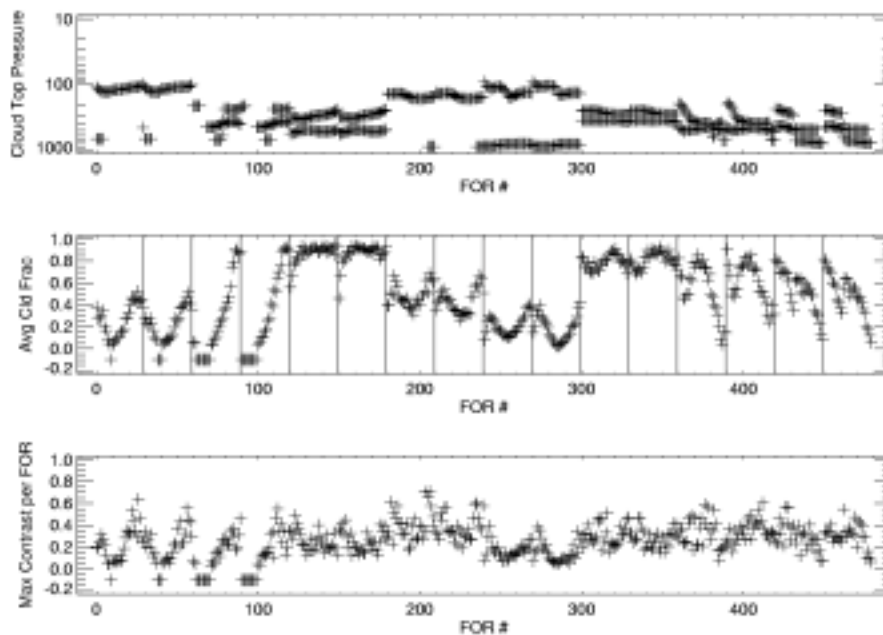


Figure 35: (a) Average cloud top pressure, (b) average cloud fraction, and (c) maximum cloud contrast for each FOR. The bars in (b) divide the 16 scanlines.

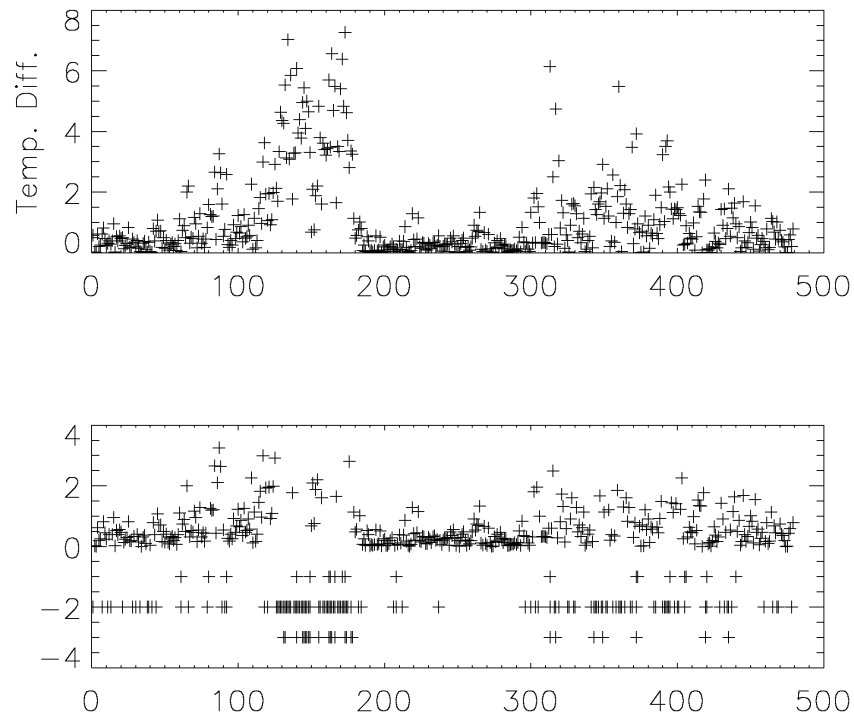


Figure 36: a) The absolute value of the difference in the average lower tropospheric temperature for each FOR. b) Same as (a) but with the rejection criterion applied.

To determine the thresholds for the various QC tests, the retrievals were ordered according to their error in lower tropospheric temperatures. The results are illustrated in Figure 37. All three tests diverge as the temperature error gets large, indicating that for the extreme cases each test will work and a more varied and extensive data set will be needed to finalize the thresholds. Figure 38 shows the RMS error for temperature and moisture retrievals with and without rejection. It should be pointed out that the variability of the profiles across each scan is small. Since the MW-only retrieval is little affected by clouds, the MW retrievals also vary little across a scan and the MW-only retrievals are fairly good for these scanlines. This is again an indication that more scanline type datasets will be needed to ensure that the QC thresholds are optimal.

SECTION 13: QUALITY CONTROL

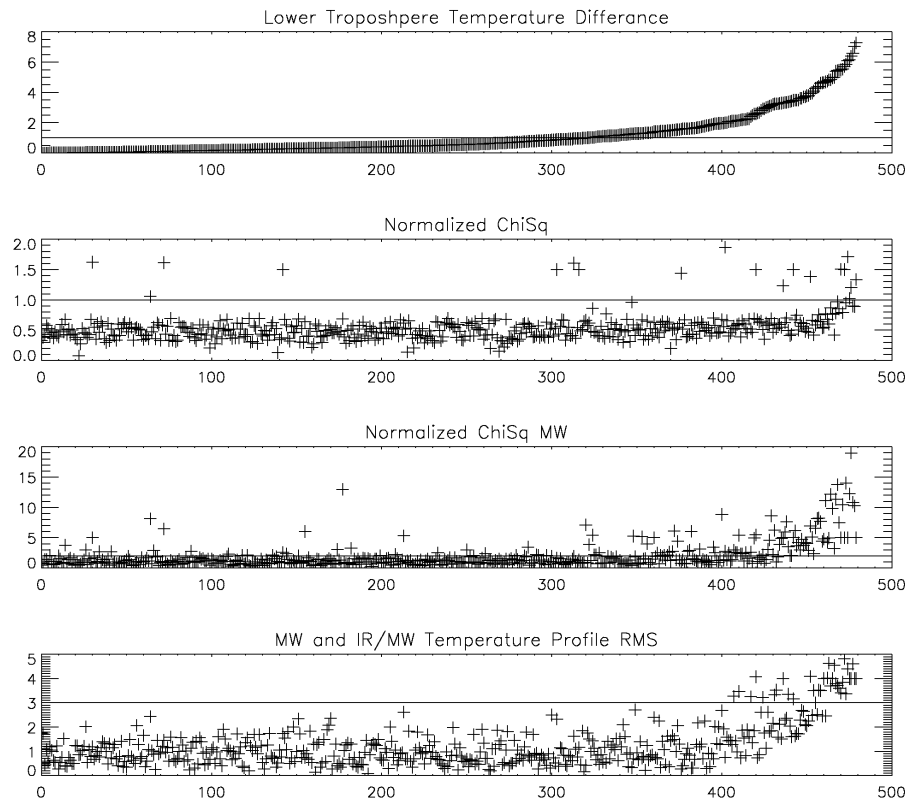


Figure 37: (a) Error in the lower tropospheric temperature for each FOR (sequenced from small to large), (b) χ^2 plotted in the same sequence as (a). (c) χ^2_{MW} plotted in the same sequence as (a), (d) σ plotted in the same sequence as (a).

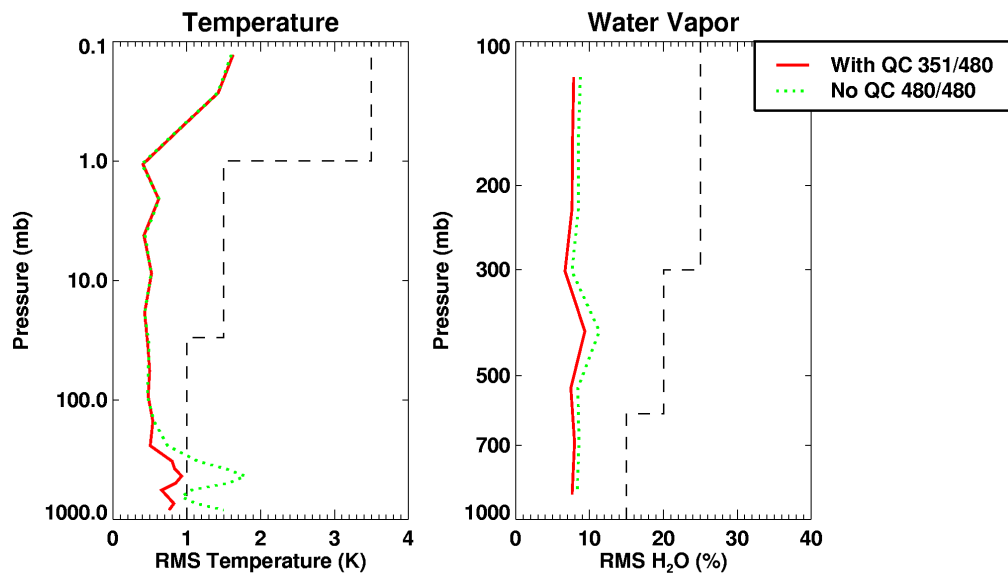


Figure 38: RMS error for temperature and moisture. Results with and without QC are presented. With QC implemented, 129 profiles out of 480 were rejected (27%).

13.6 Estimating Accuracy of Cloud-Cleared Radiances

Another approach to QC could involve a comparison cloud-cleared radiances and co-located VIIRS radiances in cloud-free regions. The minimum cloud optical depth specified for VIIRS is 0.03, which is close to the threshold that affects CrIMSS retrievals. If the difference between the cloud-cleared CrIMSS radiances and cloud-free VIIRS radiances is greater than 2 K, the retrieval may be biased.

14 OUTPUT AND POST-PROCESSING

14.1 Required Outputs

The primary EDRs for CrIMSS are the profiles of pressure, temperature, and moisture, with the pressure profile reported on an altitude grid and the temperature and moisture profiles reported on pressure grids. These reporting grids differ from the internal pressure grid used in the retrieval and RT calculations. The internal grid is determined through a trade-off between computational efficiency and numerical accuracy of the forward model. It currently uses 40 levels between 0.1 and 1000 mb, with the constraint that the last level is always located at the surface (consequently, the internal grid can contain less than 40 levels if the surface pressure is less 1000 mb). The internal pressure levels are defined in a slant sensor coordinate system, i.e., along the view angle of the sensor. In future, to comply with IPO requirements, the EDRs will be reported in a vertical coordinate system. The current choice of slant (rather than vertical) grid for reporting atmospheric profiles is driven by a desire to provide a product that is not degraded by post-processing. The output in this coordinate system can be expected to be representative of the vertical structure of the atmosphere, as long as the atmosphere is horizontally homogeneous or the scale of the desired features is greater than 20 km at edge of scan. The best approach for making use of the CrIS data in this context is to directly assimilate the product in the satellite coordinate. A complete set of auxiliary data output with the EDRs allows for the precise determination of the location of the temperature or water vapor product at any given pressure level.

14.2 Optional Outputs

Besides pressure, temperature, and moisture profiles, other outputs that are not required but are provided by the CrIMSS algorithm include ozone column amount, cloud top height, cloud fraction, and cloud emissivity (ice water path for thin cirrus clouds), and T_{skin} and surface emissivity.

14.3 Post-processing

This section describes the post-processing that is performed in the current version of the code.

14.3.1 Pressure Profile Computation

As mentioned above, the retrieval of temperature and moisture profiles is performed on a set of internal pressure levels. However, the EDR pressures are required at a set of reporting altitudes (every 1 km between 0 and 30 km) and they are calculated using the following procedure:

- Specific humidity σ and virtual temperature T_v are calculated for each retrieval level given temperature T and humidity q for the level

$$\sigma = \frac{q}{q+1}$$

$$T_v = (1 + 0.61\sigma)T$$

- Altitude is computed for each retrieval level using the hydrostatic equation

$$z_i = \sum_{j=2}^i \frac{R_d}{g} \frac{T_{vj} + T_{vj-1}}{2} \ln \left(\frac{p_{j-1}}{p_j} \right)$$

The above summation extends from the surface ($j=1$). p_j are the internal pressure levels (p_1 is the surface pressure), R_d is the gas constant for dry air, and g is the gravity acceleration (variations of g with geographical location and height are accounted for in the calculation).

- With surface pressure as the boundary term, the hydrostatic equation is integrated to obtain pressures at the reporting altitudes. The virtual temperatures at the reporting altitudes required for the integration are obtained by a linear interpolation in altitude from the virtual temperatures computed at the retrieval altitudes.

Figure 39 shows the results from 60 pressure profile calculations distributed globally with a surface pressure RMS error of 2.0 mb.

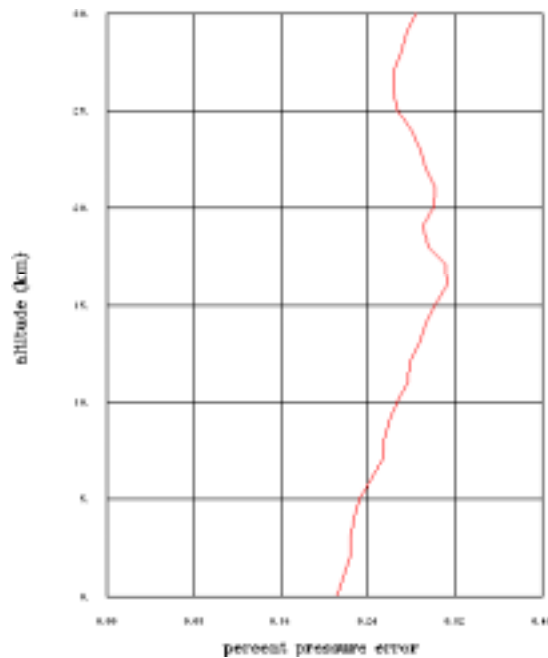


Figure 39: Pressure Profile Uncertainty.

14.3.2 Temperature and Water Vapor Profile Interpolation

In order to produce temperature and moisture profiles on the reporting grids, an interpolation from the internal grid (currently 40 levels) to the reporting grids is required. For temperature, the interpolation involves the assumption that the logarithm of temperature varies linearly with the logarithm of pressure. This assumption is rigorously valid if potential temperature is conserved (i.e., under isentropic conditions) and is equivalent to the assumption that temperature varies linearly with altitude if the difference between temperature and virtual temperature is neglected. This is consistent with the approach for calculating pressures at the reporting altitudes. For moisture, a linear interpolation of the mixing ratios is performed between the logarithm of the mixing ratio and the logarithm of the pressure.

14.3.3 Slant-to-Vertical Conversion

The CrIMSS EDR profiles are currently reported in the sensor slant path (the georeference is the intersection of FOV with surface). In order to conform with the CrIS reporting requirements, a slant-to-vertical conversion will be performed as part of post-processing in the final version of the algorithm. However, since CrIS measurements are not Nyquist-sampled and the retrieval product is provided on sparse grid (reporting interval varies with cloudiness), this conversion is likely to degrade the EDR performance. Among several possible approaches, a recursive filter method appears to offer the best combination of accuracy and speed (Hayden and Purser 1995).

14.3.4 Lower and Upper Air Temperature Profiling

As an option to enhance the EDR performance in the upper atmosphere, the CrIS lower atmosphere temperature profiles could be merged with upper atmosphere temperature profiles measured by CMIS. Since the CMIS scan geometry (conical with nominal 53° local incidence angle) is different from the one adopted for the CrIS (cross-track), a merging of CrIS and CMIS profiles would require a remapping of the profiles to a common scan geometry (this would result in some degradation of performance). Assuming that CMIS and CrIS retrieval products are on a common vertical grid, the CrIS and CMIS temperature retrievals could be merged using an optimal interpolation approach

$$T(p) = (S_l^{-1} + S_u^{-1})^{-1} [S_l^{-1} T_l(p) + S_u^{-1} T_u(p)]$$

Equation 58

where the subscripts l and u refer to the CrIS and CMIS profiles, respectively, and S_l and S_u are the corresponding error covariance matrices.

15 TIMING

Table 15 presents timing results for RT and derivatives calculations and a single MW+IR inversion performed on an SGI workstation with a single 195MHz RS10000 processor. Results for four cases are shown, including either the full CrIS spectrum or a subset of 305 channels and with the exponential expressions in the RT model either computed directly or approximated using a look-up table.

Table 15: Timing (in seconds) for the RT Model and the Joint MW+IR Retrieval.

	Full Channel Set with exponential	Full Channel SEt without exponential	305 Channels with exponential	305 Channels without exponential
OSS tran	0.063	0.064	0.024	0.024
OSS rad with derivatives	0.168	0.107	0.061	0.037
OSS rad without derivatives	0.138	---	0.056	---
Forward Model OSS total	0.236	0.175	0.089	0.066
Inversion	0.094	0.095	0.042	0.042
Total	0.362	0.296	0.144	0.118

The timing requirements allow for 20 minutes to process 1.25 orbits. The internal processing requirements are 18 minutes, which correspond to 38 ms per FOR. The current CrIMSS algorithm, running on an SGI workstation, is approximately 28 times slower than the requirement. This estimate was calculated using the values given in Table 15 and based on the assumptions that, on average, 3 MW/IR iterations are needed per report, and 3 reports are generated per FOR. It should be noted that the CrIMSS algorithm retrieves temperature and water vapor profiles simultaneously, rather than sequentially. A trade study has shown that this choice results in a 14-18% degradation in computational performance.

APPENDIX 1: SUPPLEMENTARY INFORMATION ABOUT THE OSS METHOD

This appendix contains supplementary information about the OSS forward model.

1 Monte Carlo Approach to the OSS Model

1.1 Introduction

The Monte Carlo approach to the OSS method is especially efficient for a non-localized ILS. This will be illustrated using the *Sinc* function as an example. The RMS error in the α -th channel can be written in the following form

$$RMS_{\alpha} = \sqrt{\frac{1}{N_s} \sum_{n=1}^{N_s} \left(\sum_i w_i^{(\alpha)} R_{n,v_i} - R_{n,c}^{(\alpha)} \right)^2}$$

Equation 59

Summation in n runs over N_s representative samples, i labels the selected points. $R_{n,c}^{(\alpha)}$ is used to denote the n -th component of the true radiance of the α -th channel. The RMS error is a key quantity defining the goodness of any search method, including the MC approach. Its application to the OSS model is schematically shown in Figure 40.

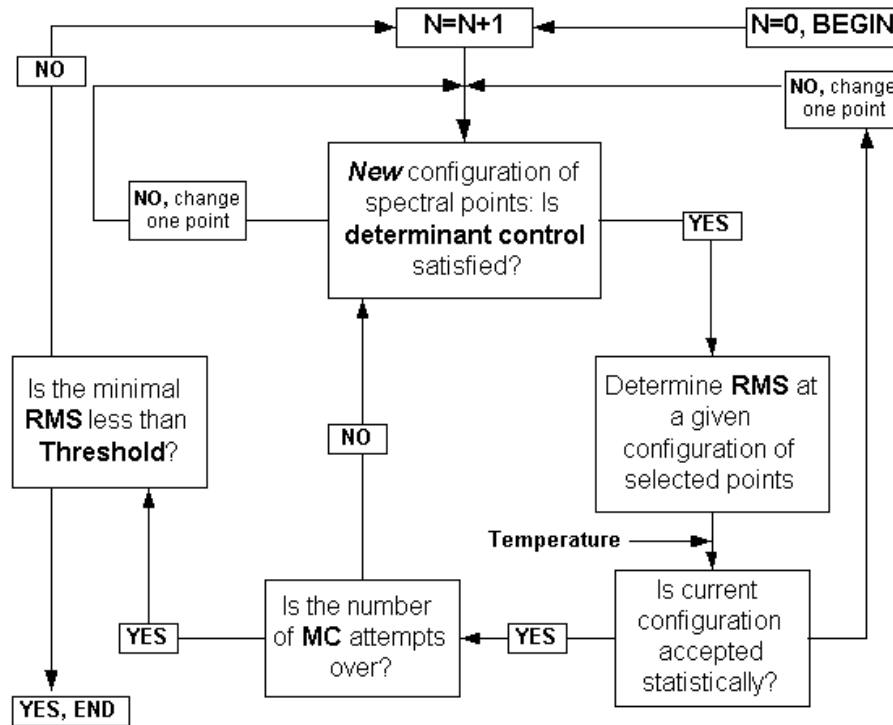
MONTE CARLO approach to the OSS model

Figure 40: Flow diagram for the MC approach to the OSS model.

Let us consider in a more detail how the MC search works with an ensemble of N selected points, and assign “slct” for their status. All other pre-selected points, which are confined to the channel region, get status “n/slct”. If the threshold condition is not satisfied with $(N - 1)$ “slct” points, a new, N -th, point chosen at random from the “n/slct” set will get the “slct” status. A new configuration should be checked whether the determinant control is satisfied (see below). If it is, then a statistical estimate should be done (see below under “Statistical Control”). The algorithm includes a pre-defined number of statistically accepted attempts. As long as this number is not exceeded, one point will be removed from the “slct” set and replaced by a point from the “n/slct” set, with both points selected at random. When the maximum number of MC attempts is reached, the RMS error is compared with the pre-defined threshold. If the former is smaller than the latter, the selection is finished. Otherwise, one proceeds to selecting the $(N + 1)$ -th point, etc. It should be noted that the MC approach provides a high degree of duplication, i.e., the same wavenumbers can be utilized for different channels. For *Blackman-3 π* , the number of duplicated points can reach ~25% of the total number of selected points, while for *Sinc* it can exceed 40%. This duplication can be used to improve the efficiency of the forward model.

The scheme shown in Figure 41 could be improved in cases when the set of selected points is overfilled, i.e., some of them could be removed from the selected ensemble without degrading the RMS error above the threshold. To eliminate these “overfilled” points, another selection among the selected points could be done. This would reduce the number of selected points for a given channel while keeping the RMS below the threshold. In contrast to the primary MC search, which may include a few thousand points for *Sinc*, this secondary search deals with a maximum of a few tens of points and could be performed using either the sequential or the MC approach. The fraction of points eliminated during the secondary search in all CrIS Bands is about 10% for *Sinc*, but for some channels with 20 or more selected points after the primary MC search, the number of eliminated points can reach 40%.

1.2 Determinant Control

Let us suppose that a total of N_C wavenumbers and corresponding monochromatic radiances have been selected. Because of the constraint

$$\sum_{i=1}^{N_C} w_i = 1$$

Equation 60

the RMS Error of Equation 59 can be rewritten as

$$RMS = \sqrt{\left(\sum_{i=1}^{N_C-1} w_i (\vec{R}_i - \vec{R}_0) - (\vec{R}_C - \vec{R}_0) \right)^2}$$

Equation 61

where \vec{R}_i , \vec{R}_0 and \vec{R}_C (vector of true radiance) are vectors in N_S -dimensional space. For example, the vector of radiance associated with the wavenumber ν_i is defined as:

$$\vec{R}_i = \frac{1}{\sqrt{N_S}} (R_{1,\nu_i}, R_{2,\nu_i}, R_{3,\nu_i}, \dots, R_{N_S,\nu_i})$$

Equation 62

The system of linear equations for the weights is $w_i L_{i,j} = M_j$, where summation over repeating indices is assumed. Here $M_j = (\vec{R}_C - \vec{R}_0) (\vec{R}_j - \vec{R}_0)$ is a $(N_C - 1)$ -component vector, whereas the matrix $L_{i,j} = (\vec{R}_i - \vec{R}_0) (\vec{R}_j - \vec{R}_0)$ defines the determinant $D = \det(L)$ used in determinant control. The geometrical interpretation of D is that it is equal to the square of volume of the N -dimensional parallelepiped in N_s -dimensional space built on vectors $\vec{R}_i - \vec{R}_0$, $i = 1, \dots, N$. Note that the location of wavenumbers and their weights do not depend on the choice of \vec{R}_0 , i.e., the role of \vec{R}_0 can be played by any radiance vector among the N_C candidates

The determinant control is implemented dynamically. The MC search begins with $N + 1$ points and a control that rejects configurations with determinant smaller than some $D(N)$. Rejected configurations are counted, and if the counter reaches a pre-defined number of accepted MC attempts, but the actual number of accepted MC attempts is below its limit, the determinant control is relaxed by multiplying $D(N)$ by some factor (0.1 in the current implementation). Simultaneously, the counter switches to zero. In addition, when the MC search with a new point begins, $D(N)$ may be further reduced (we used for such a reduction the factor of 0.1).

1.3 Statistical Control

Statistical control compares the current value of the RMS error with the value obtained for a preceding configuration of statistically accepted points. The comparison involves a parameter T called “temperature” (of course, this is not a physical, but fictitious temperature).

The value of T defines the probabilistic function:

$$P(RMS_{old}, RMS_{new}) = \frac{1}{1 + \exp(RMS_{new} - RMS_{old})/T}$$

Equation 63

For T much larger than a typical RMS value, $P \approx 1/2$, i.e., statistically accepted and rejected attempts are equally probable. This is a sort of random selection, which is poorly convergent. In the opposite “low-temperature” limit, accepted are only those configurations for which $RMS_{new} < RMS_{old}$ and a majority of attempts will return $P \approx 0$. In this case, the MC search could be replaced by Sequential Search, and this is in fact a reasonable choice for localized ILS functions. In general, something between these two limits is needed. In practice, if the numbers of rejected and accepted configurations differ by a factor of 2, the MC method shares the best features of sequential and random selections. It reveals the tendency to reduce the RMS error as in a deterministic sequential search method, and the ability to interrupt such a deterministic search in order to optimize it. There is no special equation to set a temperature, but it can be easily determined by a computational experiment. We set $T = RMS_{old}/3$. If the number of statistically rejected attempts reaches the doubled limit pre-defined for statistically accepted attempts, temperature grows by some factor (50% in our realization), which allows to get rid of slowing down. As in the case of the determinant control, the counter of statistically rejected attempts switches to zero in this situation.

2 Validation of the OSS Model

This section contains figures pertaining to the validation of the OSS model.

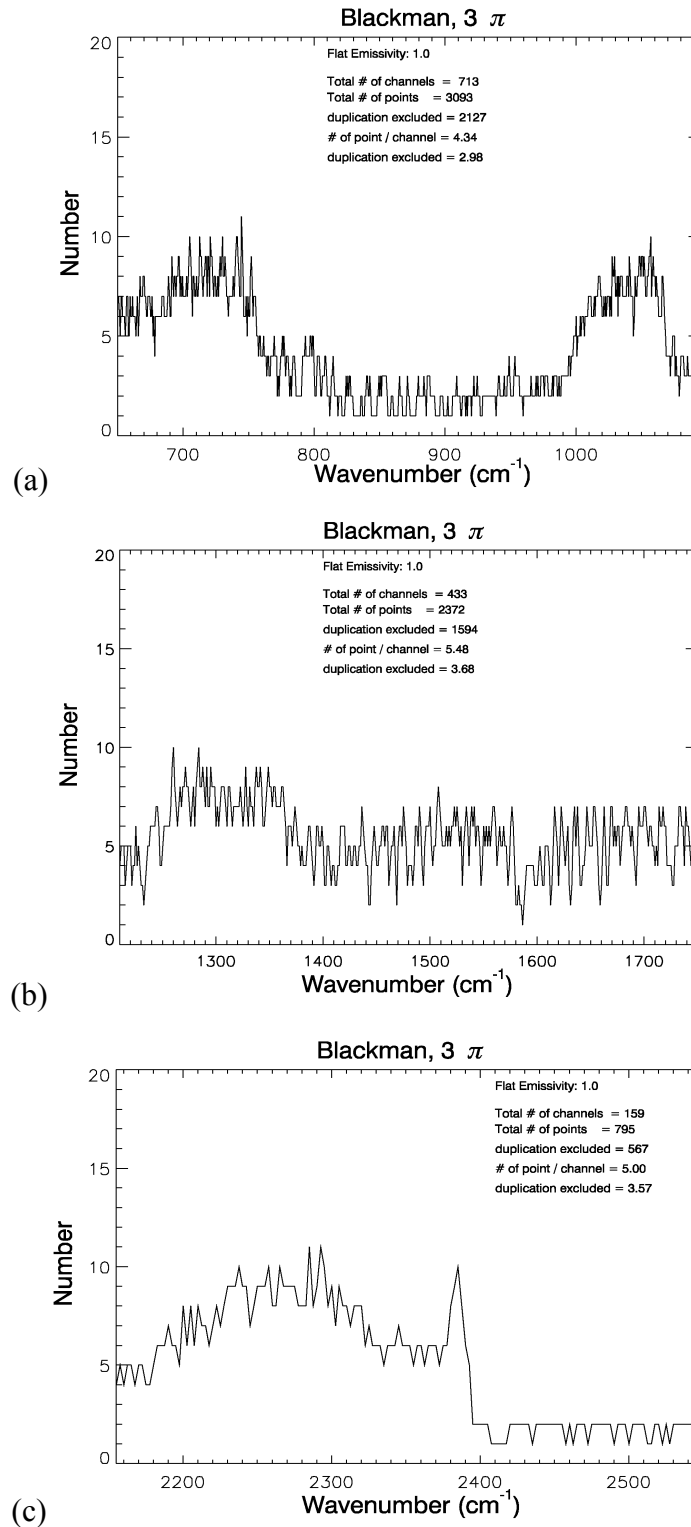
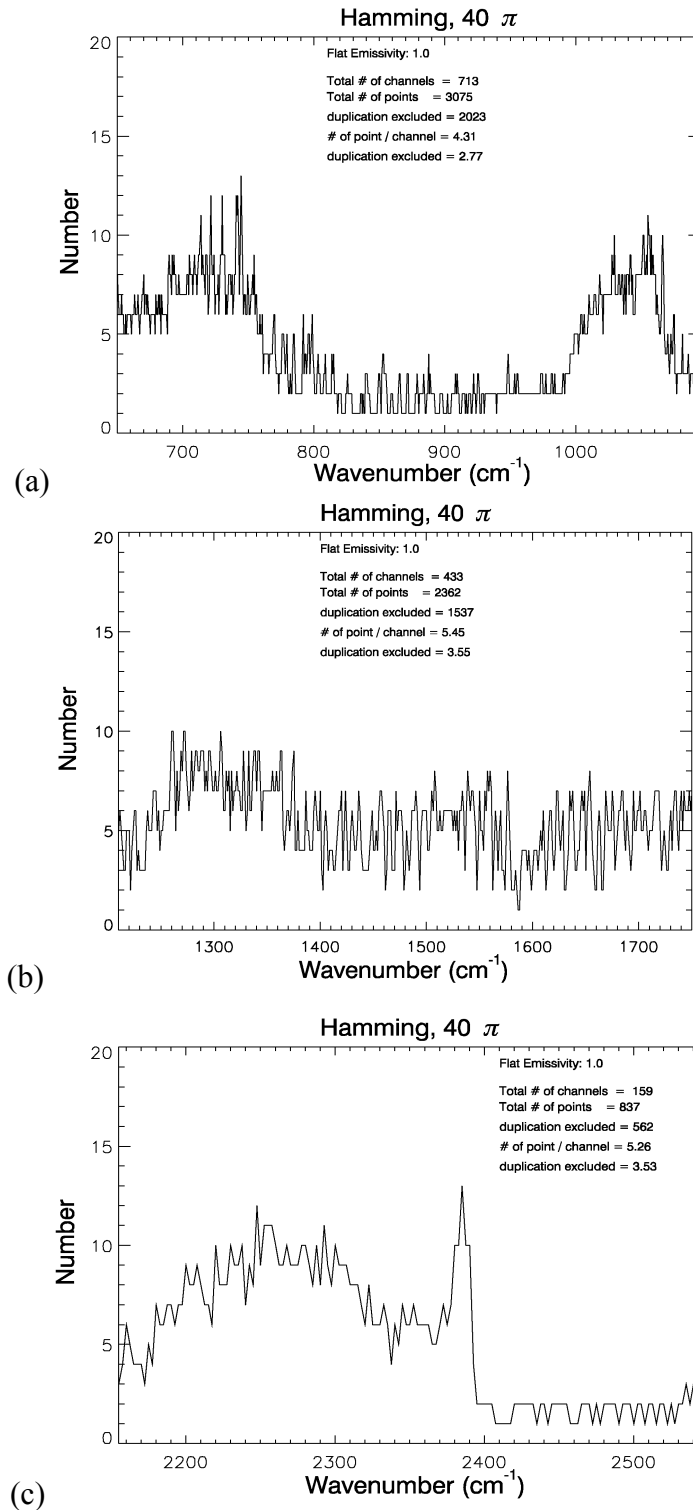


Figure 41: Number of spectral points selected for *Blackman* ILS with 3 side lobes. (a) LWIR, (b) MWIR, (c) SWIR.

Figure 42: Similar to Figure 41, but for *Hamming* ILS with 40 side lobes.

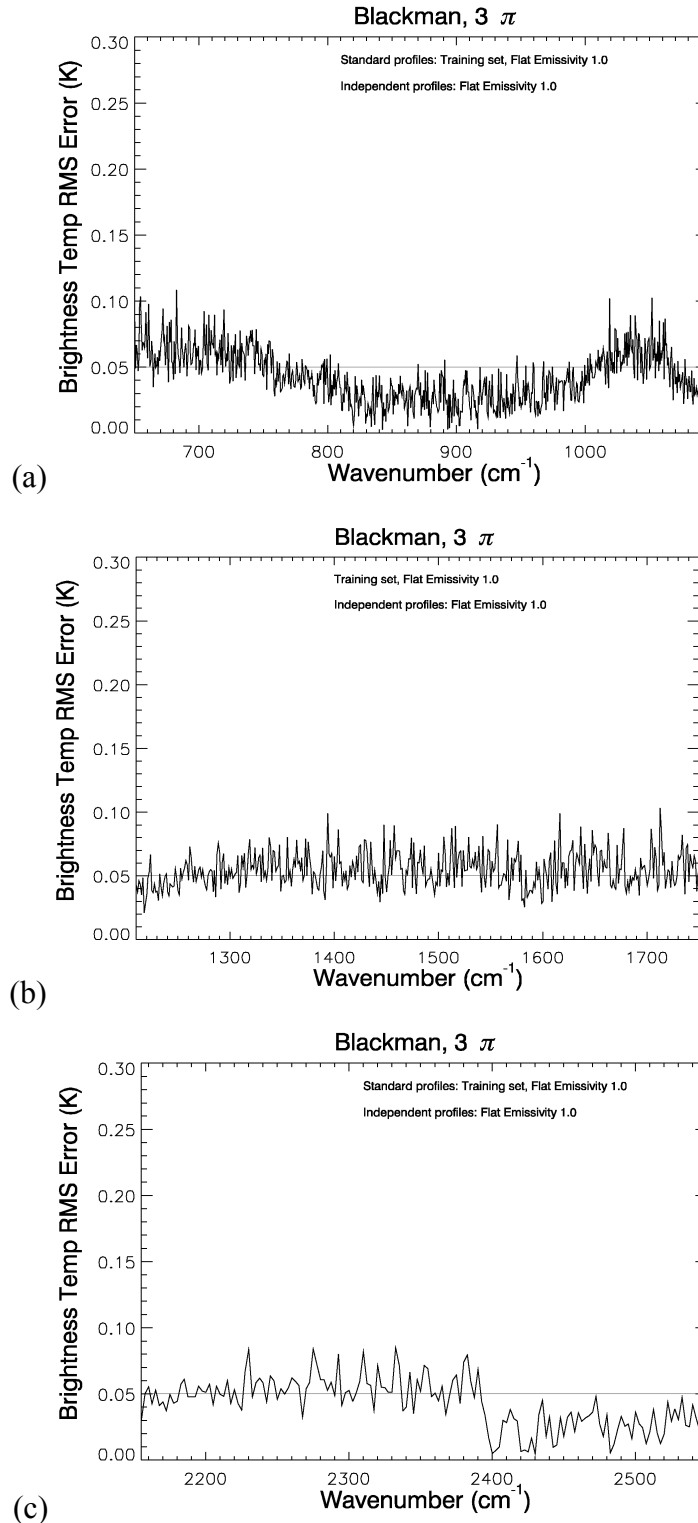
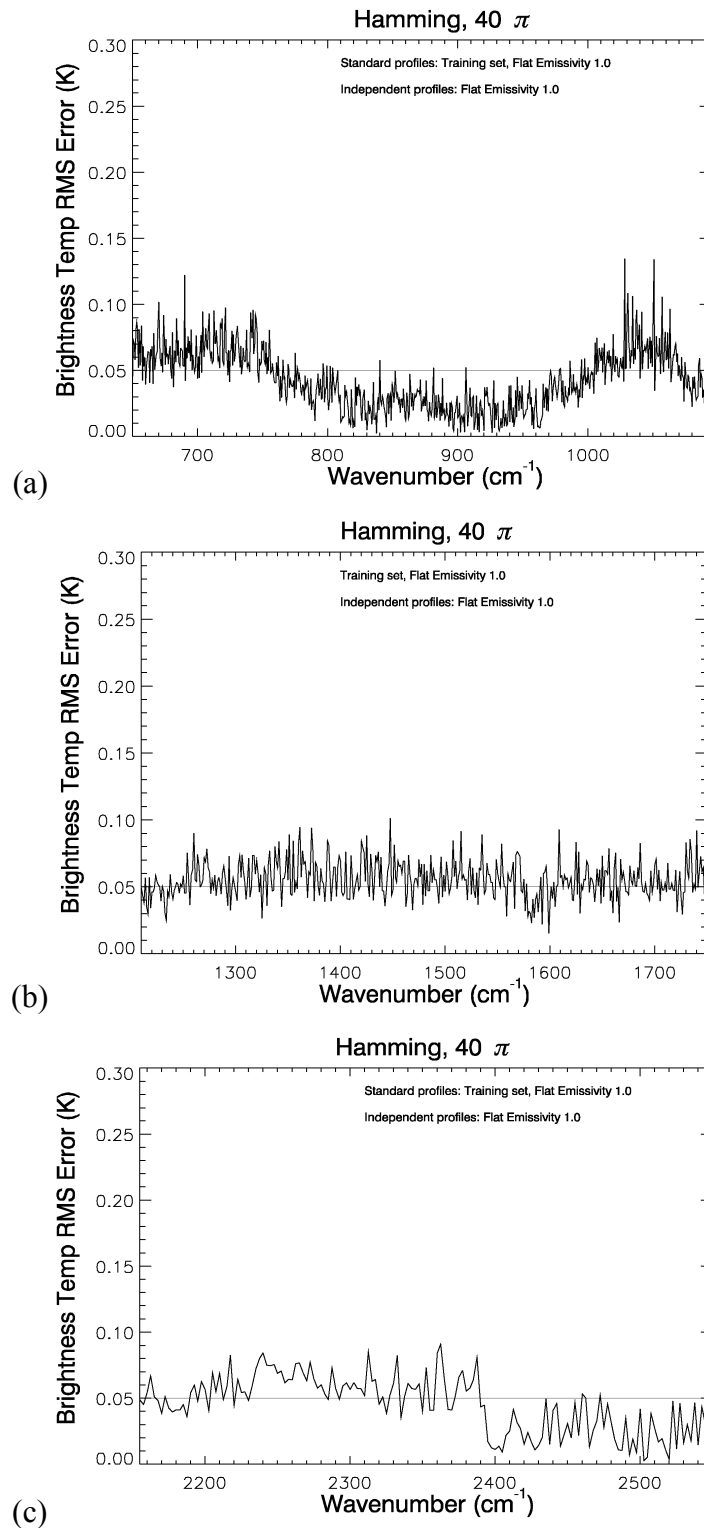


Figure 43: RMS differences between OSS-generated & true radiances for *Blackman* ILS with 3 side lobes. (a) LWIR, (b) MWIR, (c) SWIR.

Figure 44: Similar to Figure 43, but for *Hamming* ILS with 40 side lobes.

3 Transformation Between Apodized and Unapodized Spectra

Let us assume that instrument channels are not limited with a number of side-lobes and that they are set through the whole bandwidth in accordance with the Nyquist interval.

The easiest way to illustrate how the transformation between apodized and unapodized spectra works can be done on the example of *Hamming* and *Sinc* functions. Let us denote the channel response functions by $\phi_H(\nu)$ for *Hamming* and $\phi_U(\nu)$ for *Sinc*. The following relationship is valid between these functions (see Appendix 4):

$$\phi_H(\nu) = (1 - 2a) \phi_U(\nu) + a (\phi_U(\nu - \pi/L) + \phi_U(\nu + \pi/L))$$

Equation 64

The true radiance ascribed to the i -th channel can be defined as follows (ν_i is the channel center)

$$R_{\Delta\nu}^{(i)} = \int_{\nu_{\min}}^{\nu_{\max}} d\nu R(\nu) \phi(\nu - \nu_i) / \int_{\nu_{\min}}^{\nu_{\max}} d\nu \phi(\nu - \nu_i)$$

Equation 65

where $\Delta\nu = \nu_{\max} - \nu_{\min}$. The apodized radiance is related to its unapodized counterpart through

$$R_{c,H}^{(i)} = (1 - 2a) \beta_{i,i} R_{c,U}^{(i)} + a (\beta_{i,i-1} R_{c,U}^{(i-1)} + \beta_{i,i+1} R_{c,U}^{(i+1)})$$

Equation 66

where the coefficients β are defined:

$$\beta_{i,j} = \int_{\nu_{\min}}^{\nu_{\max}} d\nu \phi_U(\nu - \nu_i) / \int_{\nu_{\min}}^{\nu_{\max}} d\nu \phi_H(\nu - \nu_i)$$

Equation 67

When the range of ν_{\min} and ν_{\max} is infinitely wide, β equals to 1.0. Otherwise, for channels near band edge, the β values are different from 1.0 and the edge effect appears.

APPENDIX 2: CHANNEL SELECTION

1 Introduction

The CrIS design provides over a thousand channels (see Table 7). However, not all of these channels need to be used in order to meet the CrIS accuracy requirements. An inspection of Equation (42) indicates that channels with small values of the partial derivatives K contribute little to the retrieved state vector. Eliminating those channels from the retrieval would therefore have little impact on the retrieval accuracy, but it would help in speeding up the retrieval process. In order to select an optimal subset of channels meeting CrIS accuracy and timing requirements, we have employed a modified version of the entropy-based method described by Rodgers (1996). This appendix provides a description of our channel selection method and offers an illustration of the impact of channel selection on the temperature and water vapor retrievals.

2 Description of the Method

The channel selection is performed sequentially by ranking channels according to their information content. The entropy (or information content) gained by adding the i^{th} channel to the retrieval can be expressed as:

$$\delta S_i = \frac{1}{2} \ln(1 + \hat{k}_i^T \hat{S}_{i-1} \hat{k}_i)$$

Equation 68

where \hat{S}_{i-1} is the normalized covariance matrix given $i-1$ previously selected channels and \hat{k}_i is the vector containing the normalized derivatives for the i^{th} channel. The normalization is done according to the formula:

$$\hat{k} = S_e^{-\frac{1}{2}} K S_a^{-\frac{1}{2}}$$

Equation 69

in which multiplication by $S_y^{-\frac{1}{2}}$ normalizes K with respect to its measurement errors and taking the product $KS_x^{-\frac{1}{2}}$ removes the intra-channel dependencies. At the beginning of the selection process (i.e., for $i=0$), \hat{S}_i is equal to the identity matrix:

$$\hat{S}_0 = I = S_x^{-1}S_x$$

Equation 70

The change in entropy is then calculated for each channel using Equation 68. After locating the channel with the largest δS , \hat{S}_i is updated using the formula:

$$\hat{S}_i = \frac{\hat{S}_{i-1} \left\{ I - \hat{k}_i (\hat{S}_{i-1} \hat{k}_i)^T \right\}}{1 + \hat{k}_i^T \hat{S}_{i-1} \hat{k}_i}$$

Equation 71

and the process (i.e., Equation 68 and Equation 71) is repeated until all channels have been ranked or $\delta S \approx 0$.

The following modifications to the original algorithm described by Rogers have been adopted:

1. In order to meet EDR accuracy requirements, the channels are selected separately for temperature, water vapor, and surface parameters (i.e., the appropriate S_x and K matrices are constructed for each EDR) and then combined into a single set. The combined channel set contains prescribed fractions of channels from the sets computed for each EDR (subject to constraints on the maximum number of channels from each EDR set)
2. Some channels are eliminated prior to the selection process based on their water vapor and trace gas derivatives. This pre-selection technique is designed to eliminate channels sensitive to water vapor from the temperature channel set and those that are affected by trace from the

temperature, water vapor, and surface parameter retrieval. Only channels with derivatives falling below a set threshold are incorporated into the entropy-based selection process.

3. A priori information can be used to eliminate certain channels and/or bands. This is done by modifying elements of the measurement covariance matrix S_y when calculating δS from Equation 68. In particular, setting a diagonal element in S_y to a large positive value reduces $k_i S_y^{-1}$ and the corresponding δS_i for the channel.

4. Entropies are computed using K and δS calculated for N different atmospheric profiles, selected by latitude (e.g., polar, mid-latitude, tropics) and/or terrain type (e.g. ocean, land), with the total entropy for the i^{th} channel equal to the sum of entropies for each profile:

$$\delta S_i^{\text{total}} = \sum_{j=0}^N \delta S_{ij}$$

Equation 72

3 Implementation and Retrieval Results

The channels entropies have been sequentially ranked for 5 parameters (temperature with and without MWIR, water vapor, skin temperature, surface emissivity, and solar reflectivity), with several atmospheric profiles (polar, mid-latitude, and tropical, ocean/land) used to calculate the derivatives. Trade studies involving subsets of these profiles have produced different channel sets, but they had small impact on the retrieval performance. As noted above, spectral regions where trace gas derivatives exceed a certain threshold are excluded from the channel selection in order to minimize trace gases interference with the retrievals. The trace gases considered are O₃ (LWIR), CH₄/N₂O (MWIR) and CO/ N₂O (SWIR). In addition, for temperature channel selection we also excluded channels sensitive to water vapor. The water vapor and trace gas derivatives and their threshold values are shown in Figure 45 and Figure 46. These figures also illustrate a typical selected set containing 350 channels. As shown in Figure 46, the threshold value adopted for the N₂O derivatives results in most SWIR channels being retained by the selection process. This choice minimizes errors in the retrieved skin temperatures. Figure 47

shows a typical plot of temperature entropy as a function of wavenumber. This plot illustrates that MWIR contains a significant portion of the temperature information. However, since these channels are also sensitive to water vapor, they were not used in selecting channels for temperature retrievals.

The results from the entropy ranking process for each EDR were used to construct a single channel set for simultaneously retrieving temperature, water vapor, and the surface parameters. This combined channel set is constructed as follows: 30% of channels are the top-ranked channels selected for temperature without MWIR, 14% are from the channels for temperature with MWIR (maximum of 40 channels), 14% for water vapor (maximum of 40 channels), 14 % skin temperature (maximum of 50 channels), 14% emissivity (maximum of 30 channels) and 14% for reflectivity (maximum of 30 channels). The combined sets totaling between 25 and 500 channels are illustrated in Figure 48. A channel selection of 350 elements is also illustrated in Figure 45 and Figure 46, with the channels for that selection listed in Table 16.

The channel sets from Figure 48 were used to simultaneously retrieve temperature, water vapor, and surface parameters from a diverse set of simulated data and the resulting errors were compared to those obtained using all CrIS channels. The profiles of RMS errors for temperature and water vapor obtained using sets of 150, 300, and 400 channels are shown in Figure 49 for the case of 200 clear-sky ocean simulations. As can be seen, the retrievals based on 300-400 channels are nearly identical, in the RMS sense, to those obtained using the full complement of CrIS channels. Consequently, the current version of the CrIS employs a set containing 400 channels. This reduction in the number of channels relative to the full set of channels leads to a ~2.5 fold increase in the computational speed for the retrieval algorithm. Most of these gains result from the reduction in the number of forward model calculations and of matrix inversions.

Table 16: Selected Channels for CrIS.

EDR	IR wavenumber (cm ⁻¹)	Number of Channels Selected
Temperature	662.5-908.75	144
	1231.25-1535.0	23
	2160.0-2400.0	63
Water Vapor	1337.5-1652.5	40
Skin Temperature	1095.0-1246.25	29
Surface Emissivity and Reflectivity	2160.0-2492.5	21

APPENDIX 2: CHANNEL SELECTION

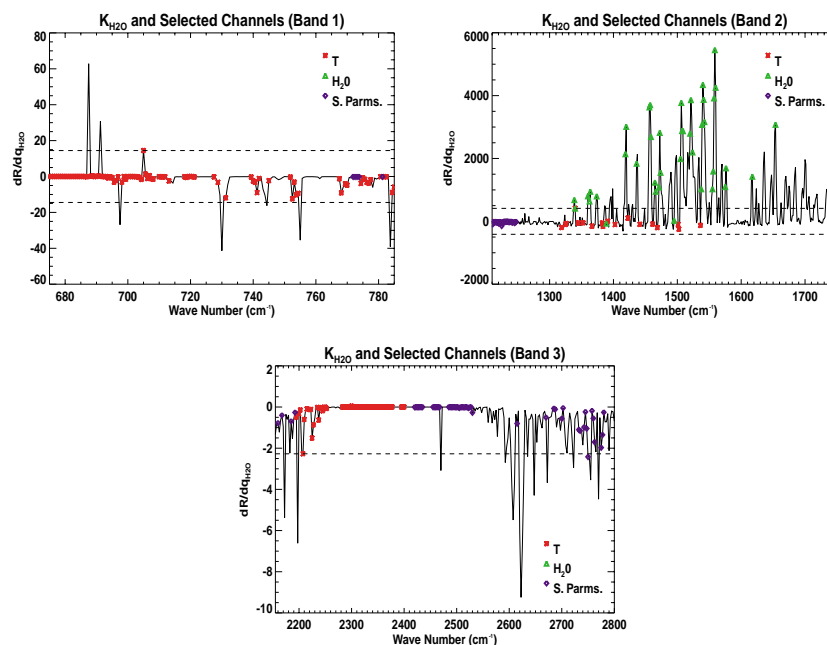


Figure 45: Water vapor derivatives and selection thresholds. Channels for which the absolute values of water vapor derivatives exceed the threshold are excluded from the entropy-based channel selection for temperature

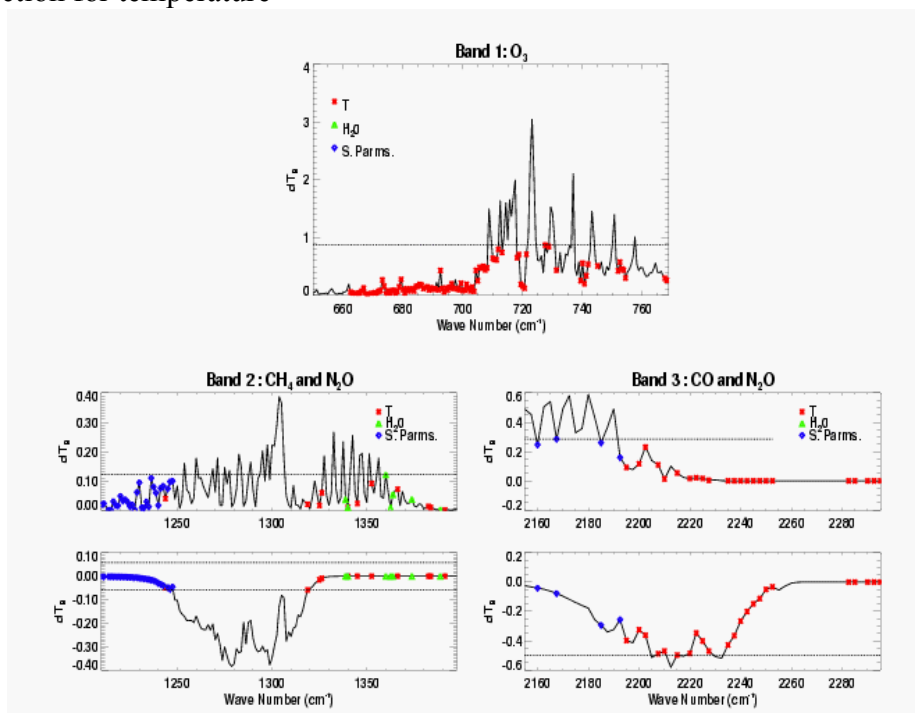


Figure 46: Trace gas derivatives and selection thresholds. Channels for which the absolute values of trace gas derivatives exceed the threshold are excluded from the channel selection for temperature, water vapor, and surface parameters.

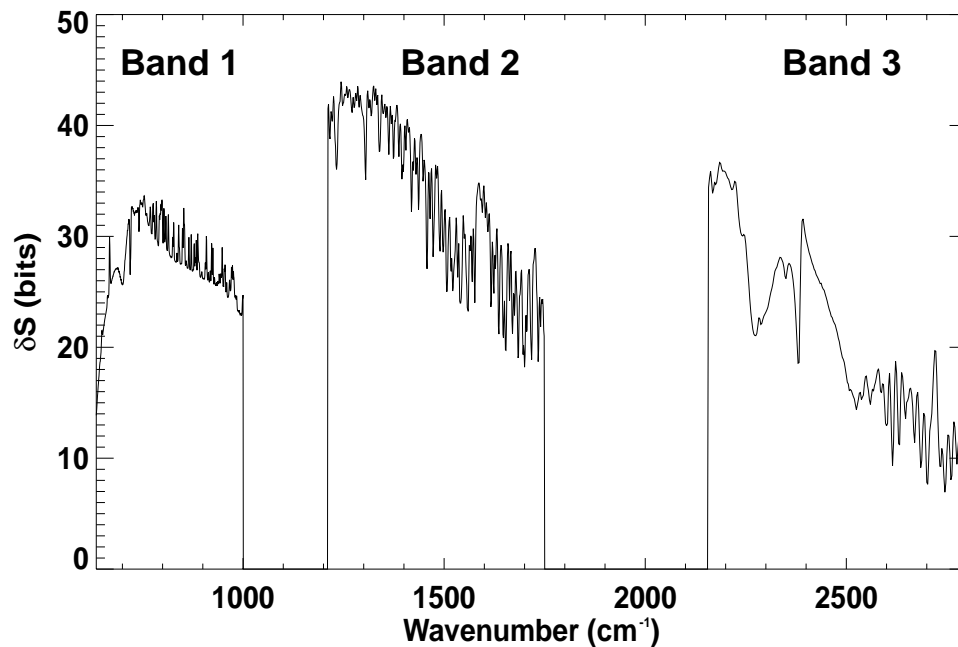
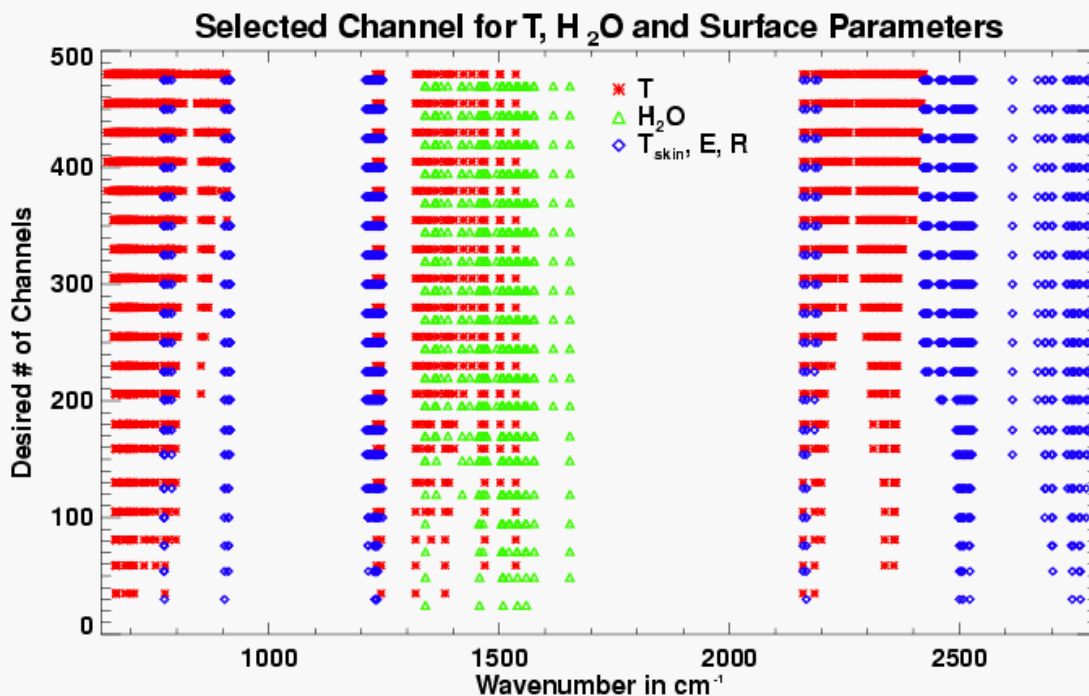
Figure 47: Typical Temperature Entropy (δS) per Channel.

Figure 48: Selected channels for temperature T (with and without MWIR), water vapor, and the surface parameters as a function of the total number of channels. The temperature channels selected in MWIR are based on information in all three bands (non-weighted S_e).

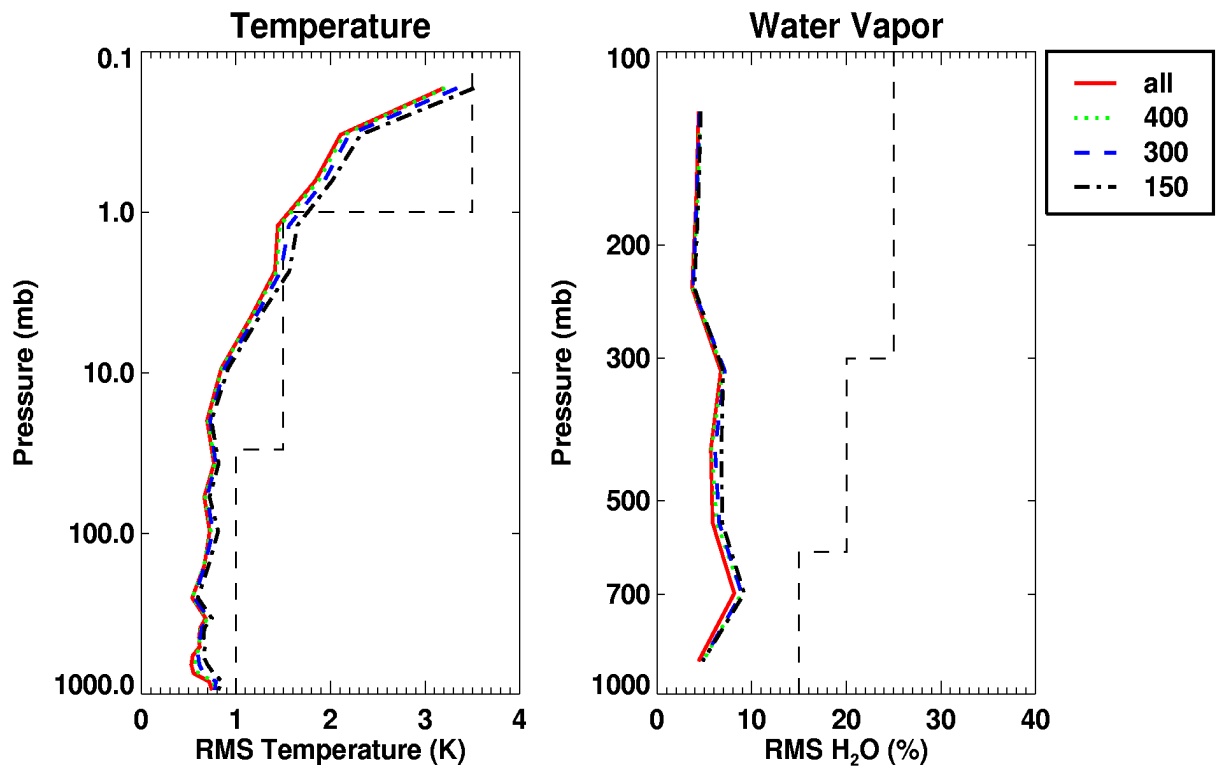


Figure 49: RMS errors for temperature and water vapor for 200 clear-sky ocean scenes. Results from second stage retrievals performed using all IR channels and subsets of 150, 300, and 400 channels are shown.

APPENDIX 3: EMPIRICAL ORTHOGONAL FUNCTIONS

1 Introduction

The Principal Component Analysis (PCA) represents the temperature and moisture profiles as a linear combination of Empirical Orthogonal Functions (EOFs) and allows the retrieval of the projection coefficients onto selected EOFs (20 for temperature, 15 for moisture), rather than the full profiles. This leads to a reduction in the dimension of the retrieved state vector and speeds up the retrieval process (in the current version of the code, the gain in speed is about 60%). Another advantage of PCA is that it helps to overcome the ill-conditioning of the background covariance matrix used in the retrieval of the full moisture profiles. This ill-conditioning is caused by the lack of moisture measurements above 300 mb and becomes progressively worse as the number of vertical levels is increased (due to inter-level correlations).

2 Principal Component Analysis of the NOAA-88 profiles

The EOFs for the temperature and moisture profiles can be obtained by performing PCA directly on 8344 profiles in the NOAA-88 database. Figure 50 shows the first 6 EOFs for temperature, with the first eigenvector representing the mean temperature profile. As the eigenvalues associated with each EOF decrease, the eigenvectors exhibit more detailed structure and their contributions to the reconstructed profiles decrease. In our implementation, PCA is applied to the covariance matrix generated from the 8344 profiles, with the original profiles reconstructed by adding the mean profile to the linearly combined EOFs. These two methods are equivalent. The accuracy of the reconstructed profiles depends on the number of selected EOFs. Figure 51 shows the mean error and standard deviation for the 8344 profiles represented using 20 EOFs. With 20 EOFs the original profiles can be reconstructed to better than 0.8 K at all pressure levels. Note that in Figure 51 the standard deviation is calculated at each pressure level. As shown in Figure 52, the error is smaller than 0.4 K at most altitudes when computed in a layer-mean sense.

Figure 53 is a typical plot of the original and reconstructed temperature profiles. The differences appear on small vertical scales, with the result that the differences in radiances calculated using the original and reconstructed profiles are smaller than instrumental noise. This indicates that at

CrIS spectral resolution, the measurement is not sensitive to very fine vertical structures. We also applied 20 eigenvectors to represent 1761 temperature profiles in the TIGR (TOVS Initial Guess Retrieval) database (Chedin *et al.* 1985). The error pattern is very similar to that in Figure 51, except above 30 mb. This is because both NOAA-88 and the TIGR data set have very limited measurements above 30 mb and different extrapolation methods generate different profiles above 30 mb. Due to the lack of accurate radiosonde measurements of moisture profiles above 100 mb, 21 levels were used to represent moisture profiles below 100 mb. The moisture value varies by orders of magnitudes between surface and 100 mb, therefore the SVD is performed on natural logarithm of moisture profiles. Figure 54 shows the first 6 EOFs for moisture profiles. Similar to the guideline used for temperature profiles, we selected 15 principal components to represent the moisture profiles.

Figure 55 shows the mean errors and standard deviation of the regenerated NOAA-88 moisture profiles. The percent rms error is less than 3% for all pressure levels between 1000 to 100 mb. With these 15 principal components, we can regenerate TIGR profiles better than 2% below 300 mb and better than 7% above 30 mb. Further studies have shown that reducing the number of EOFs to 10 does not degrade the moisture retrievals in our simulations. Figure 56 shows the mean errors and standard deviation of the regenerated NOAA-88 moisture profiles using only 10 EOFs.

3 Transformation of Retrieval Variables

In our physical retrieval algorithm, the following equation is used to solve for state vector x :

$$x_{n+1} = x_a + (K^T S_y^{-1} K + S_x^{-1})^{-1} K^T S_y^{-1} [(y^m - y_n) + K(x_n - x_a)]$$

Equation 73

where K is the Jacobian, S_y is the error covariance matrix, S_x and x_a are background covariance matrix and background state vector, respectively. After eigenvector transformation, the previous equation becomes

$$u^T x_{n+1} = u^T x_a + (u^T K^T S_y^{-1} K u + u^T S_x^{-1} u)^{-1} u^T K^T S_y^{-1} [(y^m - y_n) + K(x_n - x_a)]$$

Equation 74

where u is the matrix which contains the 20 EOFs for temperature and 15 EOFs for moisture. X is the state vector (such as temperature and moisture profiles) to be retrieved. When Sx is produced from original training profiles, one can write:

$$u^T S_x^{-1} u = \Lambda^{-1}$$

Equation 75

where Λ is a diagonal matrix whose diagonal elements equal to the eigenvalues of background error covariance matrix. The vector $u^T x$ represents the projection coefficients of state vector onto EOFs.

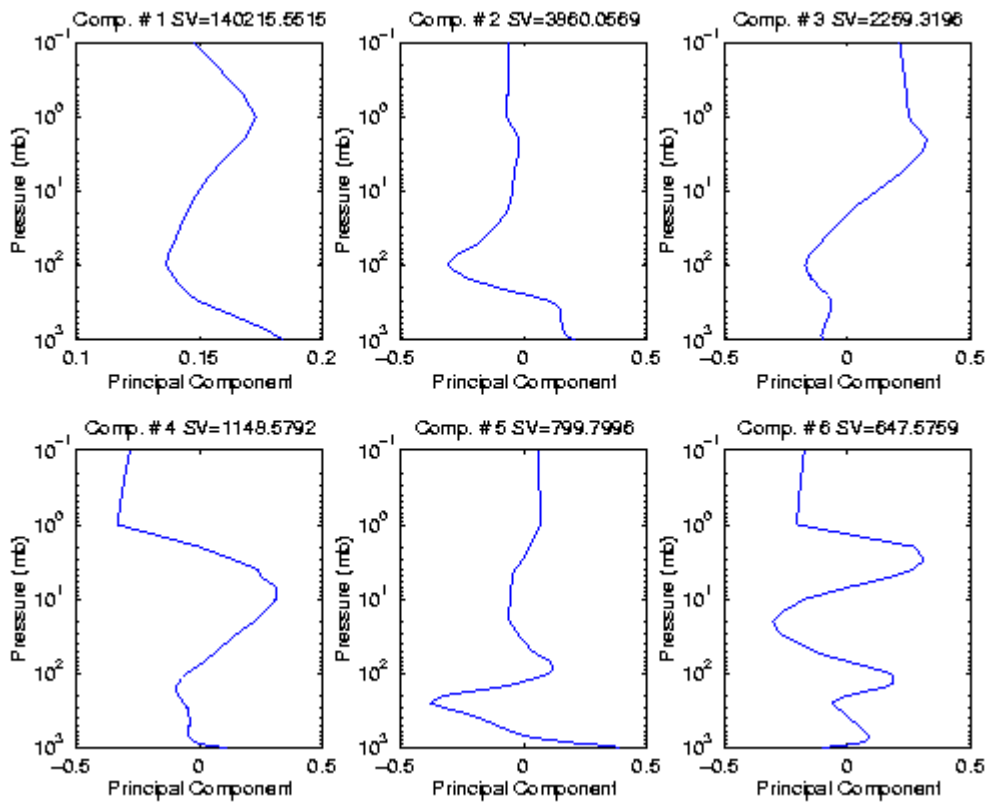


Figure 50: First 6 EOFs of NOAA-88 temperature profiles. SV stands for the square root of eigenvalue.

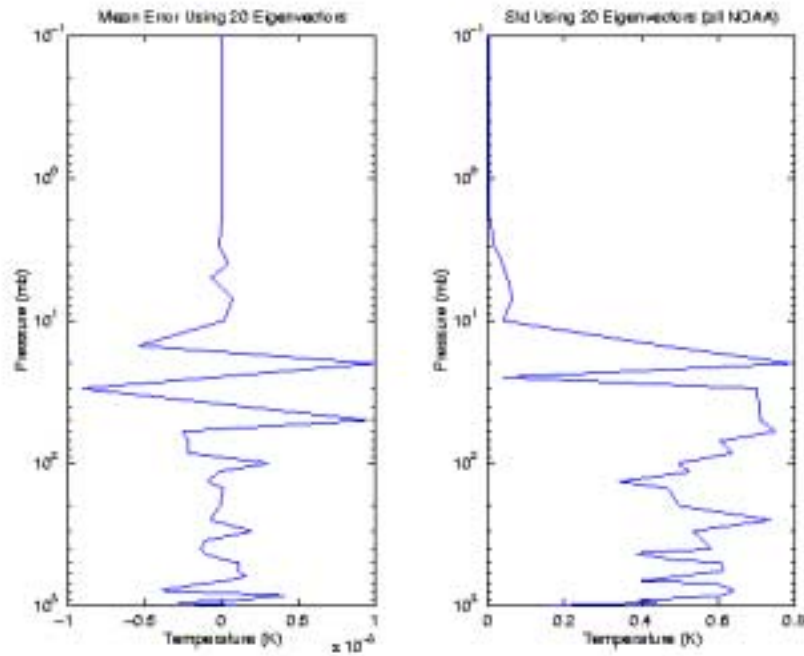


Figure 51: BIAS and RMS representation errors of NOAA-88 temperature profiles using 20 EOFs.

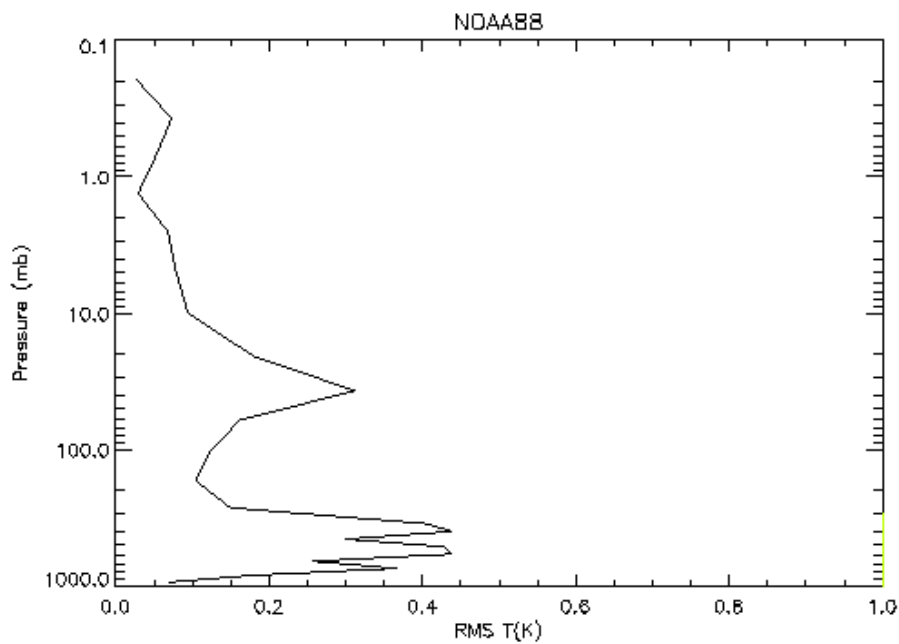


Figure 52: Layer-mean representation errors of NOAA-88 temperature profiles.

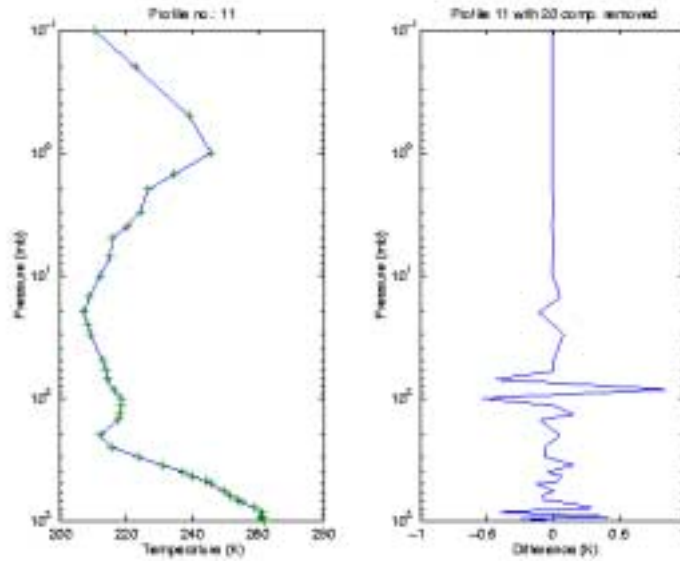


Figure 53: The original NOAA-88 temperature profile (solid line) and the profile reconstructed using 20 EOFs (stars). The plot on the right is the difference.

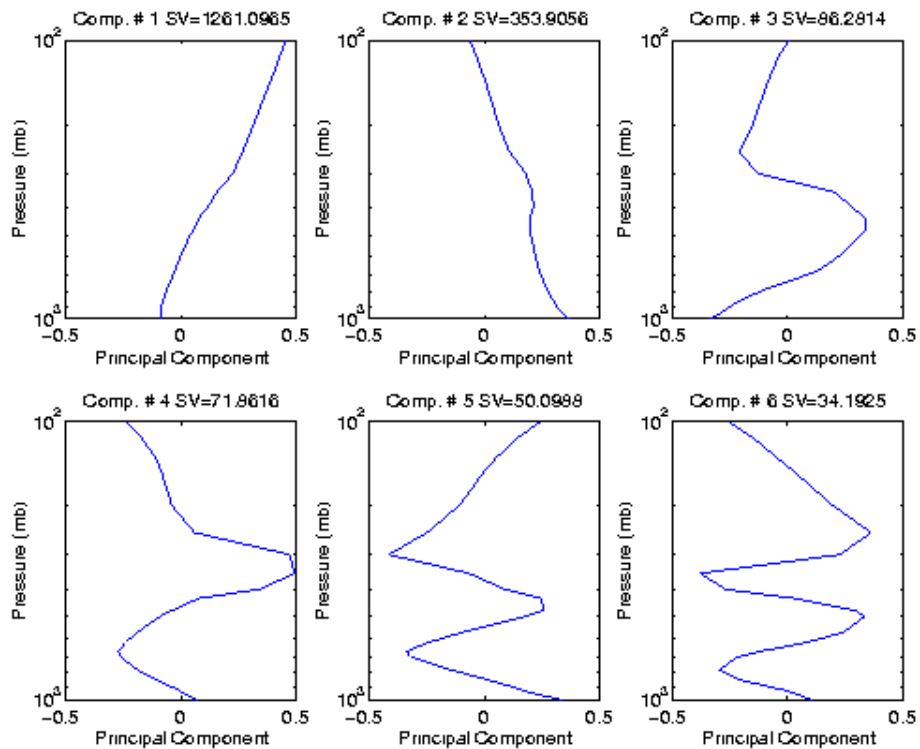


Figure 54: First 6 EOFs as a result of applying PCA to NOAA-88 moisture profiles. SV stands for the square root of eigenvalues.

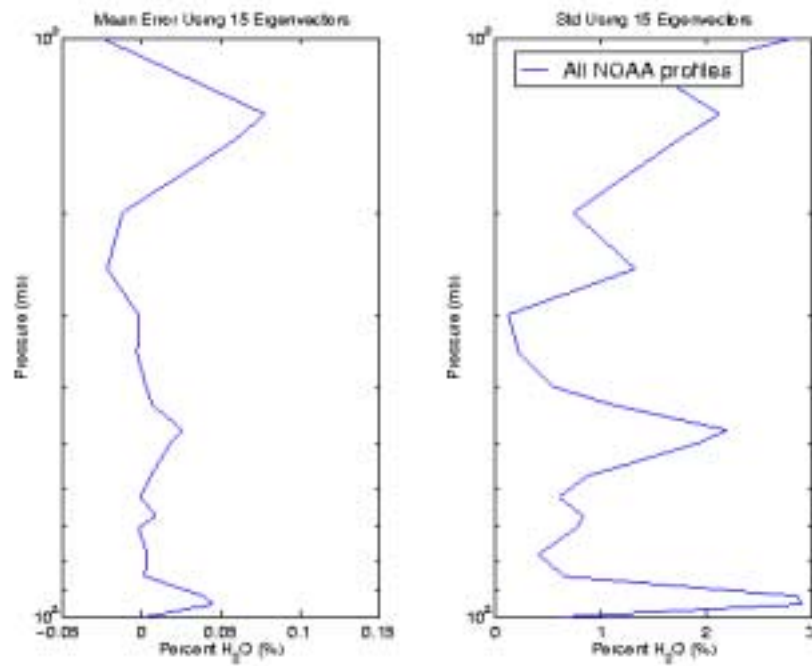


Figure 55: BIAS and RMS errors of the reconstructed NOAA-88 moisture profiles using 15 eigenvectors.

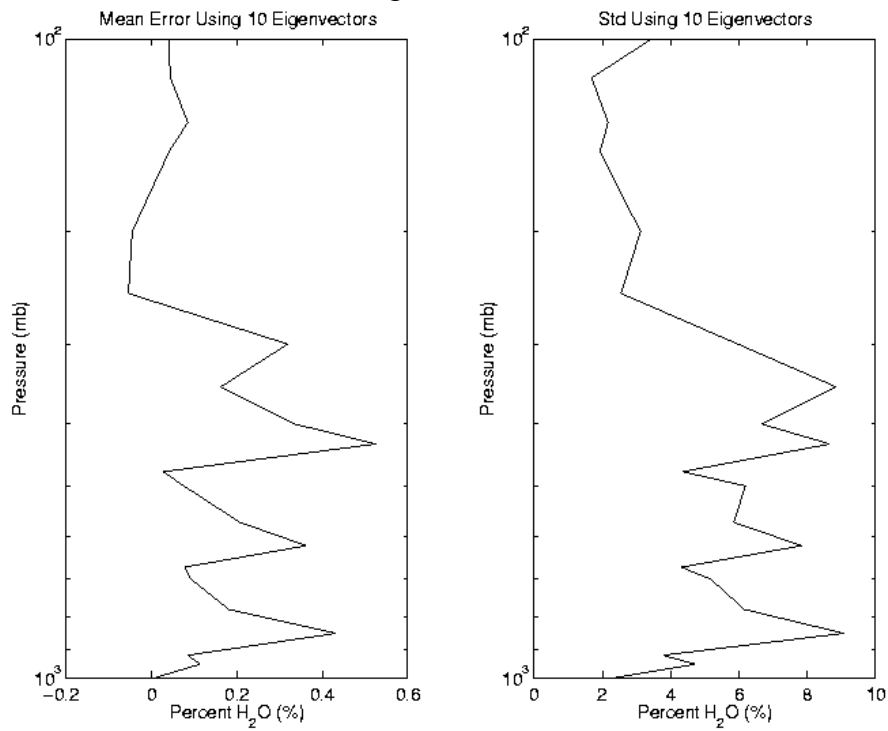


Figure 56: BIAS and RMS errors of the reconstructed NOAA-88 moisture profiles using 10 eigenvectors.

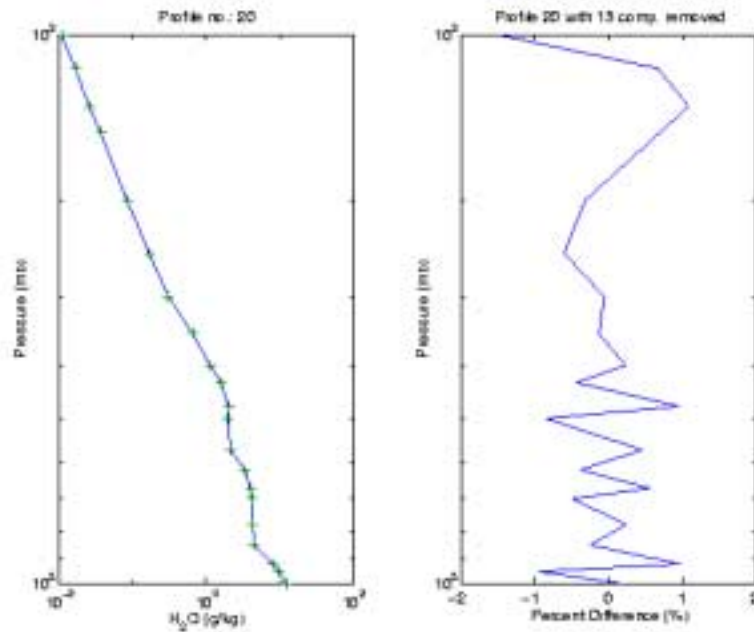


Figure 57: Example of the original and reconstructed moisture profiles and its difference.

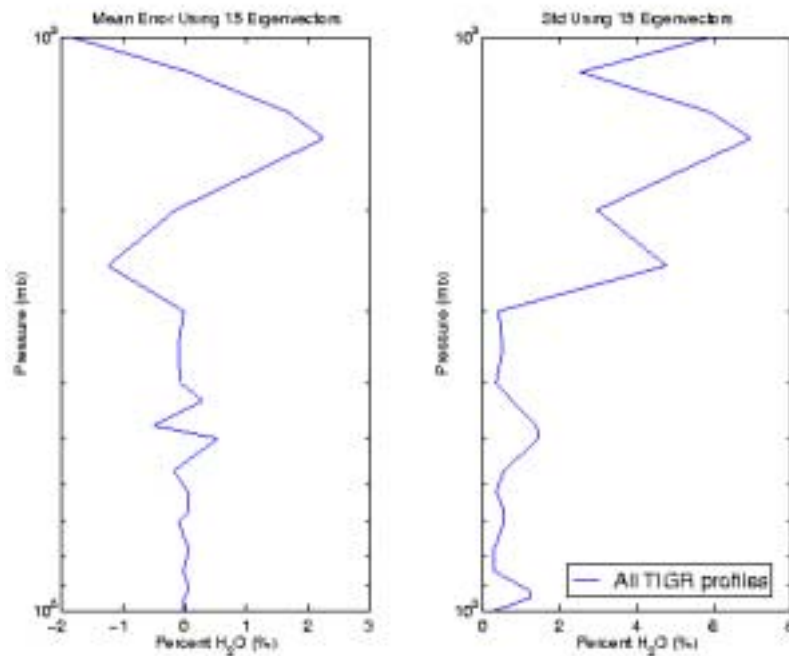


Figure 58: BIAS and RMS error when applying the eigenvectors obtained from the analysis of the NOAA-88 moisture profiles to reconstruct the TIGR moisture profiles.

APPENDIX 4: SIGNAL APODIZATION

From Section 3.5 of the CrIS SDR ATBD (BOMEM).

1 Introduction

Both spectral characteristics and signal-to-noise are critical to retrieval accuracy of advanced IR sounders. For an unapodized (boxcar apodized) interferometer, the channel response function, given by the cosine transform of the apodization function, is a $\text{sinc}(\sigma)$ function, where σ is proportional to the frequency separation from the channel center. This function has large side-lobes that alternate in sign and fall off slowly with increasing frequency separation. Typically, interferograms are apodized (the interferogram is multiplied by a function which, in effect, smoothes the spectrum) to produce a channel response function that is localized and has small side-lobes. When the Hamming apodization function is compared to other apodization functions found in the literature, it is found that it is a reasonable function to use for remote sensing purposes if the instrumental signal-to-noise is on the order of 1000. This section discusses the effects of apodization as they relate to sounding applications and shows that apodization should have no effect on retrieval results. In conclusion the Hamming FWHM is a reasonable value to use when describing the effective spectral resolution of the proposed IR interferometric sounders.

2 Unapodized Channel Response Function

The raw data product from an interferometer is a cosine transform of the incoming radiance (interferogram). The instrument has a finite maximum optical path difference, MPD . One obtains the radiance spectrum, convolved with a channel response function, by taking the cosine transform of the product of the interferogram, $I(x)$, with an apodization function, $A(x)$. The channel response function is the cosine transform of the apodization function.

In the interferogram domain, the unapodized (or boxcar) apodization function is defined as:

$$A(x) = \begin{cases} 1 & \text{for } |x| \leq MPD \\ 0 & \text{for } |x| > MPD \end{cases}$$

Equation 76

where x is the optical path difference. The channel response function for an unapodized interferometer is:

$$\frac{\sin(2\pi MPD\sigma)}{2\pi MPD\sigma} \equiv \text{sinc}(2MPD\sigma)$$

Equation 77

where σ is wavenumber. The unapodized channel radiance $S(\sigma)$ is given by a convolution of the channel response function with the monochromatic radiance at the entrance to the interferometer:

$$S(\sigma) = S_0(\sigma) * \text{sinc}(2MPD\sigma)$$

Equation 78

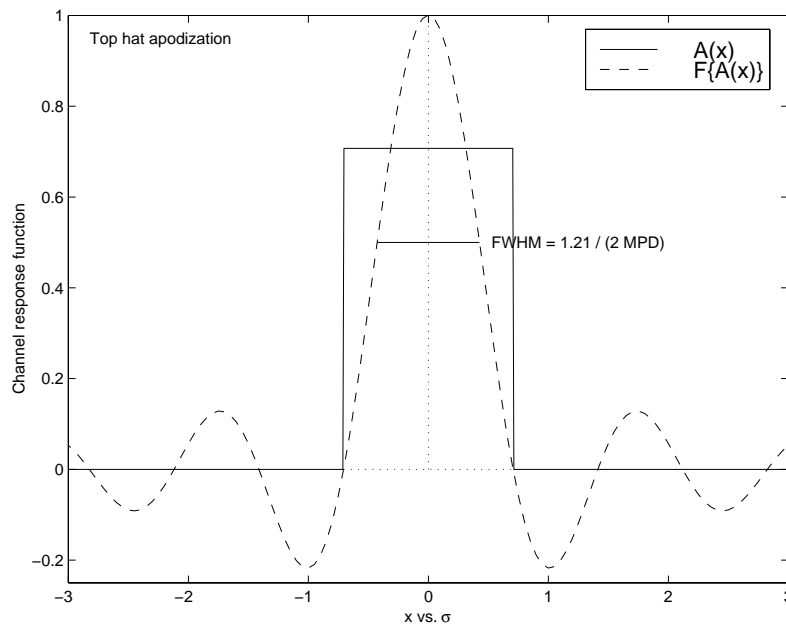


Figure 59: Boxcar Apodization Function and its Sinc Fourier Transform.

The Nyquist sampling theorem states that the optimal sampling of channels is such that the channel spacing is $\Delta\sigma = 1/(2MPD)$ in the frequency domain. No additional information is gained by sampling the interferogram at a higher rate, although information is lost if the interferogram is sampled at a lower rate. The resulting unapodized spectrum is given as an array of radiance values, $S(\sigma)$ (or $S[n]$ where n is the channel index number).

The sinc function has large side-lobes which alternate between negative and positive about the zeroes of the function spaced at $\sigma = \pm n/(2MPD)$. The first four side-lobes have heights of -21.7% , $+12.8\%$, -9.1% , and $+7.1\%$ with respect to the central lobe. The full-width-half-maximum (FWHM) of the sinc function is:

$$FWHM = \frac{0.603355}{MPD} \approx \frac{1.21}{2MPD}$$

Equation 79

This equation has been used to describe the effective spectral resolution of an interferometer. Such a definition can be used to compare the resolution of one interferometer to another, with different values of MPD . This definition is misleading, however, if one attempts to compare the spectral resolution of an interferometer to that of an instrument in which the channel response function does not have side-lobes. In typical bandpasses, only 45% of the unapodized spectral radiance comes from the central lobe. The remainder of the radiance comes primarily from the first few side-lobes, but non-negligible contributions arise from very distant frequencies within the bandpass, as the heights of the unapodized channel response function side-lobes are still above 1% at 30 zeroes from the central lobe.

In addition to not having a well defined resolution, the use of non-localized unapodized radiances produces complications in the retrieval of geophysical parameters. For multispectral retrievals (e.g., combining microwave and infrared radiances) it is convenient, but not necessary, to represent radiances in brightness temperature (i.e., the temperature of a blackbody with the same radiance). For unapodized spectra, brightness temperature is a meaningless concept due to the distortion, caused by the negative side-lobes which can produce negative channel radiances.

The unapodized channel response function also produces complications in the development of efficient and accurate methods to compute channel radiances, such as the use of channel averaged transmittance functions.

3 Hamming's Filter Function

Many apodization functions can be applied to an interferogram which will localize the channel response function for the purpose of generation of rapid and accurate radiances. It is desirable to use an apodization function which satisfies retrieval models and also allows for the ability to transform apodized radiances into unapodized radiances, if this is required. A simple cosine apodization function is found to satisfy all of these requirements. The cosine apodization function is given by:

$$A(x) = \begin{cases} (1 - 2a) + 2a \cos\left(\pi \frac{x}{MPD}\right) & \text{for } |x| \leq MPD \\ 0 & \text{for } |x| > MPD \end{cases}$$

Equation 80

which has values of $A(x=0)=1$ and $A(x=MPD)=1-4a$. The channel response function is given by the cosine transform of the previous equation and is equal to:

$$H(\sigma) = 2MPD \cdot \text{sinc}(2MPD\sigma) \left[(1 - 2a) + 2a \frac{(2MPD\sigma)^2}{1 - (2MPD\sigma)^2} \right]$$

Equation 81

Apodized radiances can be shown to be equivalent to a 3-point running mean of unapodized radiances if the Nyquist channel spacing of $\Delta\sigma = 1 / (2MPD)$ is used:

$$L[n] = (1 - 2a) \cdot L[n] + a(L[n-1] + L[n+1])$$

Equation 82

Hamming found an optimum value of a that minimized the first side-lobe of the channel response function. He also showed that the optimum value of a was a function of the number of points in the spectrum; however, the optimum value of a converged to $a = 0.23$ for more than 100 points. With this value for a , the FWHM is equal to $1.8152/(2 \text{ MPD})$, which is 50.4% larger than FWHM of the sinc.

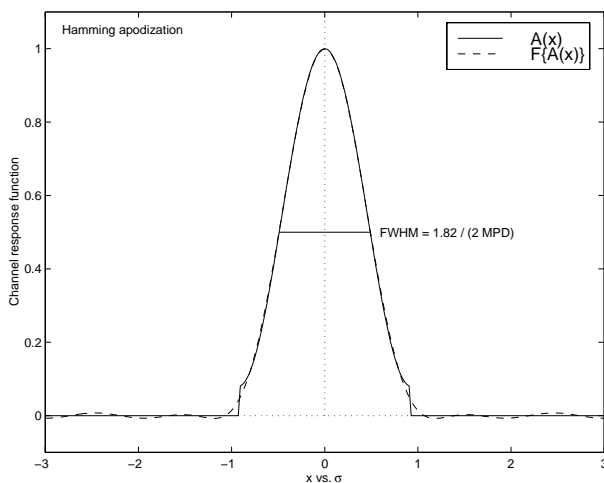


Figure 60: Hamming Apodization Function and its Fourier Transform.

One result of apodization is that the noise becomes correlated between neighboring channels. For $a = 0.23$, the 3-point running filter reduces the noise in a given channel by a factor of 1.6; however, noise in adjacent channels is correlated by 62.5% and noise in channels separated by $\Delta\sigma = 1 / (2 \text{ MPD})$ is correlated by 13.3%. In the case of the Hamming channel response function, the residuals are considerably less than the expected instrument noise levels for advanced sounders, which are on the order of 0.1°C . The information content only depends on the value of MPD , not on the apodization function. The Gaussian apodization function has similar qualities to the Hamming function but has significant values extending to larger MPD . This implies that more information content exists in the Gaussian response function and that the small side-lobes of the Hamming channel response function actually degrade the resolution compared to the Gaussian function, so that the effective resolution of the interferometer is actually slightly poorer than $1.8/(2 \text{ MPD})$.

The inverse transformation can be expressed as:

$$L[n] = \frac{c_0}{(1-2a)} \left(L[n] + \sum_{i=1}^N r^i \cdot (L[n+i] + L[n-i]) \right)$$

Equation 83

with $c_0 = 1.909188309204$, and $r = -0.5590375815769$ for the Hamming case ($a = 0.23$). The set of unapodized radiances and cosine apodized radiances are linear combinations of each other.

Hence, the information content of the complete set of radiances, including noise effects, is identical. This implies that retrieval results using unapodized radiances, or cosine apodized radiances with $0 < a < 0.25$, should produce identical results provided all the channels are used. Furthermore, it implies that while the width of the central response function of an apodized function is larger than that of the unapodized function, there is no loss in "resolution" as both sets of functions contain equivalent information. We conclude that the Hamming function is an optimal function for use as a basis for calculating radiances for itself or other apodization functions, and also reasonable for use in analysis of data because:

- It gives a good trade-off between spectral purity and apparent spectral resolution.
- The channel noise correlation is localized.
- A simple analytic inverse exists.

In addition, radiance calculations need only be done for the subset of channels being used in the retrieval process. In cases where the signal-to-noise is about 1000, the Hamming side-lobes contribute less than the noise value to the radiance calculation and the Hamming radiances are indistinguishable from those radiances calculated from localized channel response functions. The inverse Hamming matrix utilizes all the Hamming channel radiances and, therefore, can be used to create radiances for apodization functions with smaller side-lobes.

APPENDIX 5: INVERSION METHODS

1 Introduction

The approach adopted for retrieving temperature and water vapor profiles from the CrIS sensor data is an iterative Maximum Likelihood approach. In the notation of Rodgers (1976), this method for updating the parameter vector, x , at the i^{th} iteration is:

$$x_{i+1} = x_a + (K_i^T S_y^{-1} K_i + S_x^{-1})^{-1} K_i^T S_y^{-1} [(y_0 - y_i - K_i(x_a - x_i))]$$

Equation 84

where x_a is an initial guess for x , S_x is its associated covariance matrix, K is a matrix containing the current partial derivatives of the observed data, y , with respect to $x(\partial y/\partial x)$ and S_y is a matrix that describes the measurement errors. In this case, the measurement errors are assumed to be uncorrelated and S_y is a diagonal matrix.

In this study, the Maximum-Likelihood (ML) method was compared with two methods for retrieving EDR from CrIS SDR: the Levenberg-Marquardt (L-M) method and a new method, the Δ radiance or DRAD method. The three methods were evaluated based on their convergence properties and their resulting EDR errors. Each algorithm was tested using sets of simulated data to mimic different environmental and initial conditions. The results show that the DRAD algorithm has the best overall performance characteristics.

2 Retrieval Methods

The three methods considered in this convergence trade study are the ML, L-M and DRAD algorithms. The ML or inverse Hessian method attempts to minimize the errors in the measurement space based on the assumption that it can be approximate using a quadratic (Press *et al.* 1992).

The standard L-M algorithm uses a single control parameter, λ , to choose between the ML algorithm when the error is approximately quadratic, and a more conservative approach, the

steepest descent method, when the error is nonlinear in nature. The L-M algorithm implemented in this trade study, used λ to control the extent to which the unconstrained solution (in part described by the term $K_i S_e^{-1} K_i$ in the previous equation), and the constrained solution (represented in part by S_a) is incorporated into each retrieval step.

The DRAD algorithm is a simple alternative to L-M. It attempts to compensate for the non-quadratic nature of the error surface by modifying S_y . At each iteration, the values of S_y are set to either some fraction of the error in the observed space, the difference between y_i and the observed radiance (y_0), or to the noise variance:

$$S_y(j, j) = \max \left[\frac{1}{\alpha} (y_i(j) - y_0(j))^2, \sigma^2(j) \right]$$

Equation 85

where α is the error control parameter and $\sigma^2(j)$ is the instrument noise variance for the j^{th} channel. The value $\alpha=2$ has been used in this study.

3 Simulation Results

The three algorithms were tested using sets of simulated observations. Each set represented a different environmental or operating condition. In the first set of test cases, 200 profiles were retrieved using simulated radiances to mimic clear and cloudy land/ocean conditions. In all cases, a simulated MHS microwave retrieval was used to provide an initial guess for the IR based CrIS retrievals. The profiles, in the clear-sky cases, were obtained using simulated radiances for one CrIS instantaneous field-of-view (FOV), and the cloudy profiles were estimated using the radiances for 3 FOVs and the cloud clearing algorithm. The radiances for the cloudy cases were simulated using a 2 layer cloud model. This simulated cloud structures had cloud tops at 396 and 618 mb, and cloud fractions of (0.13, 0.12), (0.23, .22) and (0.32, 0.33) in each of the 3 FOVs. This cloud formation is equivalent to the hard cloud case described in Susskind *et al.* (1998).

In this trade study, 200 temperature and water vapor profiles were obtained by applying 8 iterations of either the DRAD, L-M or ML algorithm to the simulated data. At each iteration, the resulting profiles as well the χ^2 errors were recorded. The χ^2 at each iteration was divided by the number of CrIS channels to form "normalized" χ^2 values. These values were then used to establish a simple convergence criterion. The criterion was met if the χ^2 was less than a fixed threshold. Finally, a retrieval rate was calculated based on the number of cases that meet this criterion at each iterative step. The resulting retrieval rates for each of the three algorithms and their average errors are shown in Figure 61 and Figure 62. These plots illustrate that the DRAD and the M-L algorithm have comparable retrieval rates. It also shows that the ML algorithm's performance lags that of the other two. This is most evident in both the clear sky and cloudy land cases. These plots also show that the average χ^2 does not decrease asymptotically for all cases. This indicates that the ML method does not converge for all of the test cases.

Figure 63 through Figure 65 show the root mean square (RMS) errors for the first 4 iterations of DRAD, L-M, and ML algorithms (these results were obtained for the same 200 clear-sky land scenes as above). The DRAD and the L-M algorithms have similar RMS values, but the DRAD method requires 2 iterations to obtain a stable solution, whereas the L-M reaches it after a minimum of 3-4 iterations. In this case, the ML algorithm actually diverges from its minimum water vapor error as the number of iterations increases. This indicates that the ML method tends to overfit the data, which is in part due to the fact that S_e does not represent the errors associated with the forward model (mapping from profile to radiance space).

Similar comparisons have been performed using a first guess based on climatology. These experiments were designed to assess the robustness of the inversion approaches with respect to the quality of the first guess, which is an important consideration in operational environments. The clear-sky cases described above were rerun under these conditions. The resulting retrieval rates and average errors are plotted in Figure 66 and their average temperature and water vapor RMS errors for the first 4 iterations are shown in Figure 67 through Figure 69. These plots illustrate the importance of a good initial guess and demonstrate that the performance of all 3 algorithms is affected by the initial conditions. The L-M and ML algorithms are most affected by the lack of a good initial guess. Under these conditions the ML algorithm has an unacceptable retrieval rate of <50%.

4 Summary

This study shows that the ad-hoc DRAD algorithm has better overall performance than either the Levenberg-Marquardt or the Maximum Likelihood methods. The most noticeable improvement in performance was obtained when the initial guess for each algorithm was constructed based on climatology information rather than on the microwave retrieval. These results illustrate that the performance of the DRAD, L-M and ML is tightly coupled to the initial guess. However, the DRAD method shows superior convergence characteristics when the first guess is far away from the true solution. This is an important consideration in selecting an appropriate inversion technique for an operational algorithm. The DRAD algorithm has the added advantage in that its control parameter α is easy to tune. Numerous trials have shown that varying α between 2 and 10 has only a impact on the retrieval process. The control parameter λ in the L-M algorithm, on the other hand, can have a significant impact on the retrieval process. Assigning λ to a large initial value degrades the convergence rate, whereas setting λ to a small initial value may force the algorithm to spend several iterations searching for the appropriate step size.

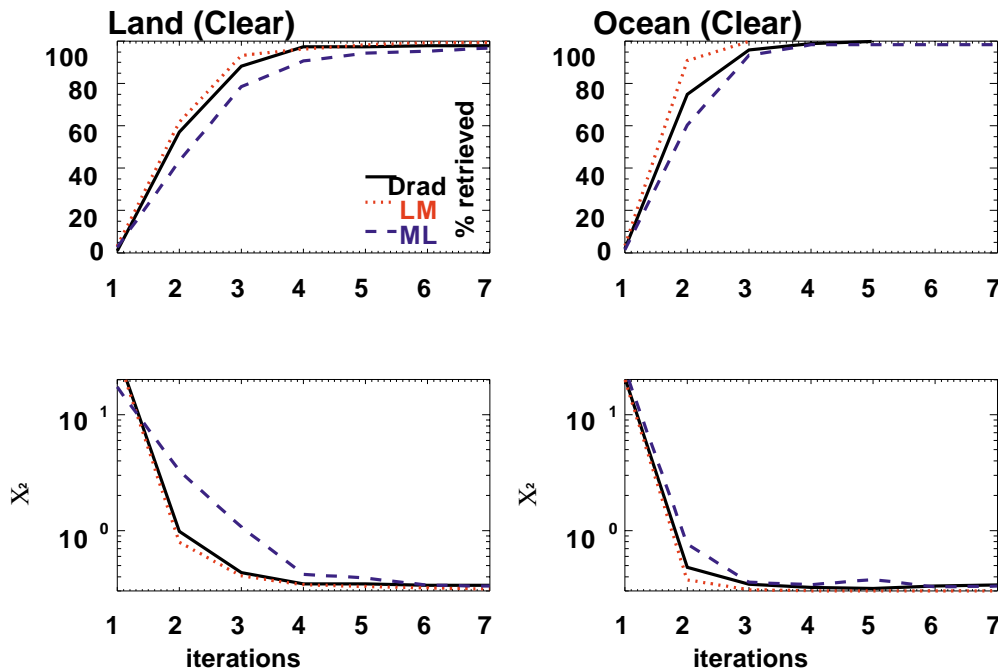


Figure 61: Algorithm retrieval rates and χ^2 values versus iteration number for clear-sky land and ocean cases (microwave first guess). Results obtained using the DRAD, Levenberg-Marquardt, and Maximum Likelihood methods are shown. The upper plots describe the number of retrievals that meet the radiance convergence criterion ($\chi^2 < 2$). The lower plots show average χ^2 values for profiles that converged in 8 iterations.

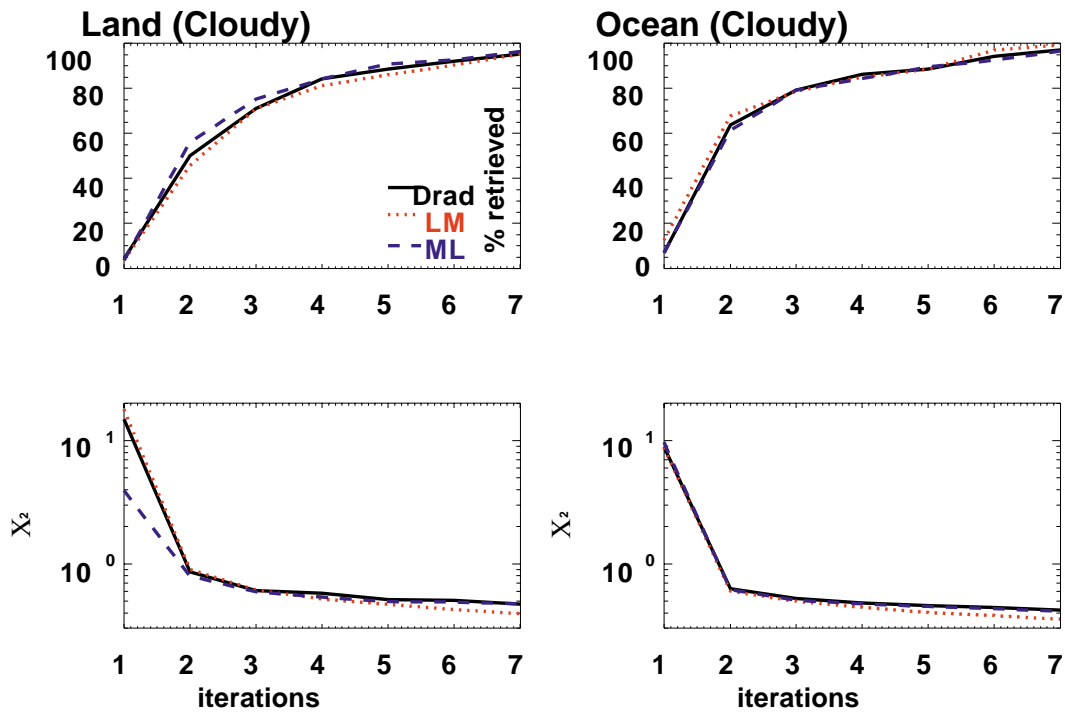


Figure 62: Percent retrieved and normalized χ^2 for cloudy cases corresponding to Figure 61.

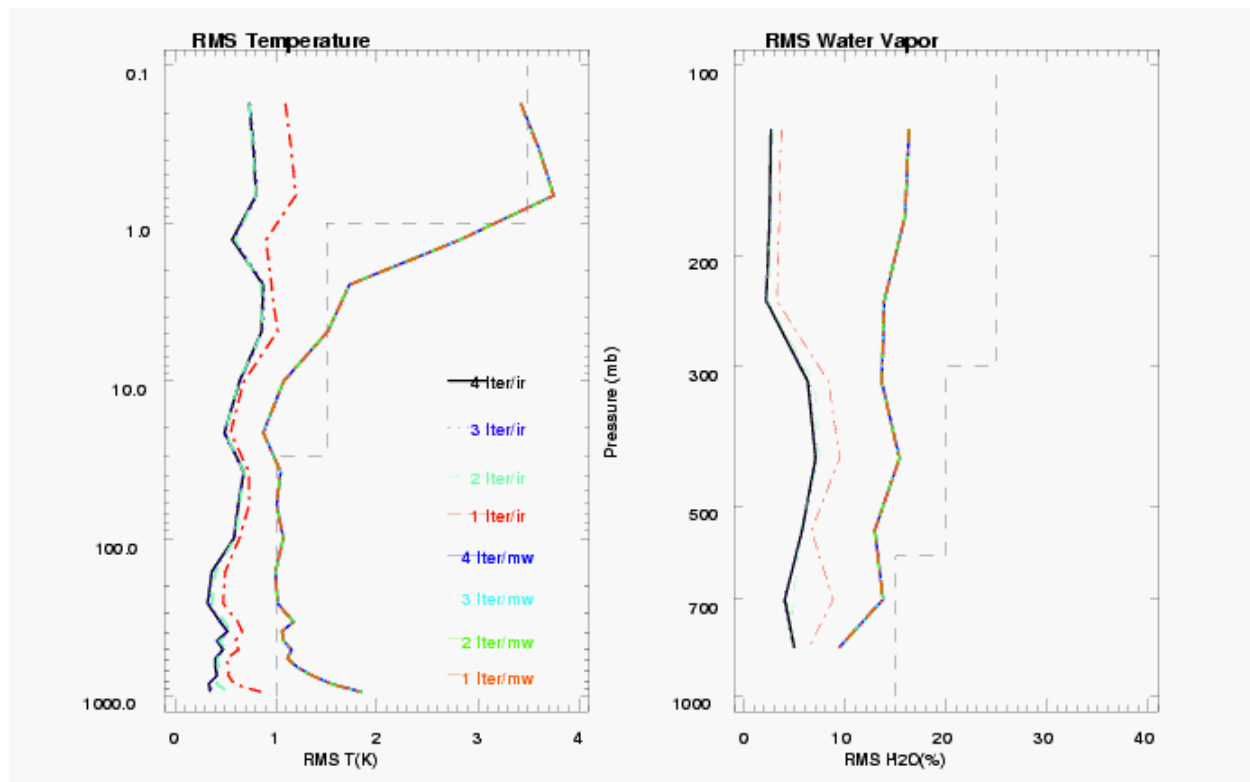


Figure 63: Temperature and water vapor RMS errors for 200 clear-sky land profiles retrieved using the DRAD algorithm.

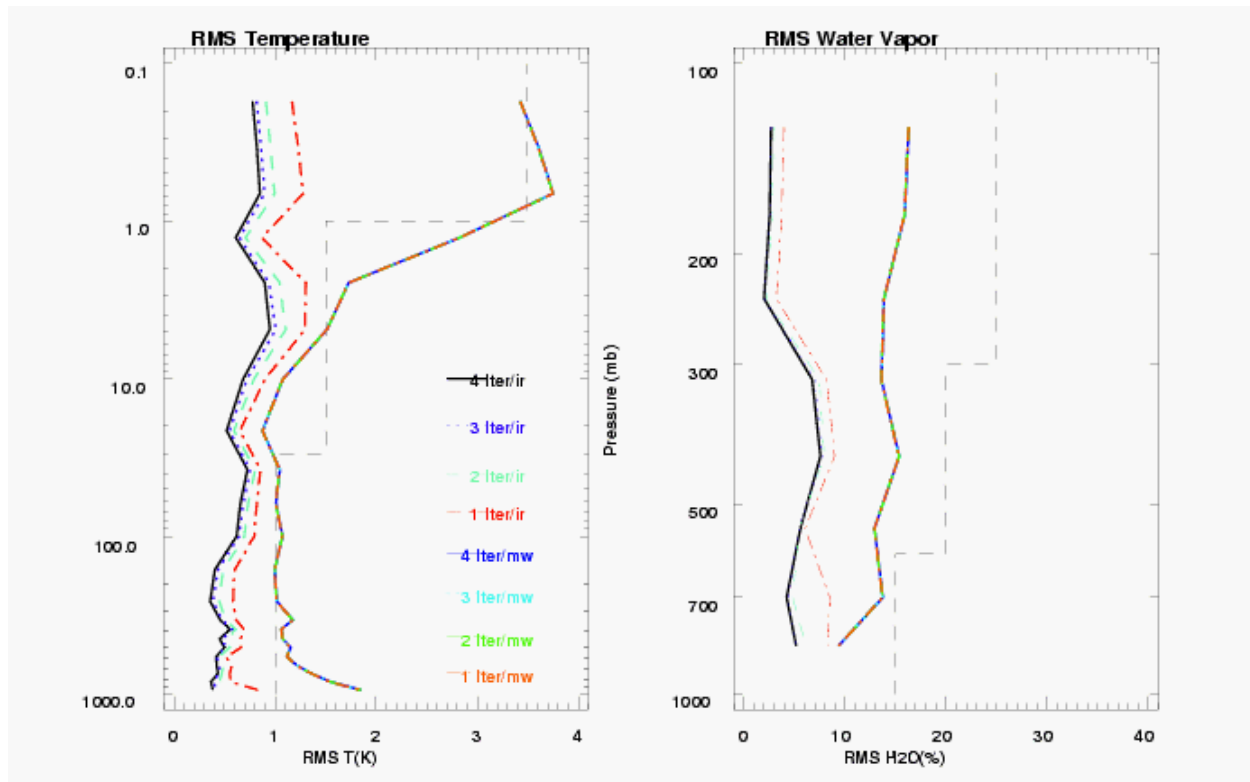


Figure 64: Similar to Figure 63, but for the Levenberg-Marquadt algorithm.

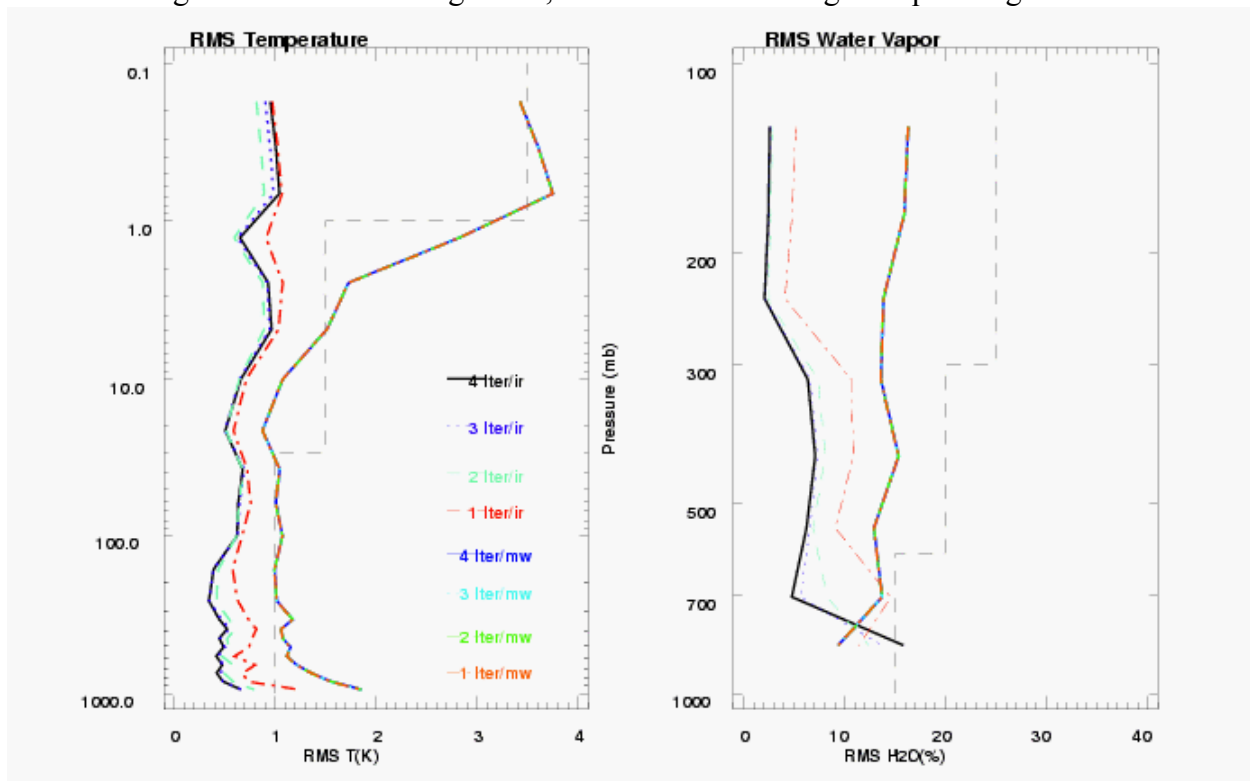


Figure 65: Similar to Figure 63, but for the Maximum Likelihood algorithm.

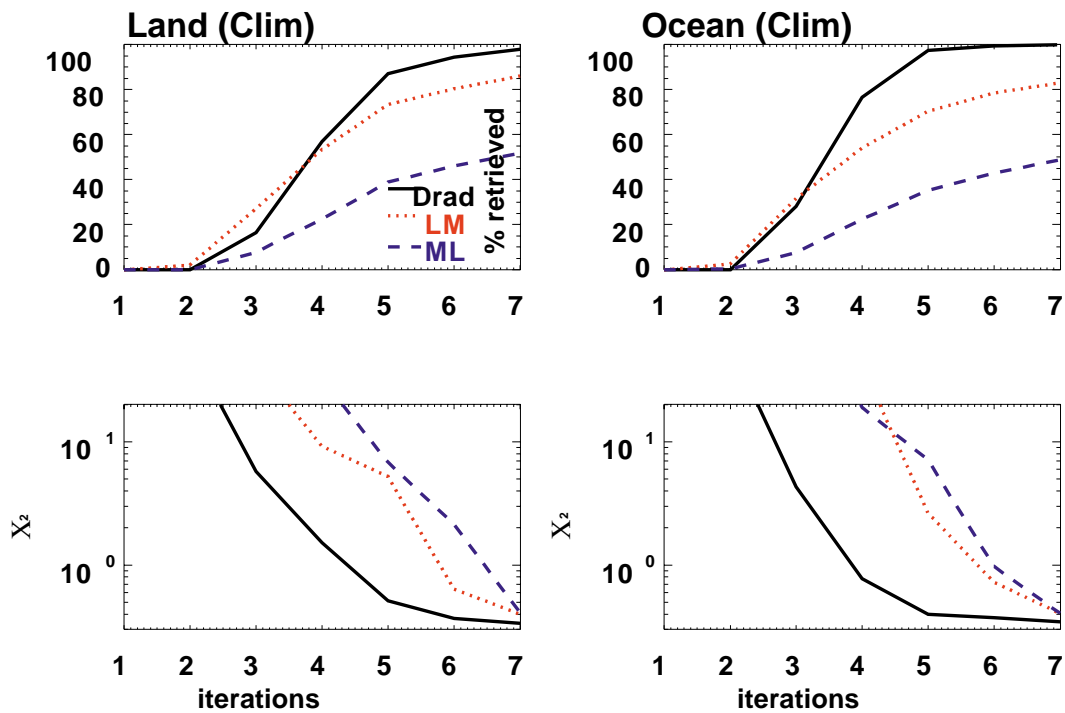


Figure 66: Similar to Figure 61, but for climatology first guess.

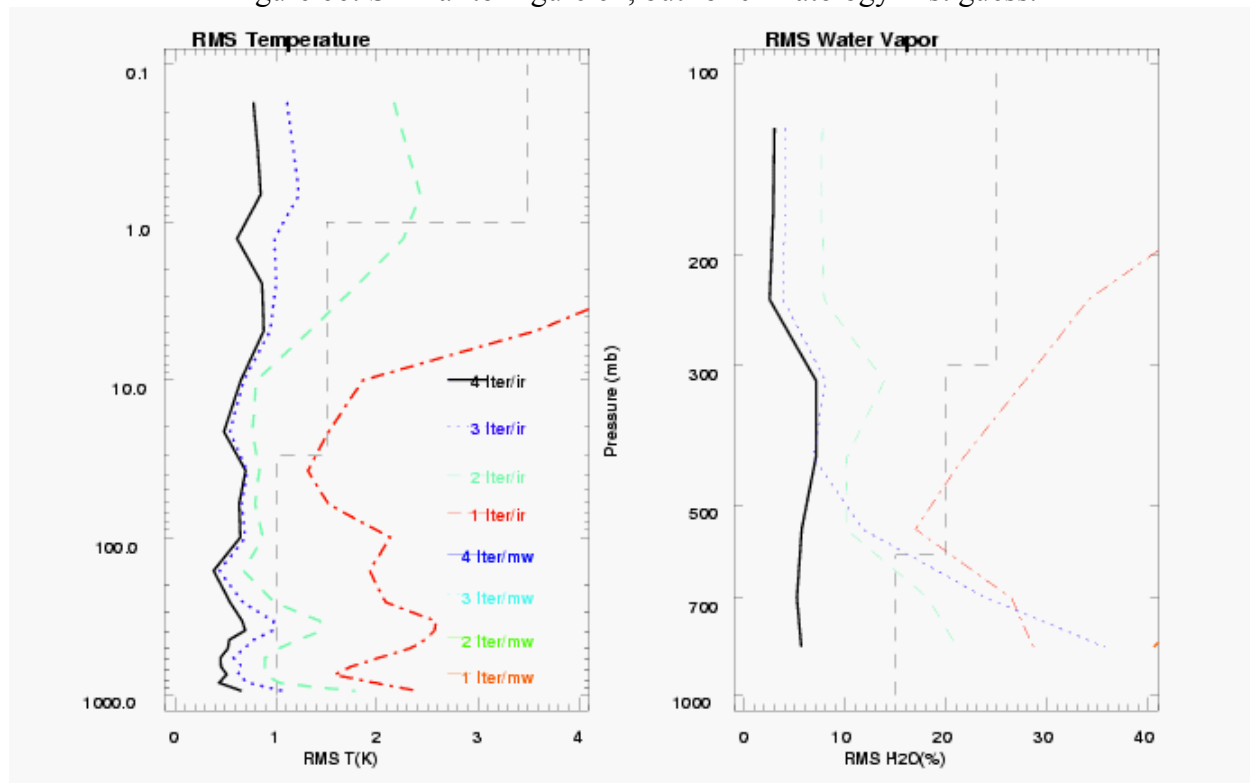


Figure 67: Temperature and water vapor RMS errors for 200 clear-sky land profiles retrieved using the DRAD algorithm and a climatology first guess.

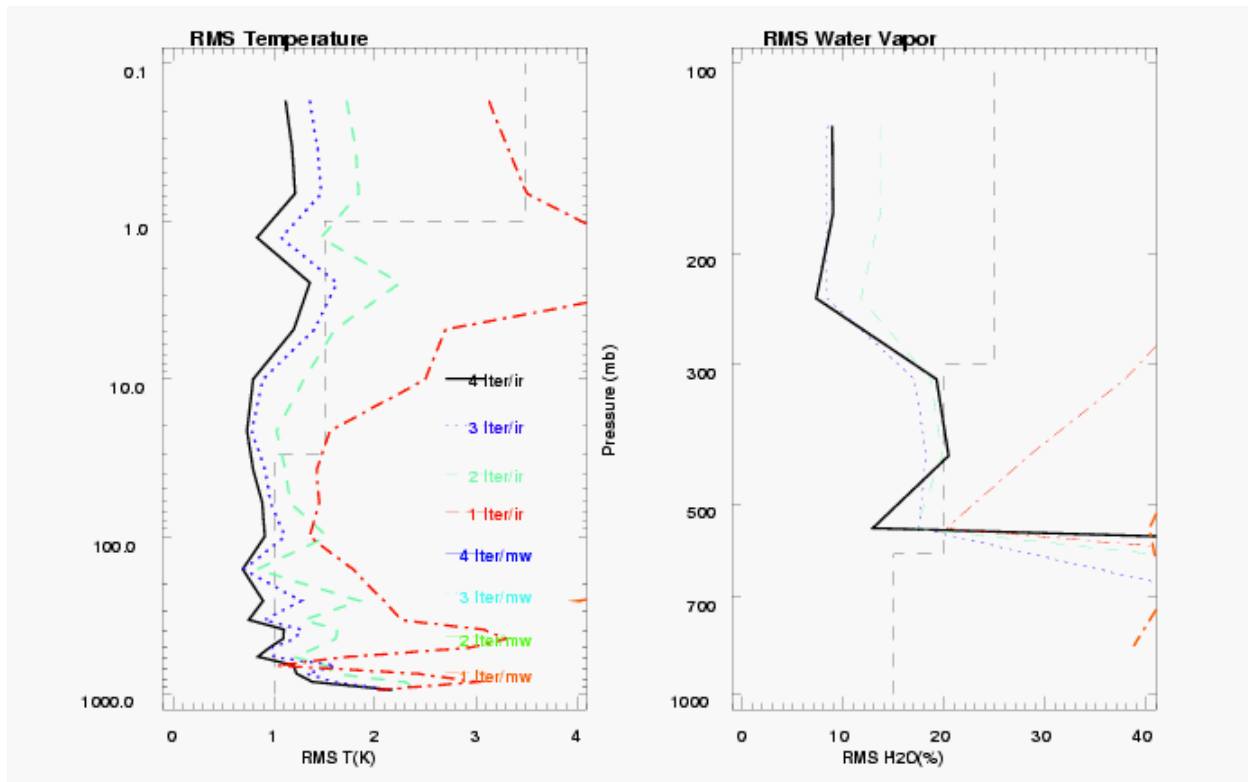


Figure 68: Similar to Figure 67, but for the Levenberg-Marquardt algorithm.

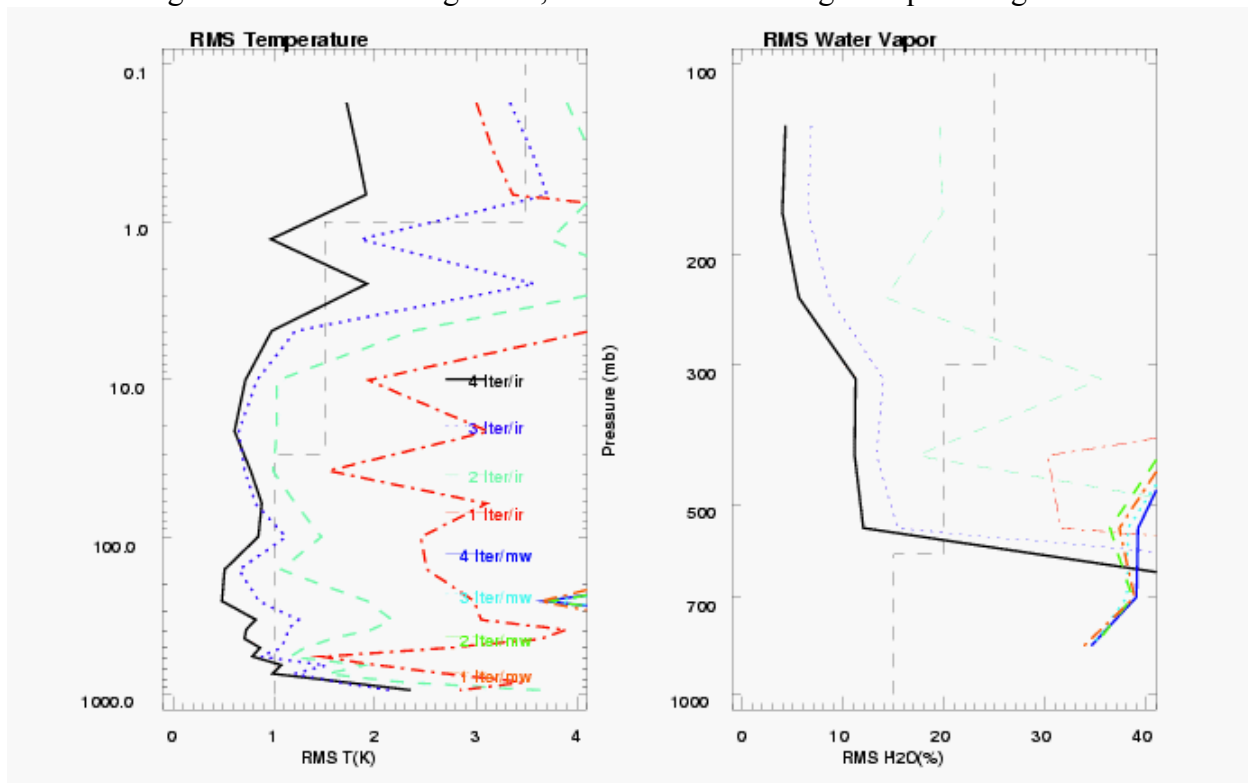


Figure 69: Similar to Figure 67, but for the Maximum Likelihood algorithm.

APPENDIX 6: THE CLOUD CLEARING (CC) METHOD

Adapted from the AIRS ATBD (1999).

“We” in this section designates the AIRS team.

1 Treatment of Radiances in Cloudy Atmospheres

Three basic approaches used for accounting for effects of clouds in satellite remote sensing are:

1) identify clear areas and only perform retrievals in those areas, with no cloud correction needed; 2) use channel observations in adjacent potentially partially cloudy scenes to reconstruct what the channel radiances would have been if the scenes were clear, and use these reconstructed observations to determine geophysical parameters; and 3) determine both surface and atmospheric geophysical parameters, as well as cloud properties, from the radiance observations themselves,

An example of the first approach is given by Cuomo *et al.*(1993).

Eyre (1989a, 1990) has used the third approach in simulation by assuming an unknown pressure, and attempted it with real TOVS data as well (Eyre1989b).

Our approach, like that used in Susskind (1993), is of the second type and is an extension of that used by Smith (1968) and Chahine (1974, 1977). This approach utilizes satellite observed radiances, $\bar{R}_{i,k}$, corresponding to channel i and field-of-view k , made over adjacent fields-of-view. In this approach, there is no need to model the radiative and reflective properties of the clouds. The only assumption made is that the fields-of-view are homogeneous except for the amount of cloud cover in K different cloud formations in each field-of-view. $R_{i,clr}$, the radiance which would be observed if the entire field of view were clear, and $\bar{R}_{i,clr,\ell}$, the radiance which would be observed if the entire field of view were covered by cloud formation ℓ , are therefore assumed to have the same respective values in each field-of-view. If the observed radiances in each field-of-view are different, the differences in the observed radiances are then attributed to the differences in $\alpha_{\ell k}$, the fractional cloudiness for cloud ℓ in field-of-view k .

Using the above assumptions, Chahine (1977) showed that the reconstructed clear-column radiance for channel i , $\hat{R}_{i,clr}$, can be written as a linear combination of the measured radiances in the $K+1$ fields-of-view, $\bar{R}_{i,1} \dots \bar{R}_{i,K+1}$, according to:

$$\hat{R}_{i,clr} = \bar{R}_{i,1} + \eta_1 [\bar{R}_{i,1} - \bar{R}_{i,K+1}] + \dots + \eta_k [\bar{R}_{i,1} - \bar{R}_{i,(K+2)-k}] + \dots + \eta_K [\bar{R}_{i,1} - \bar{R}_{i,2}]$$

Equation 86

where $\eta_1 \dots \eta_K$ are unknown channel-independent constants, and $K+1$ fields-of-view (FOVs) are needed to solve for K cloud formations. The fields-of-view are ordered such that FOV 1 is the clearest field-of-view based on observations in the $11 \mu\text{m}$ window (the field-of-view with the highest $11 \mu\text{m}$ radiances is assumed to be FOV 1) and FOV $K+1$ is the cloudiest. Thus η_1 multiplies the largest radiance differences and η_K the smallest. Once $\eta_1 \dots \eta_K$ are determined, Equation 86 is used to produce the reconstructed clear column radiances for all channels used in the retrieval process. The reconstructed clear column radiances are then used when solving for the geophysical parameters.

Susskind *et al.* (1984), Susskind and Reuter (1985a) and Chahine and Susskind (1989) have successfully used this approach with two fields-of-view, assuming one cloud formation, in the analysis of HIRS2/MSU operational sounding data. Chahine and Susskind (1989) show that retrieval accuracy, verified by co-located radiosondes, does not degrade appreciably with increasing cloud cover, for retrieved cloud fractions of up to 80%. An analogous assumption is made by NOAA/NESDIS in production of their clear column radiances used in generation of operational HIRS2/MSU retrievals (McMillin and Dean 1982). Susskind and Reuter (1985b) have performed simulations with two cloud formations and three fields-of-view for the AMTS instrument, an earlier version of AIRS (Chahine *et al.* 1984), used in conjunction with MSU.

We (AIRS TEAM) have developed a new methodology to account for multiple cloud formations using the AIRS and AMSU instruments. The methodology to determine η_k is first presented for a single cloud formation and then generalized for use with multiple cloud formations.

2 Single Cloud Formation with 2 FOVs

For one cloud formation and two fields-of-view, the reconstructed clear-column radiance for channel i from Equation 86 is given by:

$$\hat{R}_{i,clr} = \bar{R}_{i,1} + \eta_1 [\bar{R}_{i,1} - \bar{R}_{i,2}]$$

Equation 87

Given the assumptions mentioned above, the value of η_1 is independent of cloud spectral properties and has the same value for all channels. η_1 can be written in terms of α_1 and α_2 and has a unique value given by :

$$\eta_1 = \frac{\alpha_1}{\alpha_2 - \alpha_1}$$

Equation 88

where α_1 and α_2 are the cloud fractions in each field-of-view (Chahine 1974). It is not necessary to know α_1 or α_2 to determine η_1 . The determination of η is sequential and is done in a number of passes based on the latest estimate of the surface and atmospheric parameters. An expected value of $R_{i,clr}$ for any channel can be used to estimate η according to:

$$\eta_{i,1}^n = \frac{R_{i,clr}^n - \bar{R}_{i,1}}{\bar{R}_{i,1} - \bar{R}_{i,2}}$$

Equation 89

where $\eta_{i,1}^n$ is the n^{th} pass estimate of η , obtained from channel i, based on the n^{th} pass estimate of the clear column radiance $R_{i,clr}^n$. $R_{i,clr}^n$ is obtained by using the radiative transfer equation to compute the channel i radiance with the n^{th} pass estimates of atmospheric and surface parameters. The general multi-pass procedure referred to by n will be discussed later.

If the estimate of temperature profile is too warm (cold) over coarse layers of the atmosphere, the estimated clear column radiances $R_{i,clr}^n$ will be too high (low), and $\eta_{i,1}^n$ will be too large (small).

In performing HIRS2/MSU retrievals, Susskind *et al.* (1984) correct potential biases in n^{th} iterative coarse layer temperatures by adjusting computed brightness temperatures for the IR channels used to estimate η according to the difference between the observed brightness temperature for an MSU channel sensitive to mid-lower tropospheric temperatures and that computed from the n^{th} iterative temperature profile. This in effect adjusts the n^{th} iterative temperature profile to be consistent with the observations in a single MSU channel. We can utilize the superior sounding capability of AMSU, compared with MSU, to first produce an AMSU only retrieval of atmospheric temperature-moisture profile for use as the initial guess to start the retrieval process, and use in the first pass estimation of η_i . The AMSU retrieval can be done before the cloud correction because AMSU radiances are not significantly affected by non-precipitating clouds. The temperature retrieval obtained from AMSU will have the property that radiances computed from it agree well with all AMSU channels and should not be very biased over coarse layers of the atmosphere, though local errors will still exist. Alternatively, we can use the regression guess of NOAA's physical retrieval or the NOAA first product retrieval itself for this purpose. These profiles will also be unbiased, as long as the NOAA cloud clearing step, described in Section 4.2 (of the AIRS ATBD), is sufficiently accurate.

Using different IR channels in Equation 89 will result in different estimated values of $\eta_{i,1}$ as a result of a combination of local errors in the temperature profile, and channel noise effects. Many channels can be used to estimate η_i in order to reduce potential errors. For the case of a single cloud formation, this can be accomplished by simply taking a weighted average of $\eta_{i,1}$ over a set of cloud filtering channels to get a single value of η_i (Susskind and Reuter 1985a, Susskind *et al.* 1993). Once a value of η_i is computed, the clear-column radiances for all channels can be reconstructed using Equation 87. If the denominator in Equation 89 is small, errors in estimating the numerator will be amplified in the determination of η . Therefore, it is important that cloud filtering channels have a large contrast in radiance between the two fields-of-view. This implies the channels should be sensitive to the presence of clouds. The contrast can be further enhanced by averaging together observations in the warmest spots and averaging observations in the coldest spots within a scene to produce two high contrast fields-of-view (Reuter *et al.*, 1988). Averaging spots also reduces the effects of instrumental noise. The methodology for selecting and weighting channels used to determine η is described in the next section.

3 Channel Selection for Cloud Filtering

Chahine (1974) showed that 15 μm channels are preferable for use in the determination of η compared to 4.3 μm channels, because the error in $\hat{R}_{i,clr}$, caused by an error in the estimated temperature profile, will result in a smaller error in η as determined from Equation 89. This analysis is a result of the properties of the blackbody function in the two spectral regions. Moreover, Chahine (1974) and Halem *et al.* (1978) show that if one has infra-red observations in both the 15 μm and 4.3 μm temperature sounding bands, but no microwave observations, soundings can be done in cloudy conditions if η is determined using observations in 15 μm channels and the temperature sounding channels for the mid-lower troposphere come from the 4.3 μm region.

Along the lines of Chahine (1974), we (AIRS TEAM) initially selected channels in the 15 μm band that sound the mid-lower troposphere for cloud filtering. These channels were selected to be between absorption lines so as to produce sharp weighting functions that would have less of an upper tropospheric and stratospheric contribution in order to maximize sensitivity to the clouds. We also avoided channels contaminated by water vapor and ozone absorption, that could cause errors in $R_{i,clr}$. This same channel selection methodology was used by Susskind *et al.* (1993).

Using only 15 μm channels for cloud filtering ignores the effects of solar radiation reflected off the clouds. When sunlight is reflected off the surface and clouds, the scene can exhibit more contrast in the 4.3 μm region, especially for low clouds. In addition, cloud effects on radiances can be of opposite sign at short wavelengths than at long wavelengths. This change in sign makes it easier to distinguish cloud effects on the radiances from thermal effects of the clear atmosphere. Therefore, it is desirable to 4.3 μm channels in the cloud filtering set during the day. We feel that it is desirable to use the same methodology for both cloud filtering and retrieval of geophysical parameters during the day and night. We therefore use both 15 μm and 4.3 μm channels in the channel set used to estimate η . The 15 μm and 4.3 μm cloud filtering channels are a subset of the channels used to determine the atmospheric temperature profile.

Window channels are more sensitive to clouds than atmospheric sounding channels, but are also more sensitive to uncertainties in surface parameters. We have developed improved methodology to include window channels in the determination of η , with a weight that properly reflects the uncertainty in their clear column radiances. An analogous weighting procedure is done for all channels. The relative weighting of the 15 μm and 4.3 μm channels in the determination of η is done objectively and will differ under daytime and nighttime conditions as described error!later.

4 Determination of η for a Single Cloud Formation

The method we use to determine η is analogous to that used by Susskind *et al.* (1993), who sets:

$$\eta = \frac{\sum_i W_i^2 \eta_i}{\sum_i W_i^2}$$

Equation 90

where W_i is a weight for channel i . An appropriate value of W_i should take into account propagated errors in η_i resulting from instrumental and computational noise. For example, channels more sensitive to clouds, with large values of $|\bar{R}_{i,1} - \bar{R}_{i,2}|$, should receive larger weight.

One can write Equation 89 in the form of I equations, one for each channel i , in matrix form:

$$W (R_{clr}^n - \bar{R}_1) = W (\bar{R}_1 - \bar{R}_2) \eta^n$$

Equation 91

where W is an $I \times I$ diagonal weight matrix with weight W_{ii} for channel i , $(R_{clr}^n - \bar{R}_1)$ and $(\bar{R}_1 - \bar{R}_2)$ are $I \times 1$ vectors, and η^n is the unknown. The standard weighted least squares solution to this matrix problem is given by:

$$\eta^n = \left[(\bar{R}_1 - \bar{R}_2)' W' W (\bar{R}_1 - \bar{R}_2) \right]^{-1} (\bar{R}_1 - \bar{R}_2)' W' W (R_{clr}^n - \bar{R}_1)$$

Equation 92

and reduced to:

$$\eta^n = \frac{\sum_i W_i^2 (\bar{R}_{i,1} - \bar{R}_{i,2}) (R_{clr,i}^n - R_{i,1})}{\sum_i W_i^2 (\bar{R}_{i,1} - \bar{R}_{i,2})^2} = \frac{\sum_i W_i^2 (\bar{R}_{i,1} - \bar{R}_{i,2})^2 \eta_i^n}{\sum_i W_i^2 (\bar{R}_{i,1} - \bar{R}_{i,2})^2}$$

Equation 93

where η_i^n is given by Equation 89. Equation 93 is analogous to Equation 90, but in Equation 93, the contribution of the difference of radiances in the two fields-of-view to the channel weight is explicitly taken into account. Therefore W_i in this context represents any residual weight factors we may want to add, such as effects of channel noise. Susskind *et al.* (1993) used Equation 91, including in W_i the term $[\bar{\Theta}_{i,1} - \bar{\Theta}_{i,2}]^2$, that is roughly proportional to $[R_{i,1} - R_{i,2}]^2$ for the 15 μm channels they used.

The above discussion is accurate as long as sources of channel noise are uncorrelated from channel to channel. Under these conditions, an appropriate value of W_i should be inversely proportional to sources of noise. There are two sources of noise in Equation 91, instrumental noise and computational noise. Instrumental noise is random and affects $\bar{R}_{i,1}$ and $\bar{R}_{i,2}$. Computational noise affects $R_{i,clr}^n$ and will be correlated from channel to channel. In the case of channel correlated noise, the appropriate equation is given by:

$$\eta^n = \left[(\bar{R}_1 - \bar{R}_2)' N^{-1} (\bar{R}_1 - \bar{R}_2) \right]^{-1} (\bar{R}_1 - \bar{R}_2)' N^{-1} (R_{clr}^n - \bar{R}_1)$$

Equation 94

where N is the channel noise covariance matrix, indicating errors in $(R_{clr}^n - \bar{R}_1)$.

The iterative methodology to determine clear column radiances consists of three passes to determine η^n (n=1,2,3), using three sets of conditions, to give $R_{i,clr}^n$, in which $R_{i,clr}^n$ and hence η^n become increasingly more accurate in each iteration. Each pass has its own N^d , reflecting

expected errors in $R_{i,clr}^n - R_{i,1}$. In the current CrIS code, the noise covariance matrix is assumed to be diagonal and its elements have the form

$$N_{ii}^n = NE\Delta N_i^2 + \left[\frac{\partial R_i}{\partial T_s} \Delta T_s^n \right]^2 + \left[\frac{\partial R_i}{\partial \epsilon_i} \Delta \epsilon_i^n \right]^2 + \left[\frac{\partial R_i}{\partial p_i} \Delta p_i^n \right]^2 + \left[\frac{\partial R_i}{\partial T(p)} \Delta T(p)^n \right]^2 + \left[\frac{\partial R_i}{\partial \ln q(p)} \Delta \ln q(p)^n \right]^2$$

Equation 95

where $NE\Delta N_i$ is the instrumental noise variance for channel i and the remaining terms are contributions to errors in the computed value of $R_{i,clr}^n$ resulting from errors in estimated parameters. Utilizing the OSS formulation of the forward model, the partial derivatives are computed analytically and the uncertainties (such as ΔT_s^n) are specified so as to be indicative of the expected errors for that parameter in each pass.

Channels that do not see the clouds appreciably for a given scene are not included in the determination of η . Currently, channel i is considered not to be sensitive to clouds if $|\bar{R}_{i,1} - \bar{R}_{i,2}| \leq 3\sqrt{2} NE\Delta N_i$. In situations where there are not at least 2 useful cloud filtering channels, both fields-of-view are assumed to be clear and $\eta = -1/2$. This has the effect of setting the clear column channel radiances to the average of the observed radiances in both fields-of-view. The other possibility for very little contrast is that both scenes have essentially identical, but non-zero, cloud cover, such as full overcast. In this case, assuming both FOVs to be clear will result in a mismatch between the microwave retrievals (which unaffected by clouds) and the IR retrievals (which are cloud contaminated) and the profile will be rejected during quality control (see Section 13.2). The constant cloud cover case can also be detected and rejected by comparing R_{clr}^n with \bar{R}_1 , e.g., simulations show that cloudy low contrast scenes can be identified and rejected if:

$$\sqrt{\sum_{i=1}^I \frac{(R_{i,clr}^n - \bar{R}_{i,1})^2}{N_{ii}}} > 1.5$$

Equation 96

5 Multiple Cloud Formations with Multiple FOVs

In order to solve for K cloud formations with unknowns $\eta_1 \dots \eta_K$, K+1 fields-of-view are needed. A simple relationship between α_k and η_i does not exist for the case of multiple cloud formations, nor is the solution $\eta_1 \dots \eta_K$ necessarily unique. For example, consider a case of only one cloud formation with cloud fractions of 20%, 40%, and 60% in fields-of-view 1-3 respectively; $\eta_1^{(1)} = 1$, $\eta_1^{(2)} = 0$ and $\eta_1^{(3)} = 0$, $\eta_2^{(2)} = .5$ are two examples of solutions to the problem, as are appropriate linear combinations of these solutions, given by:

$$\begin{pmatrix} \eta_1 \\ \eta_2 \end{pmatrix} = (1-f) \begin{pmatrix} \eta_1^{(1)} \\ \eta_2^{(1)} \end{pmatrix} + f \begin{pmatrix} \eta_1^{(2)} \\ \eta_2^{(2)} \end{pmatrix}$$

Equation 97

The optimal solution should provide the correct clear column radiances and do so with the smallest values of η in order to minimize amplification of instrumental noise when used in Equation 86.

Determining an optimal set of η_k is analogous to the determination for a single cloud formation. Using a set of I channels to estimate K values of η , Equation 86 may be expressed as a set of linear equations in matrix form according to

$$\begin{pmatrix} R_{1,clr}^n - \bar{R}_{1,1} \\ R_{2,clr}^n - \bar{R}_{2,1} \\ \vdots \\ R_{I,clr}^n - \bar{R}_{I,1} \end{pmatrix} = \begin{pmatrix} \bar{R}_{1,1} - \bar{R}_{1,K+1} & \bar{R}_{1,1} - \bar{R}_{1,K} & \cdots & \bar{R}_{1,1} - \bar{R}_{1,2} \\ \bar{R}_{2,1} - \bar{R}_{2,K+1} & \bar{R}_{2,1} - \bar{R}_{2,K} & \cdots & \bar{R}_{2,1} - \bar{R}_{2,2} \\ \vdots & \vdots & \ddots & \vdots \\ \bar{R}_{I,1} - \bar{R}_{I,K+1} & \bar{R}_{I,1} - \bar{R}_{I,K} & \cdots & \bar{R}_{I,1} - \bar{R}_{I,2} \end{pmatrix} \begin{pmatrix} \eta_1^n \\ \eta_2^n \\ \vdots \\ \eta_K^n \end{pmatrix}$$

Equation 98

or

$$C^n = D\eta^n$$

Equation 99

The solution to Equation 99 is given by:

$$\eta^n = (D' N^{-1} D)^{-1} D' N^{-1} C^n$$

Equation 100

where N is the channel noise covariance matrix as given in Equation 95. Given η^n , $\hat{R}_{i,clr}^n$ is constructed for all channels according to Equation 86. $\hat{R}_{i,clr}^n$ are used as the observations in the general retrieval process. If the observation in a channel is not sensitive to the presence of clouds in the field of view, it is better to average the observations in all fields of view as:

$$\hat{R}_{i,clr} = \frac{1}{K+1} \sum_{k=1}^{K+1} \bar{R}_{i,k}$$

Equation 101

This is equivalent to defining separate values of η for channels that do not see clouds as $\eta_{i,clr}^n = -1/(K+1)$, and using them to produce $\hat{R}_{i,clr}^n$ for the appropriate channels. Currently, channel i is considered not to be sensitive to clouds if $|R_{i,1} - R_{i,k+1}| \leq 3\sqrt{2} NE\Delta N_i$ and it is included in a set of channels expected not to see clouds given the retrieved cloud height.

REFERENCES

- Anderson, G.P., Clough, S.A., Kneizys, F.X., Chetwynd, J.H., and Shettle, E.P., AFGL atmospheric constituent profiles (0-120 km), *Tech. Rep. AFGL-TR-86-0110, Phillips Lab., Hanscom Air Force Base, Massachusetts*, 1986.
- Chahine, M.T., Remote sounding cloudy atmospheres. I. The Single Cloud Layer, *J. Atmos. Sci.*, **31**, 233-243, 1974.
- Chahine, M.T., Remote sounding cloudy atmospheres. II. Multiple Cloud Formations, *J. Atmos. Sci.*, **34**, 744-757, 1977.
- Chahine, M.T., Evans N.L., Gilbert V., and Haskins R., Requirements for a passive IR advanced moisture and temperature sounder, *Appl. Opts.*, **23**, 979-989, 1984.
- Chahine, M. T. and Susskind J., Fundamentals of the GLA physical retrieval method, *Report on the Joint ECMWF/EUMETSAT Workshop on the Use of Satellite Data in Operational Weather Prediction: 1989-1993*, **Vol. 1**, 271-300, T. Hollingsworth Editor, 1989.
- Chedin, A., Scott N.A., Wahiche C., and Moulinier P., The Improved Initialisation Inversion (3I) method: A high resolution physical method for temperature retrievals from the TIROS-N series, *J. Clim. Appl. Meteor.*, **24**, 128-143, 1985.
- Clough, S.A., Kneizys, F.X., and Davies, R.W., Line shape and the water vapor continuum, *Atmos. Res.*, **23**, 229-241, 1989.
- Clough, S.A., Iacono, M.J., and Moncet, J.-L., Line-by-line calculation of atmospheric fluxes and cooling rates: Application to water vapor, *J. Geophys. Res.*, **97**, 15761-15785, 1992.
- Clough, S. A., C. P. Rinsland, and P. D. Brown, Retrieval of tropospheric ozone from simulations of nadir spectral radiances as observed from space. *J. Geophys. Res.*, **100**, 16579-16593, 1995.
- Cuomo, V., Rizzi, R., and Serio, C., An objective and optimal estimation approach to cloud-clearing for infrared sounder measurements, *Int. J. of Rem. Sensing*, **14**, 729-743, 1993.
- Devenyi, D. and T. W. Schlatter, Statistical properties of three-hour prediction « errors » derived from the Mesoscale Analysis and Prediction System. *Mon. Wea. Rev.*, **122**, 1263-1280, 1994.
- Eyre, J.R., Inversion of cloudy satellite sounding radiances by nonlinear optimal estimation: Theory and simulations for TOVS and application to TOVS data, *Quart. J. Roy. Meteor. Soc.*, **115**, 1001-1037, 1989a.
- Eyre, J. R., Inversion of cloudy satellite sounding radiances by nonlinear optimal estimation. II: Application to TOVS data. *Q. J. R. Meteorol. Soc.*, **115**, 1027-1037, 1989b.

REFERENCES

- Eyre, J. R., The information content of data from satellite sounding systems: A simulation study, *Q. J. R. Meteorol. Soc.*, **116**, 401-434, 1990.
- Goerss, J. S. and P. A. Phoebus, The multivariate optimum interpolation analysis at the Fleet Numerical Oceanography Center. FR 7531-92-9413, Navy Research Laboratory, Monterey, CA, 1993.
- Grody, N.C., Surface identification using satellite microwave radiometers, *IEEE Trans. Geosci. and Remote Sensing*, **26**, 850-859, 1988.
- Halem, M., Ghil, M., Atlas, R., Susskind, J., Quirk, W , The GISS sounding temperature impact test, *NASA Tech. Memo. 78063*: 2.9-2.82, 1978.
- Hamilton, K., R. J. Wilson, J. D. Mahlman, and L. J. Umscheid, 1995: Climatology of the SKYHI troposphere-stratosphere-mesosphere general circulation model. *J. Atmos. Sci.*, **52**, 5-43.
- Lachance, R., *et al.*, Algorithm Theoretical Basis Document (ATBD) for the Cross-Track Infrared Sounder (CrIS), Volume I, Sensor Data Records (SDR), BOMEM / ITT Document, 1999.
- Levenberg, K., A method for the solution of certain problems in least squares, *Q. Appl. Math.*, **2**, 164-168, 1944.
- Liebe, H.J., Hufford, G.A., and Manabe, T., A model for the complex permittivity of water at frequencies below 1 THz. *Intern. J. Infrared Millimeter Waves*, **12**, 659-675, 1991.
- McMillin, L. M. and Dean, C. A., Evaluation of a New Operational Technique for producing clear radiances, *J. Appl. Meteo.*, **21**, 1005-1014, 1982.
- Marquardt, D., An algorithm for least squares estimation of nonlinear parameters, *SIAM J. Appl. Math.*, **11**, 431-441, 1963.
- Miller, S.M., Snell, H.E., and Moncet, J.-L., Simultaneous retrievals of middle atmospheric temperature and trace gas species volume mixing ratios from Cryogenic Infrared Radiance Instrumentation for Shuttle (CIRRIS 1A), *J. Geophys. Res.*, **104**, 18697-18714, 1999.
- Press, W.H., Teukolsky, S.A., Vetterling, W.T., Flannery, B.P., Numerical Recipes in C : The Art of Scientific Computing, *Cambridge University Press, Cambridge*, 681-689, 1992.
- Prigent, C., Rossow, W.B., and Matthews, E., Microwave land emissivities estimated from SSM/I observations, *J. Geophys. Res.*, **102**, 21867-21890, 1997.
- Reuter, D., Susskind J., and Pursch A., First guess dependence of a physically based set of temperature-humidity retrievals from HIRS2/MSU data, *J. Atmos. Ocean. Tech.*, **5**, 70-83, 1988.
- Rizzi, R., Serio, C., Kelly , G., Tramutoly, V., McNally, A., Cuomo, V., Cloud Clearing of Infrared Sounder Radiances, *Journal of Applied Meteorology*, **33**, 179-194, 1994.

REFERENCES

- Rodgers, C.D., Retrieval of atmospheric temperature and composition from remote measurements of thermal radiation, *Rev. Geophys.*, **14**, 609–624, 1976.
- Rodgers, C. D., Information Content and Optimization of High-Spectral-Resolution Measurements, *Proc. SPIE*, **Vol. 2830**, 136-147, 1996.
- Rosenkranz, P.W., A Rapid Atmospheric Transmittance Algorithm for Microwave Sounding Channels, *IEEE Trans. on Geo. and Remote Sensing*, **33(5)**, 1135-1140, 1995.
- Smith, W. L., An improved method for calculating tropospheric temperature and moisture from satellite radiometer measurements. *Mon. Wea. Rev.*, **96**, 387-396, 1968.
- Smith, W. L., H. L. Huang, and J. A. Jenney, An advanced sounder cloud contamination study. *J. Appl. Met.*, **35**, 1249-1255, 1996.
- Snell, H.E. *et al.*, OMPS ATBD, 1999.
- Snell, H.E., Anderson, G.P., Wang, J., Moncet, J.-L., Chetwynd, J.H. and English, S.J., Validation of FASE (FASCODE for the Environment) and MODTRAN3: Updates and Comparisons with Clear-Sky Measurements, in Passive Infrared Remote Sensing of Clouds and the Atmosphere III, *Proc. SPIE* 2578, pp 194-204, David K. Lynch and Eric P. Shettle Editors, 1995.
- Snyder, W.C., Wan, Z., Zhang Y., and Feng Y.-Z., Classification-based emissivity for land surface temperature measurement from space, *Int. J. Remote Sensing*, **19**, 2753-2774, 1998.
- Susskind, J., Rosenfield, J., Reuter, D., Chahine, M.T., Remote sensing of weather and climate parameters from HIRS2/MSU on TIROS-N, *J. Geophys. Res.*, **89**, 4677-4697, 1984.
- Susskind, J. and Reuter D., Retrieval of sea-surface temperatures from HIRS2/MSU, *J. Geophys. Res.*, **90C**, 11602-11608, 1985a.
- Susskind, J., Reuter, D., Intercomparison of physical and statistical retrievals from simulated HIRS2 and AMTS data. In: Deepak A., Fleming H. E., Chahine, M. T. (eds) Advances in remote sensing retrieval methods. A Deepak, Hampton VA, 641-661, 1985b.
- Susskind, J., Water vapor and temperature. *Atlas of Satellite Observations Related to Global Change*. Edited by R. J. Gurney, J. L. Foster, and C. L. Parkinson. Cambridge University Press, Cambridge, England, 89-128, 1993.
- Susskind, J., Barnet, C., Goldberg, M., Final Report to the Integrated Program Office on the Interferometer Thermal Sounder Study: Part II Comparative Performance of Interferometers/AIRS, 1998.
- Wilheit, T.T., The effect of winds on the microwave emission from the ocean's surface at 37 GHz, *J. Geophys. Res.*, **84**, 4921-4926, 1979.

REFERENCES

Wiscombe, J.W. and Evans, J. W., Exponential Sum Fitting of Radiative Transmission Functions, *Journal of Computational Physics*, **24**, 416-444, 1977.

LIST OF ACRONYMS

AER	Atmospheric and Environment Research
AERI	Atmospheric Emitted Radiance Interferometer
AIRS	Advanced Infrared Sounder
AMSU	Advanced Microwave Sounding Unit
ASTER	Advanced Spaceborne Thermal Emission and Reflection Radiometer
ATBD	Algorithm Theoretical Basis Document
BRDF	Bi-directional Reflectance Distribution Function
CC	Cloud Clearing
CMIS	Conical Microwave Imaging Sounder
CrIMSS	Cross Track Infrared and Microwave Sounder Suite
CrIS	Cross Track Infrared Sounder
DEM	Digital Elevation Map
EDR	Environmental Data Record
EOF	Empirical Orthogonal Function
ESFT	Exponential Sum Fitting Technique
FOR	Field Of Regard
FOV	Field Of View
FWHM	Full Width at Half Maximum
HH	Hole Hunting
HIRS	High-Resolution Infrared Sounder
HIS	High-resolution Interferometric Spectrometer
HSB	Humidity Sounder Brazil
ILS	Instrument Line Shape
IPO	Integrated Program Office
IR	Infrared
LA	Lower Atmosphere
LBL	Line By Line
LBLRTM	Line By Line Radiative Transfer Model
LOS	Line Of Sight
L-M	Levenberg-Marquardt
LWIR	Longwave IR band
MC	Monte Carlo
MHS	Microwave Humidity Sounder
ML	Maximum Likelihood
MPD	Optical Path Difference
MSU	Microwave Sounding Unit
MW	Microwave
MWIR	Midwave IR band
NASA	National Aeronautics and Space Administration
NAST	NPOESS Atmospheric Sounder Testbed
NDVI	Normalized Difference Vegetation Index
NEDN	Noise Equivalent Difference
NESDIS	National Environmental Satellite, Data, and Information Service
NOAA	National Oceanic and Atmospheric Administration

LIST OF ACRONYMS

NPOESS	National Polar-orbiting Operational Environmental satellite System
NWP	Numerical Weather Prediction
OSS	Optimal Spectral Sampling
PCA	Principal Component Analysis
PDR	Preliminary Design Review
QC	Quality Control
RMS	Root Mean Square
RT	Radiative Transfer
RTE	Radiative Transfer Equation
SCPR	Simultaneous Cloud Parameter Retrieval
SDR	Sensor Data Record
SGI	Silicon Graphics, Inc.
SRD	Sensor Requirement Document
SRF	Sensor Response Function
SSM/I	Special Sensor Microwave/Imager
SSSR	System Sub-System Review
SST	Sea Surface Temperature
SWIR	Shortwave IR band
TIGR	TOVS Initial Guess Retrieval
TOA	Top Of Atmosphere
TOVS	TIROS-N Operational Vertical Sounder
UA	Upper Atmosphere
USGS	United States Geological Survey
VIIRS	Visible/Infrared Imager/Radiometer Suite